ΠΑΝΕΠΙΣΤΗΜΙΟ ΙΩΑΝΝΙΝΩΝ
ΣΧΟΛΗ ΘΕΤΙΚΩΝ ΕΠΙΣΤΗΜΩΝ
ΤΜΗΜΑ ΧΗΜΕΙΑΣ

Ανάπτυξη σύνθετων υλικών με βάση το γραφένιο ως αντι-ηλεκτρόδια σε ευαισθητοποιημένα με χρωστική φωτοβολταϊκά κελιά

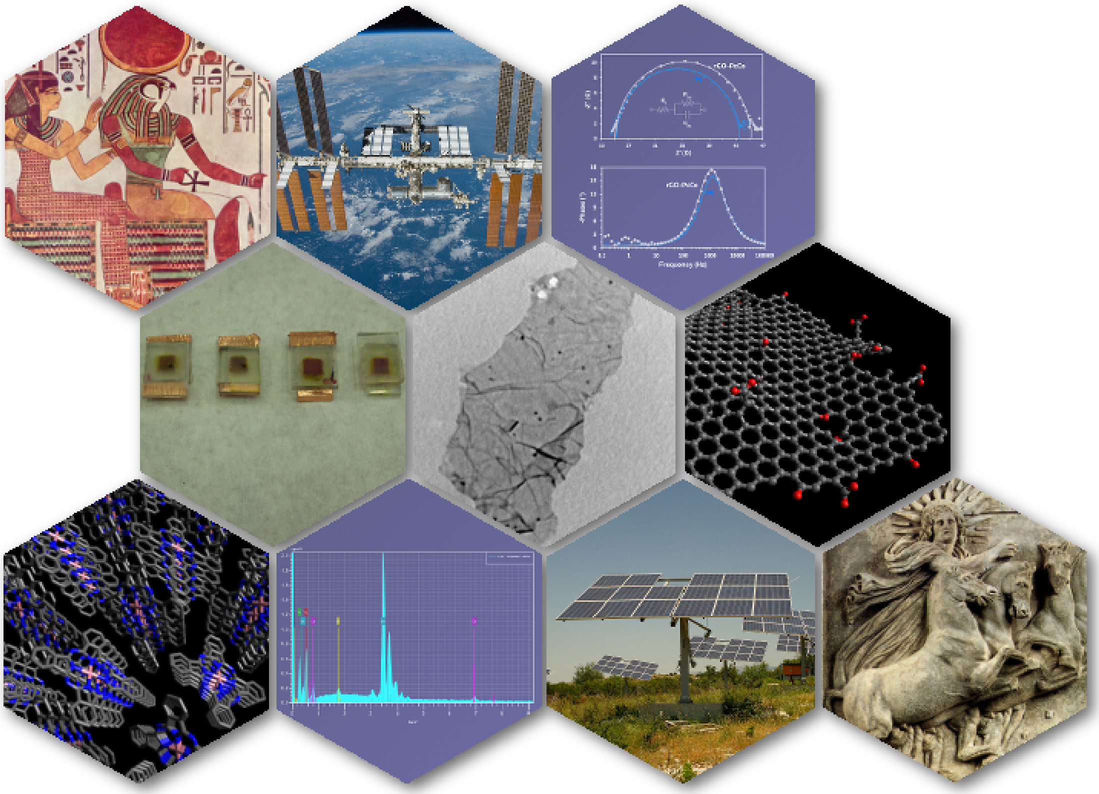

Αλέξανδρος Πλουμιστός

ΜΕΤΑΠΤΥΧΙΑΚΗ ΔΙΑΤΡΙΒΗ

ΙΩΑΝΝΙΝΑ 2017

ΠΑΝΕΠΙΣΤΗΜΙΟ ΙΩΑΝΝΙΝΩΝ
ΣΧΟΛΗ ΘΕΤΙΚΩΝ ΕΠΙΣΤΗΜΩΝ
ΤΜΗΜΑ ΧΗΜΕΙΑΣ

Ανάπτυξη σύνθετων υλικών με βάση το γραφένιο ως αντι-ηλεκτρόδια σε ευαισθητοποιημένα με χρωστική φωτοβολταϊκά κελιά

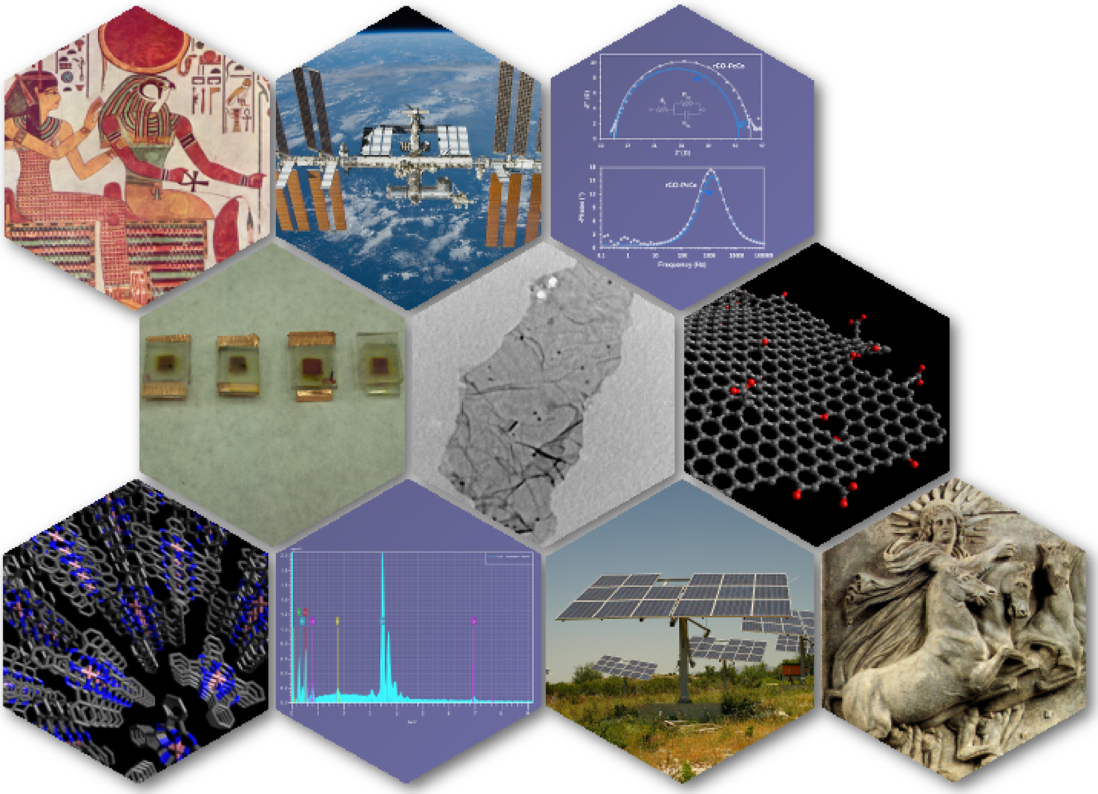

Αλέξανδρος Πλουμιστός

ΜΕΤΑΠΤΥΧΙΑΚΗ ΔΙΑΤΡΙΒΗ

ΙΩΑΝΝΙΝΑ 2017

Εισαγωγή στο Π.Μ.Σ. του κ. Αλέξανδρου Πλουμιστού: **08-10-2015**

Επιβλέπον μέλος ΔΕΠ:

Τάσης Δημήτριος

Θέμα: **«Ανάπτυξη σύνθετων υλικών με βάση το γραφένιο ως αντι-ηλεκτρόδια σε ευαισθητοποιημένα με χρωστική φωτοβολταϊκά κελιά»**

ΟΡΙΣΜΟΣ ΤΡΙΜΕΛΟΥΣ ΕΞΕΤΑΣΤΙΚΗΣ ΕΠΙΤΡΟΠΗΣ ΑΠΟ ΤΗΝ Γ.Σ.Ε.Σ.: ……^{Α}/…-…-…

1. ______________________________________
2. ______________________________________
3. ______________________________________

Έγκριση Μεταπτυχιακής Διατριβής στις …-…-…

Η Πρόεδρος του Τμήματος Χημείας
Λέκκα Μαρία – Ελένη, Καθηγήτρια

Η Γραμματέας του Τμήματος
Ζωή – Βαλεντίνα Βαμβέτσου

UNIVERSITY OF IOANNINA
SCHOOL OF SCIENCES
DEPARTMENT OF CHEMISTRY

Elaboration of graphene-based composite materials as counter electrodes in dye-sensitized solar cells

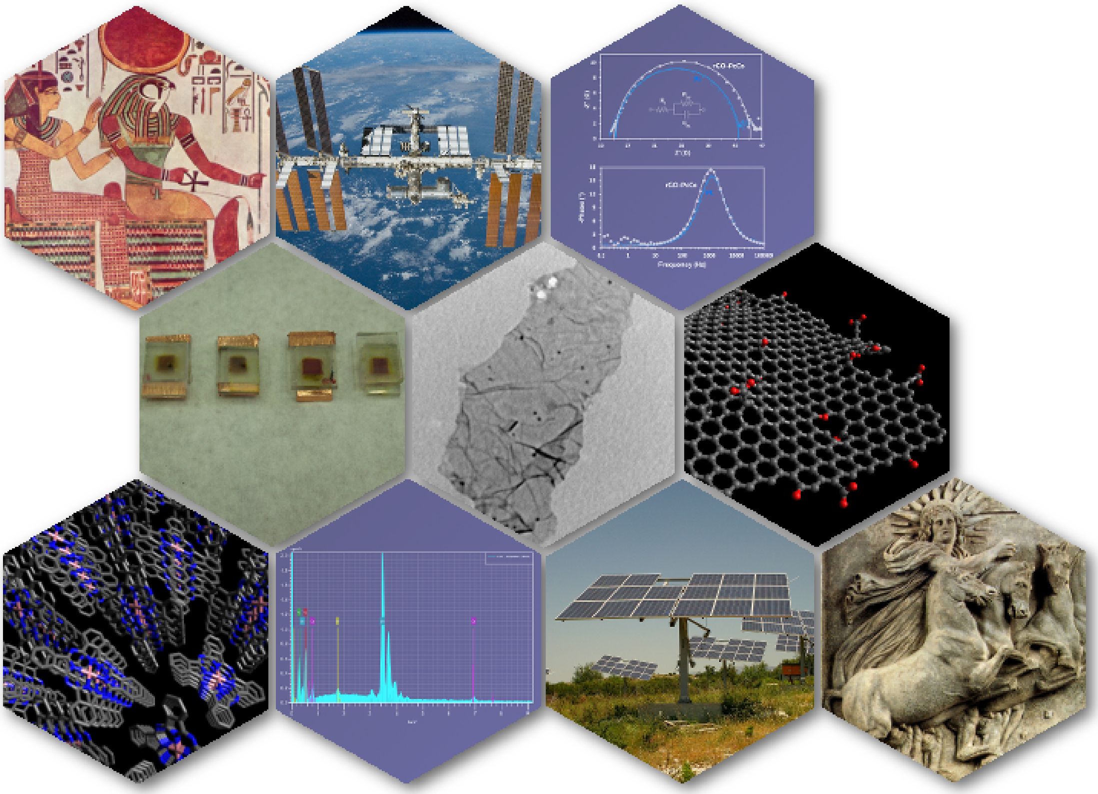

Alexander Ploumistos

MASTER THESIS

IOANNINA 2017

Dedicated to JD

Quot libros, quam breve tempus!

Περίληψη

Τα ευαισθητοποιημένα με χρωστική φωτοβολταϊκά κελιά (DSSC) αποτελούν μία από τις πολλά υποσχόμενες τεχνολογίες στον τομέα της ηλιακής ενέργειας. Πλεονεκτούν έναντι των υπαρχουσών τεχνολογιών όσον αφορά τις δομικές τους ιδιότητες και – κυρίως – έχουν την δυνατότητα να παράξουν ενέργεια αξιοποιώντας την διάχυτη ακτινοβολία (π.χ. όταν επικρατούν νεφώσεις) ή ακόμα και αυτήν από τεχνητό φωτισμό σε εσωτερικούς χώρους. Ένα από τα ζητήματα, που απομένουν να επιλυθούν, ώστε τα DSSC να περάσουν στο στάδιο της παραγωγής, είναι αυτό της αντικατάστασης του λευκόχρυσου (Pt) με κάποιο τουλάχιστον εξίσου αποδοτικό ηλεκτροκαταλυτικό υλικό στο αντι-ηλεκτρόδιο των διατάξεων. Το γραφένιο, που διαθέτει έναν απαράμιλλο συνδυασμό ιδιοτήτων, όπως οπτική διαφάνεια και υψηλότατες τιμές ηλεκτρικής αγωγιμότητας και μηχανικής αντοχής, θα μπορούσε ενδεχομένως – έπειτα από κατάλληλες τροποποιήσεις – να είναι αυτό το υλικό. Στην παρούσα εργασία παρασκευάστηκαν δύο τέτοια υλικά. Το πρώτο προέκυψε από ανόπτηση οξειδίου του γραφενίου με φθαλοκυανίνη του κοβαλτίου(ΙΙ). Το αποτέλεσμα αυτής της κατεργασίας ήταν ένα υβριδικό υλικό, εμπλουτισμένο με λειτουργικές μονάδες του τύπου CoN_3, ενταγμένες στο πλέγμα του ανηγμένου οξειδίου του γραφενίου, το οποίο ήταν παράλληλα «διακοσμημένο» με πλειάδες του ακέραιου συμπλόκου. Το δεύτερο, διστρωματικό σύνθετο υλικό, παρασκευάστηκε μέσω μίας μεθόδου συναρμολόγησης «στρώμα-στρώμα» (layer-by-layer assembly): επίστρωση μείγματος οξειδίου του γραφενίου και ουρίας σε αγώγιμο υπόστρωμα, ανόπτηση για τον σχηματισμό ανηγμένου οξειδίου, εμπλουτισμένου με άζωτο και έπειτα ηλεκτροεναπόθεση ενός υμενίου του διάφανου συζυγιακού πολυμερούς PEDOT. Τα υλικά αυτά χρησιμοποιήθηκαν για την κατασκευή φωτοβολταϊκών διατάξεων και αμφότερα έδωσαν συγκρίσιμα ή και καλύτερα αποτελέσματα σε σχέση με τον λευκόχρυσο, ως προς την απόδοση στην μετατροπή ενέργειας.

Abstract

Dye-sensitized solar cells (DSSC) are one of the most promising, emerging solar technologies. Their advantages over existing technologies include their structural properties and – mainly – their ability to produce energy under diffuse sunlight (e.g. on cloudy days) or even artificial indoor lighting. One of the issues that remain to be addressed, so that DSSCs may enter the production stage, is the substitution of platinum (Pt) in the counter-electrodes of the devices, with an at least equally performing electrocatalytic material. Graphene, which possesses an unparalleled combination of properties, such as optical transparency, very high electrical conductivity and mechanical strength, could – after suitable modifications – be that material. Two such materials are presented in this thesis. The first was produced by annealing graphene oxide with cobalt(II) phthalocyanine. The result was a hybrid material, doped with CoN_3-type moieties in the reduced graphene oxide lattice, which was also “decorated” with clusters of intact complex. The second, bilayer composite material was produced following a layer-by-layer assembly process: applying a coat of graphene oxide and urea mixture onto a conducting substrate, annealing it so that N-doped reduced graphene oxide was formed, followed by the electrodeposition of a film of PEDOT, a conjugated, transparent polymer. These materials were used to construct solar cells and both of them yielded comparable or better results than platinum, in terms of energy conversion efficiency.

Table of Contents

Preface

This is an attempt to document and sum up the last couple of years of my academic life. It will probably end up gathering dust on a library shelf, as is the case with most postgraduate dissertations these days, but I would like to think that some day, someone might find something useful in it. It is hard to put on paper two years' worth of joys, frustrations, discoveries and learning and in the end, not many people will care for that, especially in a document that serves such a specific purpose. Nevertheless, all those experiences and feelings are here: hiding underneath a chart or lurking behind an offhand remark. I will digress no longer, I just want to assure any prospective reader that I will do my best to keep my account as concise and you as interested in it, as this format allows.

Acknowledgments

It is customary to include the acknowledgments in the preface; I won't break with tradition here. A lot of people have contributed to the realization of this work – whether they know it or not – and credit has to be given where it is due. Even though my first year in the Master's program was filled with lectures and conferences, I found that the most educational and eye-opening conversations took place in hallways, over a cup of coffee or lunch, rather than in lecture halls.

The main body of this work was carried out at the Department of Chemistry, University of Ioannina. Annealing of the samples was performed at the tube furnaces of either the laboratory of the Layered & Nanoporous Materials Group, Department of Materials Science & Engineering, University of Ioannina or the laboratory of Prof. Emeritus Panagiotis Lianos, Department of Chemical Engineering, University of Patras. Fabrication of PV cells, performance and EIS measurements took place at the latter as well. XRD measurements were taken at the Department of Physics, University of Ioannina and Raman measurements at the Institute of Chemical Engineering Sciences (ICE-HT) in Patras.

First and foremost I want to thank my supervisor, Assistant Professor Dimitrios Tasis for a multitude of reasons: He gave me the opportunity to work with such fascinating materials on such a truly interesting project. His support on so many levels and his discrete guidance went above and beyond what is generally expected from an academic supervisor, they were almost parental. I was given absolute freedom to organize our laboratory and to pursue any avenues I found interesting, while my input was always taken into account. Even during the times that I left the lab in the wee hours and despite any physical exhaustion, I would have enjoyed myself so much, to the point of feeling guilt.

Over the years, I've had many friends in the LNM group and I always admired their work. Professor Dimitrios Gournis, who leads the group, carries the rare trait of being both a great teacher and a brilliant researcher. On many instances he has been quick to offer his help and our interactions, however brief, always gave me food for thought. For that I owe him my deep thanks, as I do to Dr. Myrsini Antoniou, another gifted (now former) member of the group. Even though some of my samples caused her quite a bit of trouble, not only does she still speak to me, but she keeps giving me advice from far far away.

Professor Achilleas Garoufis has been my teacher and at times my therapist and a lifesaver. His counsel has been invaluable and our discussions on whatever subject are always a pleasure. Words may fail me, but he knows that he has my respect, my gratitude and my friendship.

Though we spent a considerable amount of time together with Professor Mamantos Prodromidis, discussing measurement techniques and designing experiments, our plans did not move forward, as I had to abandon a particular fabrication method. Nevertheless, I did pick up quite a number of things pertinent to my work along the way and for them, as well as for his agreeing to be on my committee, I am thankful.

I would like to thank Professor Emeritus Panagiotis Lianos from the Department of Chemical Engineering at the University of Patras, with whom we have collaborated on this project and at whose lab I received training on the fabrication of DSSCs and measuring their performance. Working alongside his team was both a pleasure and a privilege. PhD candidate, Dimitrios Raptis, part of that team, has conducted all the PV efficiency measurements presented here, often putting his own work on hold. I am really grateful for everything.

I never thought that looking at a graph could make me happy, until the day that I received one particular X-ray diffractogram from Dr. Christina Papachristodoulou. Just for this work, she has taken close to one hundred PXRD measurements; many more if we take into account the secondary projects I have dabbled with. She has my many thanks.

I need to thank Dr. Lamprini Sygellou, who has performed the XPS analyses of my most interesting samples. During my visit to ICE-HT, she did her best to make me feel at home and she gave me such a detailed walk-through of the equipment and the various procedures involved, that if I didn't know any better, I'd say she was training her replacement.

I was always fascinated by microscopy and even more so by the techniques that allow us to visualize molecules and atoms. Dr. Mary Kollia at the Department of Biology, University of Patras, allowed me to image some of my samples, using a transmission electron microscope after a mini crash course on the instrument's principle of operation and the particulars of the machinery. She has provided all the TEM micrographs you will see later on. I wish to thank her as well.

I would be remiss not to mention my friends and neighbors in the X3 building, who made the longer days seem shorter and who, during our countless discussions, helped expand my understanding of Chemistry: Panagiotis Karagkounis, once my lab partner, who defected to teaching – I don't hold it against him (any more); Dr. Afroditi Tabaki, my next-door neighbor, whose smile alone is worthy of mention and who has helped me more times than I could count during my time here; Dr. Konstantinos Ypsilantis, who shares my passion for tinkering, assisted me in assembling quite a few odd contraptions – which surprisingly worked – and he always let me play with his toys; Theodoros Tsolis, always on the brink of a burn out, yet ever-cheerful; Michalis Papanikolaou, destined for greatness and also my go-to guy for exotic reactants and glassware; Sophia Rapti, distressed but happy with her MOFs; Evgenia Fotou, who whines a lot, but means well and is really good with peptides; Andreas Mazis, my willing linux student, who will hopefully get to play with snakes and not just their venom by the time he gets his degree; Androniki Kostagianni, despite working in the bleakest laboratory of the building, always managed to lift my spirits when we crossed paths; Alexia Tsapinou, the person most likely to be in her lab after hours, during weekends and holidays – may she be rewarded for her efforts eventually.

A debt of gratitude is owed to my extended family; not just the people with whom I share a blood bond, but also some great teachers I've had through the years and a few select people who opened their hearts to me. They all know who they are and I am forever grateful to them.

Last, but certainly not least, I want to thank my significant other, Fay Gkaniatsou for all her love, support and tolerance. Without her spurring me, I would still be looking for my way.

On copyright and the tools used in this work

Unless otherwise noted, all images, illustrations, etc. presented herein are either own work, or in the public domain.

This work was produced in its entirety using Free/Open Source Software:

Prior to this undertaking, I happened to work for a local business that installed photovoltaic systems. During my four years with them, as part of my job I had to read a lot of scientific articles, product literature and pretty much anything related to solar technologies. This “encyclopedic” knowledge stuck with me and most of what I have written about photovoltaics and other solar power-related trivia in the following introduction is based on it, hence the limited number of references in there.

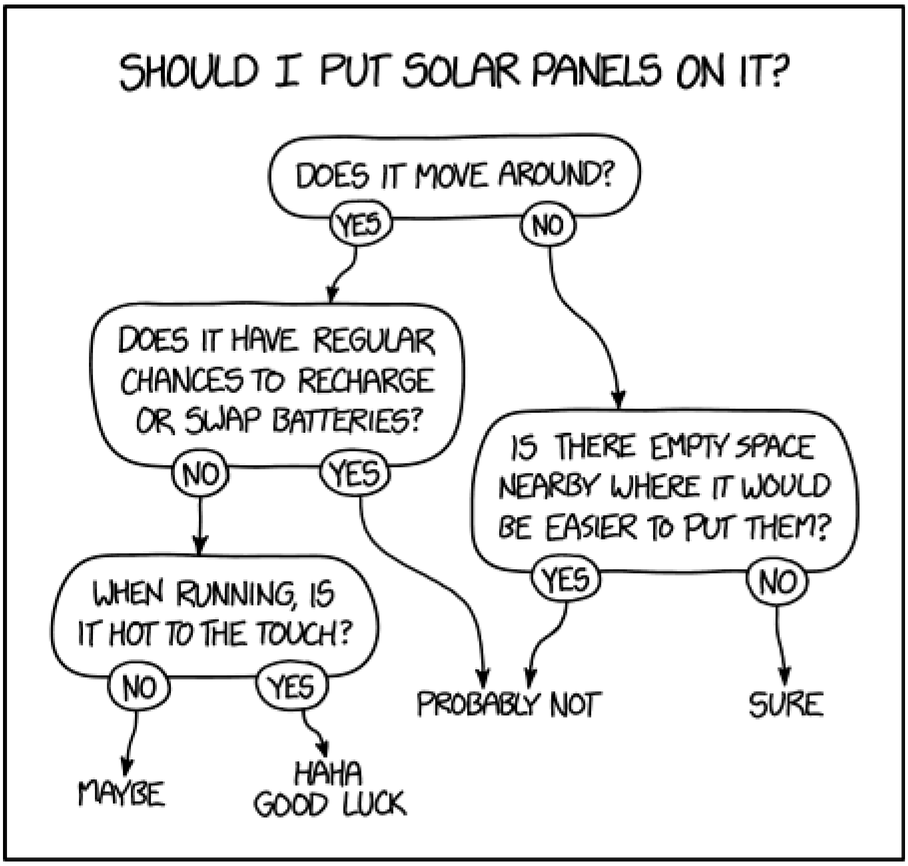

"This works for a surprising range of sunlit things, including rooftops (sure), highway surfaces (probably not), sailboats (maybe), and jets, cars, and wild deer (haha good luck)." - xkcd.com

Parts of this thesis have been published in the following articles:

1. Belekoukia, M.; Ploumistos, A.; Sygellou, L.; Nouri, E.; Tasis, D.; Lianos, P. Co–N Doped Reduced Graphene Oxide Used as Efficient Electrocatalyst for Dye-Sensitized Solar Cells. *Solar Energy Materials and Solar Cells* **2016**, *157*, 591–598 DOI: 10.1016/j.solmat.2016.07.042.
2. Paterakis, G.; Raptis, D.; Ploumistos, A.; Belekoukia, M.; Sygellou, L.; Ramasamy, M. S.; Lianos, P.; Tasis, D. N-Doped Graphene/PEDOT Composite Films as Counter Electrodes in DSSCs: Unveiling the Mechanism of Electrocatalytic Activity Enhancement. *Applied Surface Science* **2017**, *423*, 443–450 DOI: 10.1016/j.apsusc.2017.06.180.

Parts of this thesis have also been presented at the following conferences:

1. **22nd Panhellenic Chemistry Conference "Chemistry: Research and Education aiming at sustainable development"**, Thessaloniki, Greece (02 - 04/12/2016)
   "Co-N doped reduced graphene oxide used as counter electrode in Dye-sensitized solar cell device" A. Ploumistos, M. Antoniou, L. Syggellou, P. Lianos, D. Tasis (poster)
1. **5th Conference of the Department of Chemistry, University of Ioannina,** Ioannina, Greece (29 - 30/09/2017)
   "Synthesis of multifunctional 2D nanostructures and applications" A. Ploumistos, I. Tzanidis, P. Karagkounis, D. Tasis (poster)

List of abbreviations used in this work

AFM Atomic Force Microscopy
AM Air Mass coefficient

BIPV Building-Integrated Photovoltaics

CE Counter-Electrode
CI(G)S Copper Indium Gallium (di)Selenide
CSP Concentrated Solar Power
CV Cyclic Voltammetry
CVD Chemical Vapor Deposition

DSC Differential Scanning Calorimetry
DSSC Dye-Sensitized Solar Cell
DTA Differential Thermal Analysis

EDOT 3,4-ethylenedioxythiophene
EDS Energy-dispersive X-ray spectroscopy
EIS Electrochemical Impedance Spectroscopy

FESEM Field-Emission Scanning Electron Microscopy
FTO Fluorine-doped Tin Oxide

GO Graphene Oxide

HCPVT High Concentration Photovoltaic Thermal
HOMO Highest Occupied Molecular Orbital
HVAC Heating, Ventilation and Air Conditioning

ITO Indium Tin Oxide

LED Light-Emitting Diode
LUMO Lowest Unoccupied Molecular Orbital

MIDA N-methyliminodiacetic acid
MOF Metal-Organic Framework

OD Oxidative Debris

PcCo Cobalt(II) Phthalocyanine
PcFe Iron(II) Phthalocyanine
PcMg Magnesium Phthalocyanine
PEDOT Poly(3,4-ethylenedioxythiophene)
PEDOT-TMA Poly(3,4-ethylenedioxythiophene)-Tetramethacrylate
PSS Polystyrene Sulfonate
PTFE Polytetrafluoroethylene
PV Photovoltaics
PXRD Powder X-Ray Diffraction

rGO reduced Graphene Oxide

SEM Scanning Electron Microscopy

TCO Transparent Conducting Oxide
TEM Transmission Electron Microscopy
TFT Thin-Film Transistor
TGA Thermogravimetric Analysis
THF Tetrahydrofuran

XPS X-ray Photoelectron Spectroscopy

Encumbered forever by desire and ambition
There's a hunger still unsatisfied
Our weary eyes still stray to the horizon
Though down this road we've been so many times

1. Introduction

Problems...

In the last few decades, humankind has been slowly awaking from its deep and blissful slumber and coming to grips with some hard realizations: Fossil fuel reserves are nearing depletion. Burning them affects the planet's climate (not in a good way) and at the same time bereaves us of the primary source for the large scale production of medicines and plastics. Most of our activities waste a lot of energy. Nuclear energy might have its uses, but powering our cities and infrastructure, is most definitely not one of them; nuclear waste is far too dangerous and costly to handle and it has to be stored, it won't magically go away. It has been several millennia since our ancestors postulated that “ex nihilo nihil fit”, which morphed into the laws of conservation of energy and mass. One would expect that these and their corollaries would be deeply seated in our collective mindset, yet we as a species have been going about our business seemingly unaware of them for far too long.

One of the principal human traits appears to be the unwillingness to plan ahead and change our ways, until there is a cost involved, usually paid in lives as well as money. Now that we have made several down payments, we are slowly starting to grasp the responsibilities that our stewardship of this planet entails and what we should be doing to carry them out. So far, our existence on Earth has been parasitic; it needs to become symbiotic. We cannot exist outside what we have abstractly termed “the environment”.

Among the top priorities of most developed and developing countries is (or should be) the diversification of energy production for our ever-increasing needs as well as decreasing our reliance on finite energy sources – a reliance which has also been the cause of numerous conflicts and wars. Since global population growth is limiting the areas that we can use as dumping grounds and pollute in an “out-of-sight-out-of-mind” manner, energy production needs to be “clean”, i.e. without us having to deal with the storage of harmful waste or toxic emissions and with zero impact on the planet's climate. Even though a significant number of backward-thinking, “business as usual” reality deniers in positions of power is hampering ongoing efforts to avert ours and our planet's demise, a global consensus is slowly forming on how to tackle these global problems. At glacial speeds, yet it is forming.

A (really) brief overview of solar technologies

Looking to the skies for answers

Fortunately for us, we happen to live just three hops away from the biggest nuclear reactor in the solar system. This enormous fusion reactor's spent fuel turns primarily to harmless helium, which we don't have to bury deep underground and we don't even have to bother with the reactor's maintenance – not for at least another 5 billion years. Speaking of our Sun, it is the single most important energy source for life on Earth, as every living being ultimately depends directly or indirectly on photosynthetic organisms for its sustenance. The Sun's energy output peaks at ~1000W/m^2 on our planet's surface or ~1400W/m^2 just outside the Earth's atmosphere[1] and it is the driving force behind almost every phenomenon from the formation of wind and rain, to sea waves and the dissemination of plant seeds. Harvesting just a fraction of that energy in its many forms, coupled with energy-efficient processes could cover humanity's needs in perpetuity (or at least for many many thousand years) and give us the necessary breathing room to tackle our many other problems.

There are a number of ways we can profit from the Sun's energetic bombardment. Some methods have been around since humans first started building their homes, while others are fairly new. The ancient Egyptians, who worshiped the Sun god Ra (Image 1.1), are often credited as the first to purposefully build "green" residencies; their houses stored up the Sun's heat during the day and released it at night, maintaining a near-constant indoor temperature. Today we are in a position to combine our detailed logs and models of an area's microclimate and yearly solar exposure with materials with specific reflectivities, heat capacities and porosities, to design buildings with zero or minimal energy needs for heating, ventilation and cooling. Solar water heaters and cookers have been with us for quite some time, but their efficiency varies depending on the geographic latitude. Of particular interest is the process of artificial photosynthesis, i.e. the use of light to initiate and sustain chemical reactions. Though first proposed on a theoretical level in the early twentieth century and while the first commercially viable photocatalysts appeared in the late 1960s, it was in the last couple of decades that research on this topic really took off. The end goal is the production of useful substances (e.g. hydrogen, synthetic fuels, precursors for industrial use, etc.) in both small and large scale, with no energy input, other than sunlight. Perhaps most important of all these applications is the conversion of light into electricity.

Image 1.1: Imentet and Ra. Mural from the tomb of Nefertari, 13th century BCE.

Currently, there are two mainstream technologies for converting solar energy to electricity: concentrated solar power plants (CSP) and photovoltaic systems (PV). There are also a number of emerging hybrid technologies, but they are either in an experimental or proof-of concept stage. Concentrated solar power plants make use of mirrors, lenses and tracking systems, to focus sunlight into small areas. The impressive amount of heat concentrated on the focal point of those beams, heats up and sets in motion a working fluid medium, which can be used for energy storage or to provide in turn heat to a steam turbine, which generates electricity. Photovoltaic systems rely on the photovoltaic effect (closely related to the photoelectric effect) where light incident upon a material causes the excitation of electrons to higher energy states. At times, this can set them free from their parent atom and this separation of charges leads to the appearance of an electric potential difference (voltage) at the edges of the device (Figure 1.1). There are several types of solar cells, but the most prevalent one is the large area photodiode, constructed from single or multiple silicon-based p-n junctions.

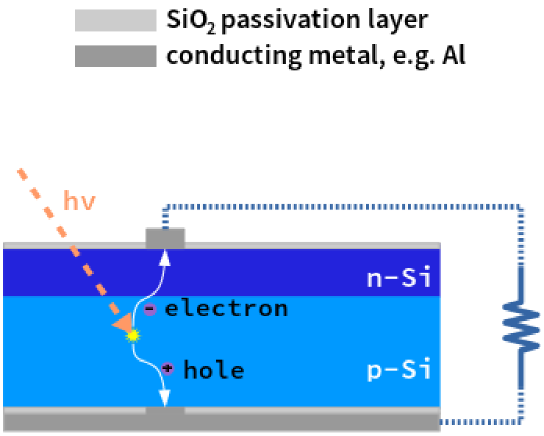

Figure 1.1: Schematic and principle of operation of a Si solar cell.

CSP and PV combined, accounted for 1.05% of total global electricity generation in 2016, with PV systems providing the majority of that. Global solar PV capacity has grown from less than 4GW at the turn of the century to 303GW in 2016. This brings photovoltaics to the third place among renewable energy sources, behind hydro and wind power. Improvements in manufacturing have steadily increased the efficiency of solar panels, while driving unit costs down. Just in 2016, more than 75GW of solar PV capacity was added worldwide, which translates to more than 31000 solar panels being installed every hour. Even though state subsidies in the form of feed-in tariffs, tax deductions and exemptions have been declining in the developed world, PV installations are continuing to grow exponentially every year. This has to do with their modular nature, their constantly improving efficiency/cost ratio and their increased use in tandem with energy storage systems.[2–4]

Image 1.2: A small (100kW) PV park on the outskirts of Ioannina, with modules mounted on solar trackers.

It is worth expanding on that last one a bit. Obviously, solar systems can not produce energy at night and their yield drops on cloudy days. Thus it was thought impossible to add solar input in power grids beyond a certain ratio and keeping “traditional” power plants in place to compensate for that lack of constant power output was deemed a necessity. There where also fears of grid stability issues due to the need to drive power production up or down, depending on the state of renewables. Serendipitously, as PV installations started to boom, a number of energy storage technologies reached maturity. Small and large scale batteries are being deployed everywhere from homes to autonomous storage plants, while a number of less known or even “exotic” solutions, such as redox flow batteries, flywheels, pumped, compressed air and thermal energy storage, among others, are being put in operation. This has dispelled most fears and it has led governments and authorities around the world to reconsider their estimates and energy development strategies.[5–12]

Silicon is king

Since 1839, when Alexandre-Edmond Becquerel first observed the photovoltaic effect[13], using an acidic solution of AgCl and Pt electrodes, a wide range of materials have been tested and employed in the conversion of sunlight to electricity, while many more are under investigation. Metals, metalloids, metal oxides, chalcogenides and almost every other processable element have been used or combined to form p-n junctions, the workhorse in most types of solar cells. Yet, no other material or combination of materials has managed to outperform silicon simultaneously in efficiency, stability, ease of manufacturing and cost.

Advances in semiconductor technologies in the late 1940s ushered in the dawn of the Digital Revolution – sometimes referred to as the Third Industrial Age. While the first semiconductor-based electronic components to be mass-produced were created using elements like germanium, gallium and selenium, within the next decade or so, the bulk of production had shifted over to silicon. This made perfect sense, as silicon happens to be the second most abundant element in the Earth's crust (a little over 27% by mass) and its physicochemical properties were just right for the intended uses, while at the same time they allowed for it to be easily processed and purified. As most aspects of our everyday lives grew all the more dependent on integrated circuits, we learned to make bigger, purer silicon crystals (Image 1.3); we learned to finely control the introduction of impurities into these crystals, almost down to the atomic level; and we also learned how to etch patterns on their surface, with near-nanometer precision. It is hard to think of another industry that has seen such a constant stream of innovations in all its areas of activity and at such a pace, as the silicon industry.

Image 1.3: Monocrystalline silicon boule. Photograph by wikimedia.org user Saperaud~commonswiki, CC-BY-SA 3.0.

Silicon solar cells first became commercially available in the mid-1950s and for a while they were considered for space applications, though that industry settled for the much more expensive, but also more efficient GaAs variant (its cost, along with a few technical disadvantages have precluded its use in terrestrial applications). Research -as well as consumer- interest in Si solar cells at the time was rather limited. It wasn't until the energy crises of the 1970s that governments and private corporations decided it was high time they invested heavily in solar energy research. Luckily, the field wasn't exactly “terra nova” and as soon as the infrastructure was put in place or modernized, the industry started building upon the lessons learned from electronics. As an example, the need for bigger computer and TV flat screens led to the production of bigger, lighter and perfectly uniform and transparent glass and polymer panes. These same panes are now used as substrates and covers in solar modules. Similarly, the search for high-performance, brighter red, blue and green elements in thin-film transistor (TFT) displays has benefited the PV industry twice: it yielded the cheaper polycrystalline Si cells (Image 1.4) on one hand and multi-layered solar panels, with each layer absorbing specific wavelengths of the visible spectrum for increased overall efficiency on the other.


Image 1.4: Detail of a polycrystalline solar module. The variations in color are due to the differently oriented crystallites within the bulk material.

Monocrystalline silicon solar cells once dominated the market, but over the last couple of decades, polycrystalline silicon panels, which are easier to produce and thus cheaper, have climbed to the first place, even though they are slightly less efficient. Solar cells fabricated using these two materials, are often classified as “first generation” cells. In 2016, mono- and poly-Si amounted for a little over 94% of the global PV production.

Contenders to the throne

The second generation of solar cells reached commercial availability in the early 2000s. They are also called thin film solar cells, because the thickness of the active, light-absorbing material – a few nm to tens of μm depending on the technology and production method – is a fraction of that of silicon cells, which typically measure ~200nm. The “thin film” blanket term covers three mainstream technologies: amorphous silicon (a-Si), cadmium telluride (CdTe) and copper indium gallium (di)selenide ($CuIn_xGa_{(1-x)}Se_2$, commonly called CIGS or CIS, for $0<x<1$ and $x=1$ accordingly). Some of these materials have a higher optical band gap than silicon, so a thinner layer is required to absorb the same amount of sunlight. In addition, the active material can be deposited on a substrate using a variety of methods, even direct printing. This offers several key advantages over crystalline silicon: The solar cell can be shaped and does not need to be flat. It is also possible to deposit the film on flexible substrates, opening the door to a very wide and diverse set of possible applications, from wearables to building components. Equally and perhaps even more importantly, less material is used in the construction of the cells, which lowers their cost and their environmental footprint.

Thin film photovoltaics launched with much fanfare, promising to address several of the shortcomings of the first generation of solar cells and they were even poised to be the major source of PV-generated electricity by 2020, despite their noticeably smaller efficiency. On paper, their advantages seemed just right for the job: they can absorb diffuse and not just direct sunlight, most of the absorbed light turns to electricity, so less runaway heat and loss of efficiency due to increased resistivity and they are lighter, requiring smaller rigid supports. The deposition techniques used to produce them, also meant that it was possible to manufacture light-harvesting building elements such as roof shingles, tiles, panes and bricks, addressing the aesthetic horrors incurred by “traditional” roof-mounted PV installations.

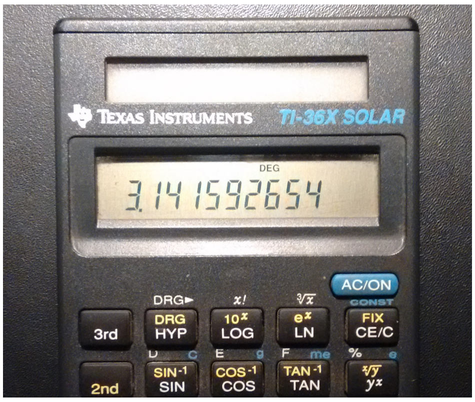

Image 1.5: a-Si has been used in low-power devices since the late 1970s.

As we are nearing 2020, thin film global production has settled around 6%, save for a brief period of silicon panel shortages around 2010, when it spiked to 17%. Despite their boasted advantages, thin film cells have failed to outperform silicon; sure, they might do somewhat better on a cloudy day, but their year-round production falls far short. Cd, In, Te and Ga are rather scarce, so mass production hasn't been able to decrease costs at the same rate as Si cells. Amorphous silicon panels are almost extinct, while many companies that invested in them went bankrupt. There is some research in combining a-Si with other materials or multi-Si, but that is a long way from a commercial product. CIGS cells continue to be developed, as are CdTe cells, which have fared a lot better than the other two competing thin film technologies. While there are some large solar parks using CdTe panels, it appears that CdTe and CIGS cells are best suited for building-integrated photovoltaics (BIPV) and other similar applications, where it is impossible or impractical to use silicon.

The third generation of photovoltaics encompasses a broad spectrum of technologies, materials and combinations thereof, most of which are still in the research or development stage. The vast majority of them aim to provide more efficient light harvesting at a lower cost than current solar cells, but there are quite a few that hold interest for niche or exotic applications. To name a few, these applications include coupling low surface area-large scale power production (High Concentration Photovoltaic Thermal, or HCPVT)[14] with HVAC or other uses for zero-energy buildings and datacenters, “sunless” solar cells that produce energy in the dark[15] or achieving adequate output under extreme conditions for use in the colonization of other planets. Among the promising new materials being investigated are perovskites, quantum dots, organic and organometallic films. Optimizing existing materials e.g. by patterning, or using them in new ways, in tandem with novel materials and nanostructures is another research field, which has yielded some interesting preliminary results.

Manipulating solar radiation by various means is also an exciting topic which is being extensively researched. Concentrating lenses, optical traps, waveguides, metamaterials and adaptive materials, that can alter their transparency or reflectivity could all be used to funnel more usable light into devices, minimizing losses and increasing performance. The energy carried by the Sun's rays is not evenly distributed; approximately 50% is in the infrared region (most of it in the near-IR part of the spectrum), 40% in the visible region and the remaining 10% in the ultraviolet region, while 70% of the latter is filtered by the Earth's atmosphere[1]. So far, we've been trying to tailor PV materials and their band gaps to match the energy pattern of sunlight; converting the more energetic UV or visible photons to IR photons and focusing them on materials that operate optimally at higher wavelengths would be another way to boost efficiency.

Most of these emerging solar technologies are really far from finished products – some of them decades away. Striking a balance between performance, long-term stability, low cost and ease of manufacturing isn't easy. “Traditional” silicon solar panels will be with us for many more years, as they perform well, they are cost-efficient, they are constantly improved and their reliability has been tested for more than half a century, to the point that many manufacturers back their panels with 20 or 30-year warranties. However, newer devices do not have to beat silicon in every aspect to be deemed successful or at least useful. A cell that degrades within a month, but which has a moderate efficiency and costs pennies to produce could still see a number of uses. Thermophotovoltaics could be installed on sites with excess heat such as factories and power plants and complement power production. HCPVT systems can be put in operation on islands or any place with little available land for traditional solar parks. Transparent cells can be integrated into glass windows. Flexible films, depending on their stability, can be applied on pretty much any surface from vehicle chassis to interior walls. This third generation of devices truly has the capacity to fundamentally alter how we conduct our lives on this planet and elsewhere. We could power entire cities without sacrificing precious farmlands. We could harvest every unused photon from indoor lighting or during cloudy days and feed it back to the grid – if we still need a grid. Stopping for gas, changing the batteries of our devices every few days will be habits of the past, much like we think today of our ancestors that had to get their drinking water from wells and streams. Truly autonomous robots, taking care of menial and labor-intensive tasks, disposable, self-powered and unobtrusive medical devices, colonists on Mars printing their own generators, these are all images of a future that will be within reach when this research bears fruit.

Dye-Sensitized Solar Cells

Featured prominently amid the third generation of solar devices are dye-sensitized solar cells, or DSSCs for short. While a number of researchers had been working on dye-based photogalvanic devices for years, the creation of the “modern” DSSCs is credited to Brian O'Regan and Michael Grätzel[16]. These cells rely on organic dyes or metals ligated with chromophores to capture light, much like photosynthetic organisms rely on chlorophyll to absorb energy from the Sun. Unlike semiconductor photovoltaics, where incoming photons produce electrons and holes in a single step process, in the case of DSSCs, irradiation of an organic dye results in the formation of an exciton[17], which then transfers its excited electron to a secondary material – usually a semiconductor such as TiO_2. The oxidized dye subsequently gets regenerated by extracting electrons from an electrolyte in contact with a counter-electrode, which completes the circuit.

The device proposed by O'Regan and Grätzel in their 1991 paper and its principle of operation is presented in Figure 1.2.

The anode of the device consists of TiO_2 nanoparticles which form a mesoporous layer, deposited on a glass substrate coated with fluorine-doped tin oxide (FTO), a conducting material. The dye (or sensitizer), which in the case of the O'Regan and Grätzel cell was a trinuclear ruthenium complex ($[Ru(bpy)_2(CN)_2]_2Ru(bpy(COO)_2)_2^{2-}$), is adsorbed as a monolayer on the TiO_2 nanoparticles, as shown in the inset of the preceding image. Energy from an incident photon is transferred to an electron which is excited from the highest occupied molecular orbital to the lowest unoccupied molecular orbital. While it is there, that energetic electron can then get injected into the conduction band of the semiconducting TiO_2 from where it will leave the device, performing useful work along the way. As current flows back into the cell via the counter-electrode, a triiodide ion is reduced to three iodide ions. In the last step of the process, an electron is extracted from an iodide by the dye cation, which returns to its neutral form and is ready to re-enter the cycle.

The maximum voltage measured between the terminals of the device (open-circuit voltage, V_{OC}) is roughly equal to the difference between the semiconductor's Fermi level and the redox potential of the electrolyte at ideal illumination conditions. As can be extrapolated from the schematic, in order for the cell to operate, the various energy levels of its components need to be matched in a specific order: the dye molecule's LUMO needs to be at least just over the semiconductor's Fermi level, so that electron injection can take place from the dye to the semiconductor; the dye's HOMO energy level has to be below the electrolyte's Nernst potential to favor electron extraction towards the cationic form of the dye; obviously, with such a setup, the Fermi level of the semiconductor can not be below the Nernst potential of the electrolyte system, otherwise no current would flow outside the cell. Another point to consider is the energy gap between the HOMO and the LUMO, which absolutely must be smaller than the energy carried by the photons in the part of the spectrum where the dye molecule absorbs light.

To further complicate things, besides the aforementioned thermodynamic parameters, the kinetics of all the charge carriers, donors and acceptors in the system need to be balanced strongly in favor of the reactions that govern the working principle described previously. That is the reason for example, that the I^-/I_3^- pair works well as a charge carrier; interconversion between the reduced and oxidized forms requires the participation of three and rather heavy atoms. In the timescale of the events that take

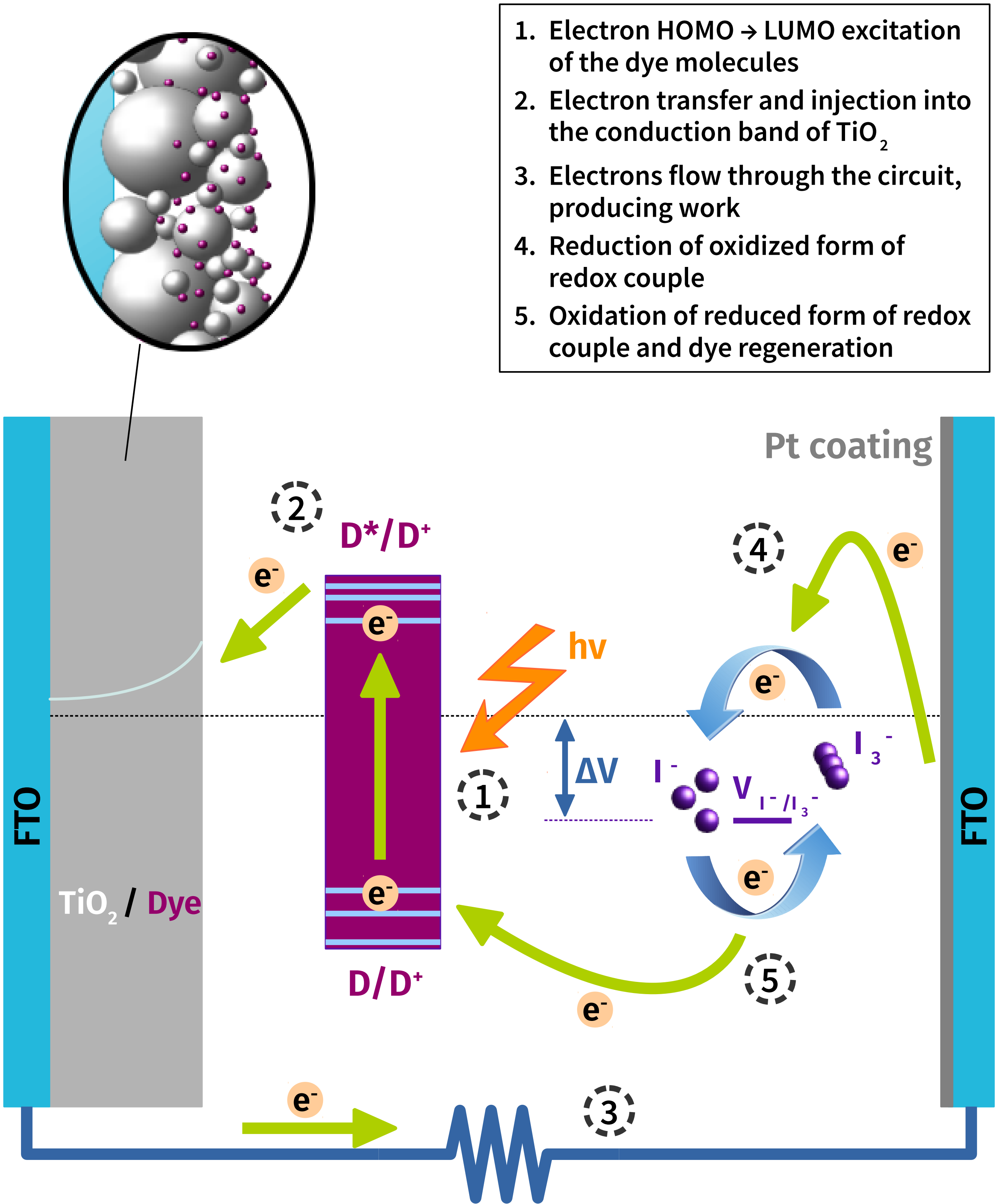

1. Electron HOMO → LUMO excitation of the dye molecules
2. Electron transfer and injection into the conduction band of TiO_2
3. Electrons flow through the circuit, producing work
4. Reduction of oxidized form of redox couple
5. Oxidation of reduced form of redox couple and dye regeneration

Figure 1.2: Schematic representation of a typical DSSC depicting the various steps in the process and the energy levels at each step. D, D* and D^+ is the dye in its base, excited and oxidized form, V is the Nernst potential of the I^-/I_3^- redox couple, the long dashed line represents the Fermi level of TiO_2 and ΔV is the measured voltage difference between the two electrodes. Inset: morphology of the photoanode.

place inside the cell, $3I^- \rightleftharpoons I_3^-$ interconversion is quite sluggish. Other unwanted reactions include D^+-e^- recombination, electron transfer from the semiconductor to the oxidized species of the electrolyte system and potential side-reactions between the principal components in their various forms, with secondary elements, such as solvents and insulators. Since charge separation and transfer happen at the interfaces between the semiconductor, dye and electrolyte, one needs to take into account the surface dynamics when designing a DSSC. A stronger bonding of the dye to the semiconductor surface could result in undesirable dipole-dipole interactions between the dye and the electrolyte, hindering its flow in the pores of the semiconductor; modulating the pH could improve electrolyte performance, but it could also shift the absorption maximum of the dye to lower wavelengths. All of the above interactions and side-reactions can hamper the efficiency of the devices and affect their long-term stability. In order to fabricate more efficient devices, it is therefore crucial to examine how each constituent fits in the overall assembly and anticipate how it might affect all the others[18].

At first glance, the counter-electrode seems rather unimportant, just completing the circuit, but in reality it is as important as any of the other components in the device. It might also seem superfluous to have two conductive layers stacked one on top of the other, but there is more going on there than meets the eye. The surface area of the Pt layer provides the sites where the oxidized form of the electrolyte comes into contact with the electrons flowing back into the cell, while its chemical inertness ensures that the charge-carrying ions don't end up trapped in a salt or react with the transparent conducting oxide, damaging it. Removing the Pt layer results in an increase of the charge transfer resistance at the electrolyte-cathode interface by six orders of magnitude. The mechanism for the reduction of triiodide is thought to consist of the following four steps[19]:

I. $I_3^- \rightleftharpoons I_2 + I^-$
II. $I_2 + 2Pt \rightleftharpoons 2I(Pt)$
III. $I(Pt) + e^- \rightleftharpoons I^-(Pt)$
IV. $I^-(Pt) \rightleftharpoons I^- + Pt$

The first step is the spontaneous dissociation of triiodide into an iodine molecule and an iodide ion. The iodine is then adsorbed onto two adjacent platinum atoms, where the I-I bond is relaxed and subsequently broken. Then follows the reduction of the iodine atom, which is the slowest step in the process. The resulting iodide is quickly desorbed from the Pt layer. It was also discovered that the cations in the solution greatly affect the speed of the whole process, which probably means that the ions listed above may not necessarily be in direct contact with Pt, but surrounded by a sphere of solvent molecules and counter-ions.

The 1988 O'Regan-Grätzel device was able to achieve conversion efficiencies of 7.9% and 7.12% under one tenth and full sunlight respectively (direct insolation), while the efficiency reached 12% under diffuse daylight. While these numbers may not seem like much, it's worth keeping in mind that commercially available crystalline panels at the time reached comparable efficiency levels and costed almost 40 times more than they do today. It should also be noted that unlike semiconductor solar cells, DSSCs perform better with diffuse than with direct sunlight. As for the longevity of the devices, the researchers noted in their paper: “The long-term stability of cell performance was tested by illuminating the thin TiO_2 film loaded with 1 (the dye) with visible ($\lambda > 400$ nm) light for 2 months. The change in the photocurrent was less than 10% over this period […]”.[16]

Obviously, a 10% degradation after just 2 months of operation would confine DSSCs to short and medium-term applications, provided that their cost is adequately low and they can be recycled or at least disposed of easily and in a safe manner, not unlike single-use batteries. Unfortunately, iodine is both toxic and corrosive, platinum is rare and very expensive and some sensitizers or their degradation products – while a minor component per mass – could also be hazardous. The matter of costs is further compounded by the use of ruthenium as the central atom in the dye complexes and the need for conducting glass. Having a liquid medium in the device imposes lower and upper temperature bounds for its operation: if the ambient temperature drops below its freezing point, power production will cease; if it is heated too much, it will expand, possibly rupturing the device.

Despite these shortcomings, DSSCs remain a promising technology, mainly because of the way the electrons are produced in contrast with p-n junctions (considerable output on cloudy days, indoors and under artificial lighting, minimized losses due to heat on warm, sunny days) and because organic molecules can be more easily modified to absorb light at specific wavelengths than semiconductors. The manufacturing process scales up well and does not require highly-specialized tooling and substituting TCO-covered glass with conducting polymers yields flexible devices, with a whole host of potential applications, so a lot of effort over the years has gone into addressing the aforementioned issues[20].

A lot of different optimizations have been proposed, which aim to alleviate the deficiencies of the original design: A redox pair with a Nernst potential below that of the I^-/I_3^- system increases its short-circuit current and subsequently its power output. Many researchers have switched to using cobalt complexes as charge mediators, which does increase the efficiency of the cells, but ultimately this approach trades one problem for another, as cobalt is also toxic and while not as scarce in the Earth's crust as Pt, it is not all that abundant either. Other strategies involve solid-state charge carriers, such as polymers or other materials, allowing for temperature-independent operation. Some efforts have concentrated on preventing degradation of the devices; to that end, there have been proposed better, oxygen-free sealing methods, the shielding of the sensitive components from UV radiation, modifying the dye molecules as to resist desorption by the solvent and several other avenues. Replacing the platinum in the cathode with a cheaper material would significantly lower the cost of the devices and make them more affordable, expanding their potential uses and user base. Of course, such a material would need to exhibit similar – if not better – kinetics and interactions with the redox pair as platinum, otherwise the cell's efficiency will take a hit and its “cutout” illumination limit will be raised, as unwanted recombinations would prevail sooner. Coming up with a counter-electrode with these properties has been the objective of this Master thesis.

Chapter Bibliography

[1] Fu, Q. Radiation (SOLAR) A2 - Holton, James R. In *Encyclopedia of Atmospheric Sciences*; Academic Press: Oxford, 2003; pp 1859–1863.

[2] *REN21 Renewables Global Status Report Highlights*; REN21 Secretariat: Paris; p 45.

[3] Philipps, S.; Warmuth, W. *Photovoltaics Report*; Fraunhofer Institute for Solar Energy Systems, ISE: Freiburg, 2017; p 44.

[4] BP Statistical Review of World Energy 2017. BP p.l.c 2017.

[5] Geuss, M. Power Company Kills Nuclear Plant, Plans $6 Billion in Solar, Battery Investment. *Ars Technica*. August 31, 2017.

[6] Geuss, M. German Energy Company Wants to Build Flow Batteries in Old Natural Gas Caverns. *Ars Technica*. July 22, 2017.

[7] Geuss, M. After Bet between Billionaires, South Australia Buys 129MWh Tesla Battery. *Ars Technica*. July 7, 2017.

[8] Timmer, J. Renewable Capacity Passes Coal, Additions Outpacing Demand in US, Europe. *Ars Technica*. October 26, 2016.

[9] Timmer, J. Renewables Won't Drive up Cost of Electricity from Fossil Fuel Plants. *Ars Technica*. April 5, 2017.

[10] Timmer, J. Renewable Energy's Global Growing Pains. *Ars Technica*. March 13, 2016.

[11] Timmer, J. Solar Is Top Source of New Capacity on the US Grid in 2016. *Ars Technica*. December 19, 2016.

[12] Geuss, M. Here Are Humanity's Best Ideas on How to Store Energy. *Ars Technica*. October 28, 2017.

[13] Becquerel, A. E. Mémoire Sur Les Effets Électriques Produits Sous l'influence Des Rayons Solaires. *Comptes Rendus Séances Hebd. Académie Sci.* **1839**, *9*, 561–567.

[14] Schmitz, M.; Wiik, N.; Ambrosetti, G.; Pedretti, A.; Paredes, S.; Ruch, P.; Michel, B.; Steinfeld, A. A 6-Focus High-Concentration Photovoltaic-Thermal Dish System. *Sol. Energy* **2017**, *155*, 445–463 DOI: 10.1016/j.solener.2017.05.087.

[15] Kruk, S. S.; Wong, Z. J.; Pshenay-Severin, E.; O'Brien, K.; Neshev, D. N.; Kivshar, Y. S.; Zhang, X. Magnetic Hyperbolic Optical Metamaterials. *Nat. Commun.* **2016**, *7*, 11329 DOI: 10.1038/ncomms11329.

[16] O'Regan, B.; Grätzel, M. A Low-Cost, High-Efficiency Solar Cell Based on Dye-Sensitized Colloidal TiO2 Films. *Nature* **1991**, *353* (6346), 737–740 DOI: 10.1038/353737a0.

[17] Petty, M. C.; Nagase, T.; Suzuki, H.; Naito, H. Molecular Electronics. In *Springer Handbook of Electronic and Photonic Materials*; Kasap, S., Capper, P., Eds.; Springer International Publishing: Cham, 2017; pp 1–1.

[18] Nazeeruddin, M. K.; Baranoff, E.; Gr?tzel, M. Dye-Sensitized Solar Cells: A Brief Overview. *Sol. Energy* **2011**, *85* (6), 1172–1178 DOI: 10.1016/j.solener.2011.01.018.

[19] Hauch, A.; Georg, A. Diffusion in the Electrolyte and Charge-Transfer Reaction at the Platinum Electrode in Dye-Sensitized Solar Cells. *Electrochimica Acta* **2001**, *46* (22), 3457–3466 DOI: 10.1016/S0013-4686(01)00540-0.

[20] Freitag, M.; Boschloo, G. The Renaissance of Dye-Sensitized Solar Cells. *Curr. Opin. Electrochem.* **2017** DOI: 10.1016/j.coelec.2017.03.011.

2. Graphene-based counter-electrodes

It did not take long after its discovery for graphene to be identified as a potential candidate for the replacement of platinum in DSSCs. In fact, its chemical, electronic, optical and mechanical properties have led some to envisage nanometer-thick dye-sensitized solar cells, in which almost every single component from the glass substrate to the charge carrier has been supplanted by graphene or graphene-based, nanostructured materials. Our own goals were more modest and we would be satisfied with a platinum-free counter electrode. Before we get into the experimental details, it is worth taking a look into the materials we opted to use, as well as the previous work done by others and on which we built.

Graphene

Often called a “miracle material” and hailed as the future of nanotechnology, graphene has rightly captured the imagination as well the interest of thousand of researchers around the world. There has been a torrent of publications regarding graphene following its isolation by Andre Geim and Konstantin Novoselov in 2004[1] and even more so after they received the 2010 Nobel Prize in Physics for that work (Figure 2.1). Its fame and potential future applications have breached the confines of academia and it is often featured in mainstream publications. The material itself is so versatile, that almost once a month there is a fundamental discovery concerning graphene and every other week, a new, innovative use is proposed for it.

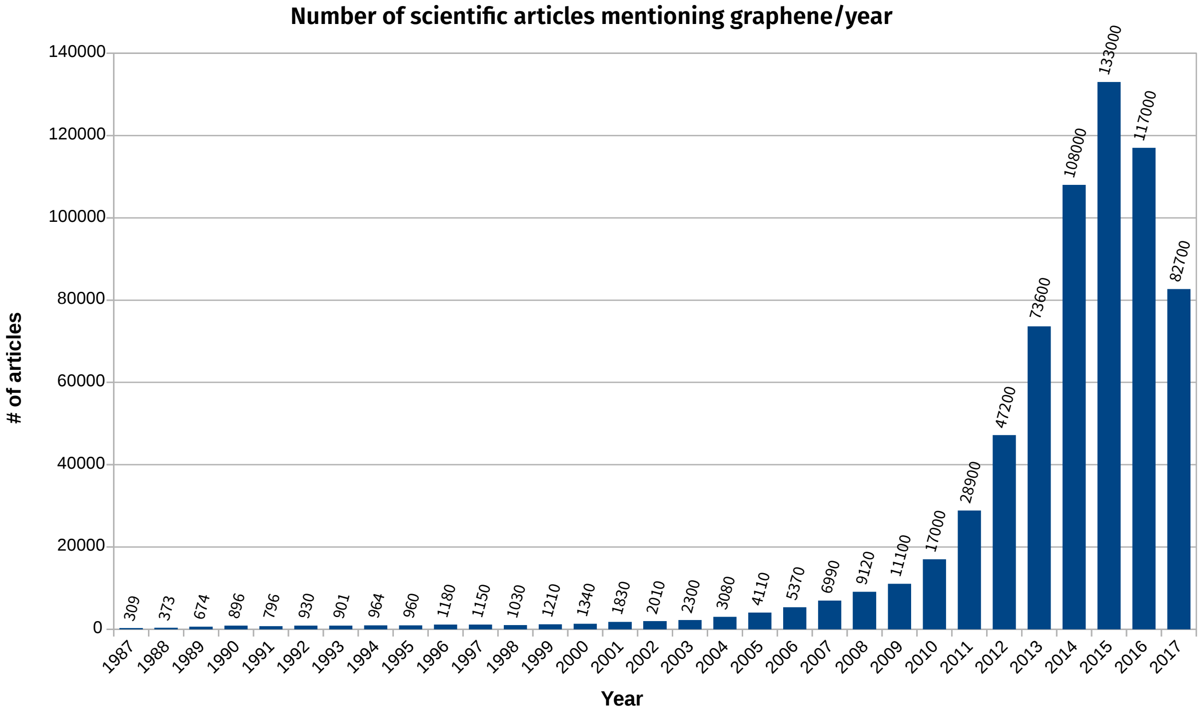

Figure 2.1: Number of published scientific articles referencing graphene per year, during the last couple of decades. (Data obtained from Google Scholar on 1 Nov 2017 - data for 2017 are up to the same date)

Properties

Graphene is the building block of humble graphite. It consists of a layer of sp^2-hybridized carbon atoms, arranged in a hexagonal honeycomb pattern, like myriads upon myriads of benzene molecules fused together. Its crystal lattice has a primitive cell containing two atoms. Much like in benzene, the bond length between two carbon atoms is 1.42Å – shorter than a single bond, but longer than a double bond[2]. Graphene sheets stack to form graphite and they are held together via van der Waals forces, which allow the sheets to slide against one another when an external force is applied. This is what makes graphite slippery to the touch and this property has been employed in high performance lubricants for decades. The distance between two sheets is about 0.335nm[3] (Image 2.1). In graphite, the sheets can adopt two different arrangements, as seen in Figure 2.2:

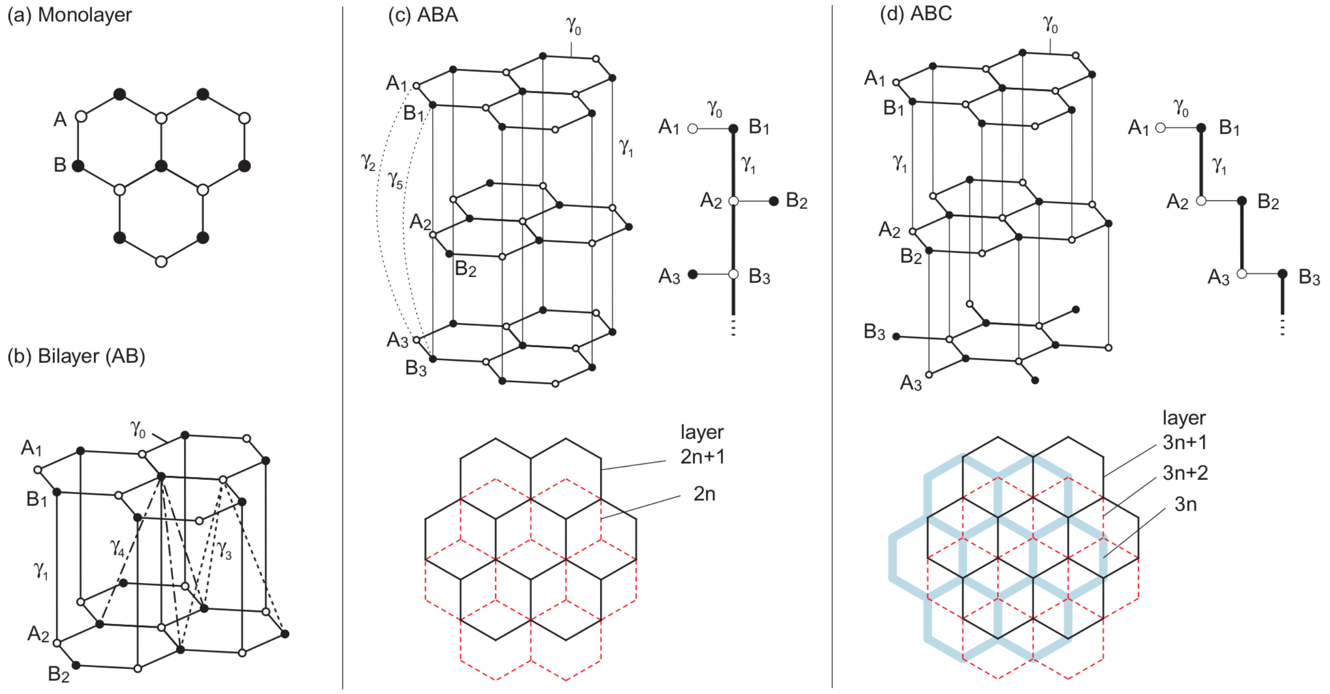

Figure 2.2: Lattice structures of (a) monolayer graphene, (b) AB-stacked bilayer graphene, (c) ABA-stacked multilayer graphene and (d) ABC-stacked multilayer graphene.[3]

The ABA arrangement results in a hexagonal crystal lattice (α-graphite) and the ABC arrangement in a rhombohedral one (β-graphite)[4]. The arrangement of the sheets in the β form carries an energy cost and as a result, pure rhombohedral graphite has been impossible to isolate and it is converted to hexagonal graphite when heated above 1600K[5]. On occasion and particularly when a sheet folds unto itself, an AA arrangement has also been observed[6].

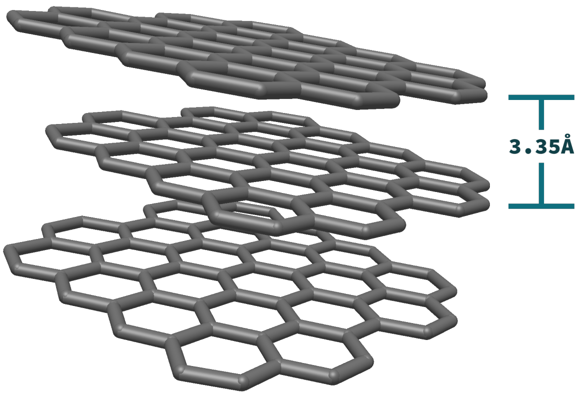

Image 2.1: Stacking of graphene sheets.

Having examined the structure of graphite, it is easy to comprehend why it is highly anisotropic. Phonons and electrons can travel rapidly across graphene sheets, but their propagation is considerably slowed down when moving in an interlamellar direction, or when they meet interstitial gaps in the crystal.

The three sp^2 orbitals of each carbon atom form strong σ bonds with its neighbors, giving graphene its excellent mechanical properties (breaking strength 42N·m^{-1}, Young modulus ~1TPa, third-order elastic stiffness -2TPa)[7]. The fourth valence electron, which would normally reside in the p orbital, becomes part of the practically infinite conjugated system and can move undisturbed across the graphene sheet. As a result, graphene exhibits ballistic transport, with an intrinsic mobility of 200000cm^2·V^{-1}·s^{-1}. These structural particularities also impart it a high thermal conductivity (∼5000W·m^{-1}·K^{-1}), a large surface area (2630m^2·g^{-1}), while the sheets themselves are almost transparent, with an optical transmittance of ~97.7%[8]. To put some of these properties in perspective, the 2010 Nobel Prize in Physics announcement by the Royal Swedish Academy of Sciences offered this tidbit about graphene: *"It is so strong, that a 1m^2 hammock, no heavier than a cat's whisker, could bear the weight of an average cat without breaking"*. That hammock would also be almost invisible.

As for its electronic properties, while graphene might appear to behave like a metal, it is actually a zero band gap semiconductor, with its valence and conduction bands (in effect, its π and π* molecular orbitals) touching (Figure 2.3a). As such, it displays an ambipolar electric field effect and its n or p character can be tuned with a variety of methods. The two-atom lattice results in two nonequivalent triangular sub-lattices throughout each sheet and this non-equivalence is responsible for the difference in stability and electronic behavior between "zig-zag" and "armchair" edges of graphene sheets[9]. These differences are even more pronounced in graphene nanoribbons, where the conjugated system is substantially smaller in one dimension[8–10].

A direct result of graphene's structure and electronic properties is its increased chemical inertness.

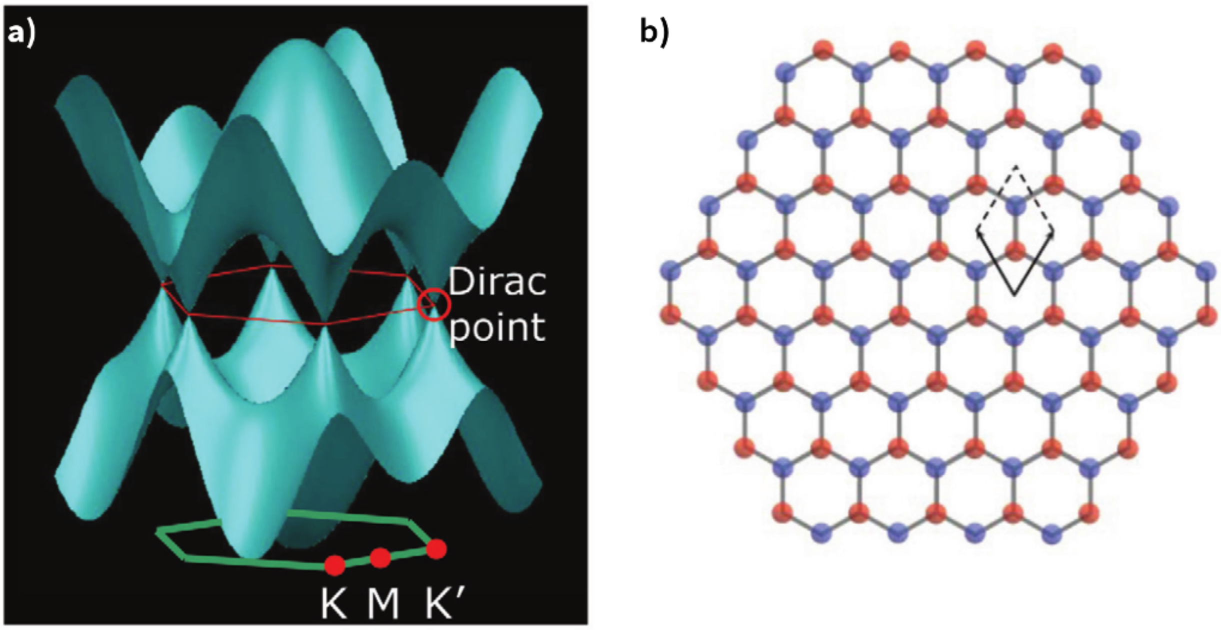

Figure 2.3: a) Representation of the electronic bandstructure and Brillouin zone of graphene. The conical shapes where the two molecular orbitals touch, are the so-termed Dirac cones. b) The two graphene sub-lattices (red and blue) and unit cell.[10]

Carbon nanotubes and fullerenes, two closely related materials, are substantially more reactive than graphene, because despite the stabilizing effect of the vast π system, the curvature of the lattice induces stress to the bonds and leaves the carbon atoms somewhat exposed e.g. to nucleophiles. This is not the case for graphene; the sp^2 bonds all lie on the same plane at the optimal, relaxed conformation of 120°, while the π system covers densely and evenly both sides of each sheet, leaving just the edge atoms available to reactants. Picking up an individual sheet and contorting it, which would alter its electronic properties[11] and hence its reactivity, is not entirely outside the realm of possibility, but obviously, it is not practical. There have been successful attempts to functionalize the basal plane of graphene by direct addition of e.g. dienophiles or free radicals[2,12], but this approach usually entails drastic, hazardous compounds and/or large amounts of energy. As a consequence, most researchers seeking to functionalize graphene prefer a different route, in which the first step is always the oxidation of graphene to graphene oxide (GO). This disrupts the π system, introduces defects and vacancies to the lattice and leaves many carbon atoms available to participate in further reactions. Of course, this is also detrimental to most of graphene's attractive properties, so more often than not, a final step in the process is the chemical or thermal reduction of the functionalized graphene oxide, in an attempt to restore the graphitic lattice as much as possible[13]. Cleaving a sheet of graphene, even mechanically, will result in the formation of new edges, which will readily react with the environment. Depending on the desired application and since graphene is, after all, an aromatic macromolecule, there is always the option of "decorating" graphene sheets with other species which can be adsorbed on its surface via π-π stacking or π-cation interactions. An interesting side-effect of the π system, is that graphene absorbs the excitations of adsorbed chromophores, thus "quenching" any luminescence.

It is often said that graphene possesses self-healing properties. The phase diagram of carbon (Figure 2.4), elucidates why this is true: under a wide range of temperatures and pressures and especially at standard conditions, graphite is the most stable allotrope of carbon. This includes not only graphene, but also the other known graphitic materials, namely nanotubes and buckminsterfullerenes. Given sufficient energy, the carbon atoms of any carbon-based substance will tend to get rid of

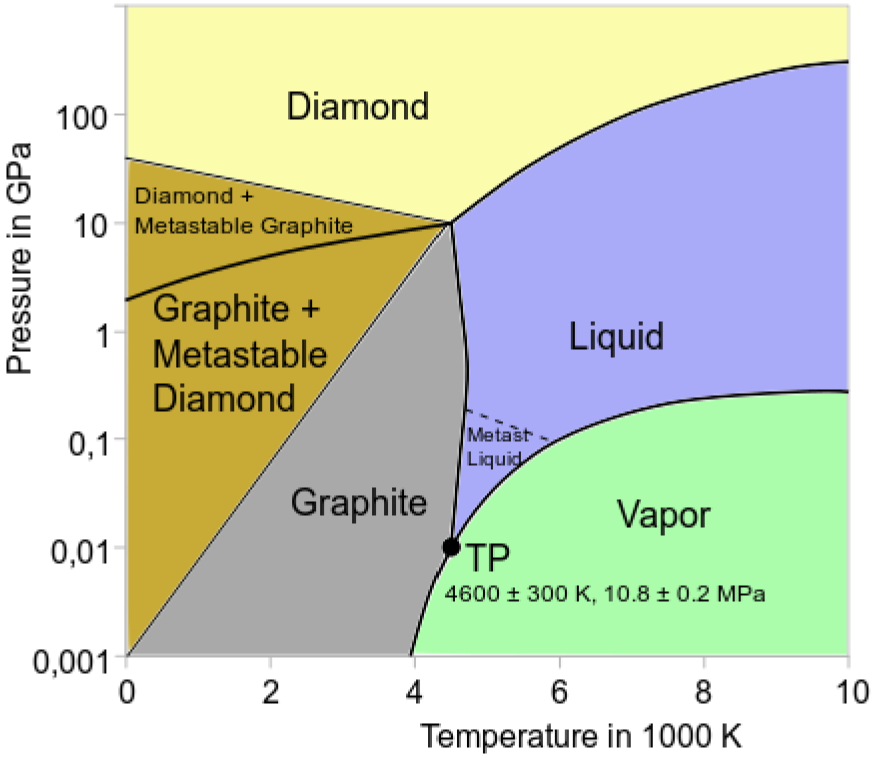

Figure 2.4: Phase diagram of carbon. The states for temperatures > 4000°C are derived from calculations.

other elements and form sp^2 bonds with their neighbors, eventually giving rise to that honeycomb lattice. By tuning the conditions, e.g. the speed of the process, the atmosphere in which it takes place, the shape/area of the surface on which carbon atoms can be adsorbed, etc., it is possible to favor the formation of one graphitic form over the other. By heat-treating a graphene sheet with defects or impurities, it will revert to its pristine state. This has also been observed in graphite crystals, where after the treatment, the edges of individual layers had fused together, forming larger, folded sheets[6] (Image 2.2).

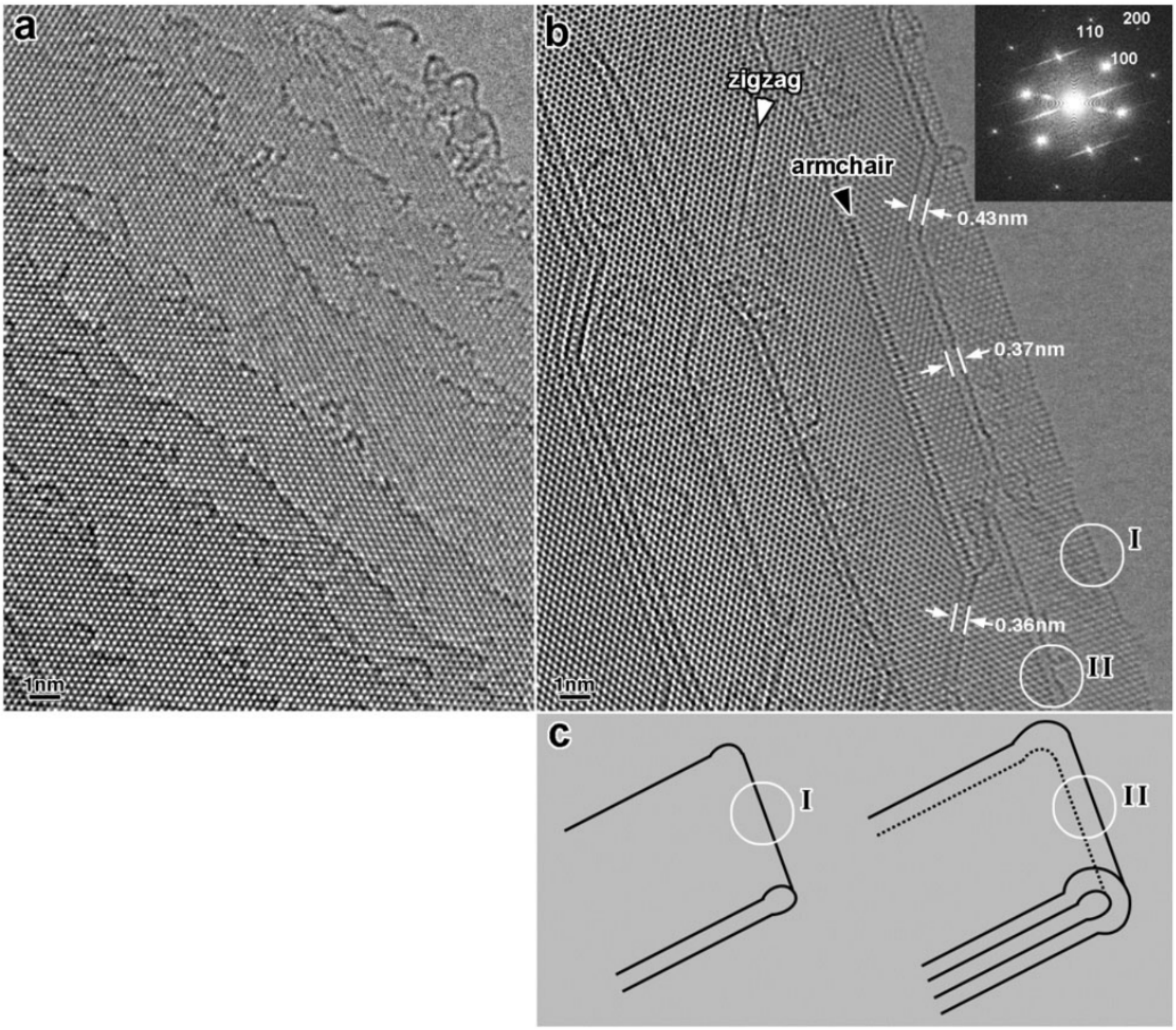

Image 2.2: a) HR-TEM image of graphite powders before heat treatment shows wavy edge structures b) HR-TEM image of the same powders after heat treatment (3h, 2000°C, vacuum) shows the straight edge lines. c) Each edge line corresponds to a closed edge of bilayer graphene.[6]

Graphene production

There are two strategies that can be employed to produce graphene: a top-down approach, with graphite as the starting material and a bottom-up one, where smaller, carbon-bearing molecules are used to form the graphitic lattice. The quality of the obtained material and consequently its properties are highly dependent on the method of production.

Exfoliation

In 2004, Geim and Novoselov resorted in a simple, yet ingenious method to isolate a single graphene layer from graphite: scotch tape. By sticking a length of scotch tape onto a piece of graphite, removing it and repeating the process with what was left on tape, they managed to end up with a single graphene layer, which they used in their experiments[1]. This technique is still used in laboratory settings and other than dissolving and washing away the adhesive tape, no other processing is required. The sheets of graphene obtained in this manner can be up to a few millimeters across, depending on the size of the crystallite.

In what has been termed “micromechanical cleavage”[14], researchers managed to drive an ultra sharp diamond wedge between graphite layers and ended up with few-layer graphene sheets, measuring several square micrometers. They had to encase the graphite crystal in epoxy, in order to keep it in place and the wedge was assisted by ultrasonication, so as to increase shear force[15].

It goes without saying that the above two methods do not scale up well, in fact they do not at all. When larger quantities of pristine graphene are required, exfoliation in the liquid phase is the only viable solution. Bulk graphite is dispersed in a suitable solvent and the mixture is subjected to either plain turbulence[16], or, more commonly, ultrasonication[17]. In either case, the energy transfer via the liquid medium exerts the necessary shearing forces to drive graphene sheets apart. The process can be further optimized by selecting a solvent whose molecules can be intercalated between the graphene sheets, by using surfactants or by adding polymers or fatty acids[18,19]. These additives increase the shearing forces by modifying the surface tension of the system or they help stabilize the resulting dispersion, so that it may be stored and used later, or both. Liquid phase exfoliation is not without its drawbacks too: The energetic process used to exfoliate graphene can also result in the tearing of the sheets, reducing their size. Completely removing the solvent without having the graphene sheets stacking up again can be a challenge. Separating the graphene layers from the surfactants and other additives is an even bigger challenge.

When the overall process calls for oxidation of graphene/graphite, it is possible to almost completely forgo the aforementioned treatments. As the oxidation progresses, the graphitic lattice is deformed. At the same time, oxygen-bearing groups such as epoxides are formed further and further inside the basal planes and these act like small wedges, pushing adjacent layers apart[20]. These two factors help minimize the interactions between neighboring sheets, making it easier for solvent molecules to penetrate between them on one hand, while reducing the energy requirements for complete exfoliation on the other.

Synthesis

Chemical vapor deposition (CVD) is the most prominent method for the production of pristine, large-area graphene sheets, even on an industrial scale[21–23]. Small precursor molecules, such as methane, ethane, acetylene, etc., flow into a furnace, where they thermally decompose. The carbon atoms, free from hydrogen and other substituents, latch onto a suitable surface, such as a metal foil and the graphitic lattice starts growing from there, as more molecules flow into the furnace. The graphene sheet is then removed mechanically or by chemically destroying the catalytic substrate. This process can be combined with roll to roll pressing and transfer, in order to produce graphene sheets of arbitrary length[22] (Figure 2.5).

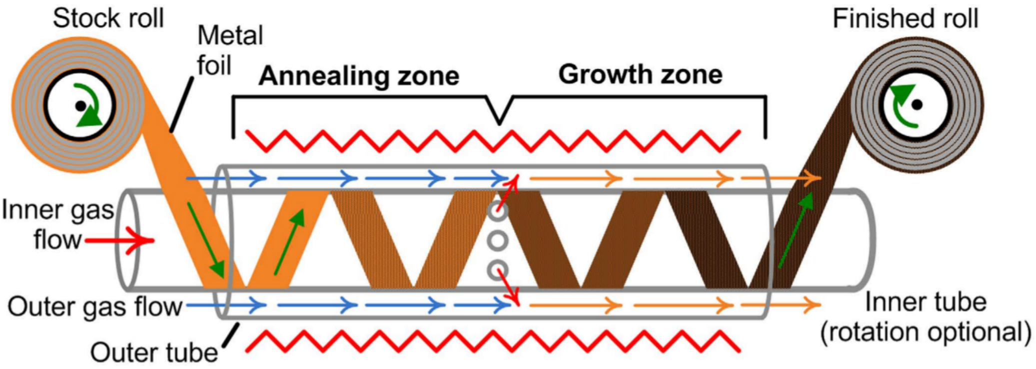

Figure 2.5: Schematic of a concentric tube CVD system configured for roll-to-roll graphene growth on Cu foil[22].

Another way to produce sheets of fixed dimensions is by the thermal decomposition of SiC crystals. The process starts with a 6H-type crystal grown or cleaved along the (0001) surface, which is then heated up to 1500°C in a vacuum or inert atmosphere. The heat causes silicon atoms to evaporate away from the lattice and the remaining carbon atoms are joined together, forming sheets of graphene. For the 6H carborundum crystal, approximately three layers of Si need to evaporate for a single graphene layer to form[24].

It is possible to obtain graphene-like structures from the reduction of CO_2. The gas reacts with alkali metals in a closed reactor under heat (500°-600°C) for prolonged periods of time. However, the resulting products are in powder form, three-dimensional and contain a large number of defects[25,26].

A very different, interesting, but also painstaking approach is the chemical synthesis of graphene sheets, quantum dots, nanoribbons and other structures, starting from small polycyclic aromatic hydrocarbons. By careful selection and

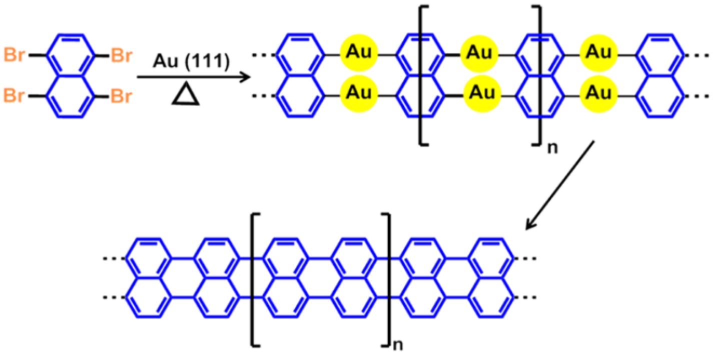

Figure 2.6: On-surface synthesis of rylene-type graphene nanoribbons[27].

design of the precursor molecules, it is possible to end up with graphene in a variety of shapes and forms, of fixed, but also of almost infinite dimensions, using common reactions (Figure 2.6), such as the Diels-Alder cycloaddition, cyclodehydrogenation and polymerization[27,28]. Needless to say that just figuring and designing the synthetic pathway is in itself a huge amount of work. Also, at the end of such a synthesis, graphene needs to be removed from a substrate or separated from stacked aggregates.

Some researchers have proposed solvothermal synthetic methods[29] for the production of graphene, but the end product needs to be exfoliated. While such methods do have their merits, especially if graphene is to be doped with heteroatoms or other functional groups, when it comes to graphene production, they do not differ much from the methods used to produce synthetic graphite; they just traverse into the graphite area of the phase diagram with a different slope (e.g. lower temperature, higher pressure).

Graphene doping

The term “doping” originated in the field of semiconductors and refers to the introduction of defects or impurities in a bulk semiconducting material, intended to modify its n or p character. This was contrasted with “surface modification” – a self-explanatory term. In the case of 2D materials, they are both practically indistinguishable, as there is no third dimension and the surface also makes up the bulk of the material.

Based on what has been discussed so far, it is easy to see the available routes towards graphene doping. When graphene is synthesized or “grown”, e.g. via CVD, it is possible to introduce another component or mix of components in the reaction chamber. This technique has been employed in the synthesis of boron and nitrogen-doped graphene[30]. Introduction of the same dopants in the graphitic lattice has also been achieved using the more “chemical” approach, of having suitable precursors undergo simple reactions[31,32].

When the desired carbon-dopant bond has a higher enthalpy of formation, that what can be achieved with CVD or other “milder” methods, but not only then, pyrolysis of suitable precursors is always a possibility. A representative example involves the formation of P and PO-doped graphene by pyrolyzing alginate coordinated with dihydrogen phosphate[30].

A third general strategy to graphene doping relies on its self-healing, or, more accurately put, its energy-assisted healing. After creating defects or vacancies in the lattice, e.g. via oxidation (the GO route) or other methods, graphene is annealed in an atmosphere containing the dopant, or it is co-annealed with it in an inert atmosphere. Examples of this strategy include the production of N-doped graphene after irradiation with N^+ ions and then annealing in NH_3[33] and the production of S-doped graphene by annealing a mixture of GO and benzyl disulfide in Ar[34]. A conceptually similar approach combines the chemical restoration of the lattice and doping in a single step, as in the case of the reduction of GO in a borane/THF solution, which yielded boron-doped graphene[30].

Several other techniques have been reported in the relevant literature, such as playing billiards with ions and lattice atoms[35], but since on one hand this sub-chapter is not meant to be an exhaustive list of every method researchers have used to dope graphene and on the other, such methods are not of practical use to an average chemist, nor do they possess any tangible advantage over what has already been presented, they will not be discussed here.

Graphene oxide

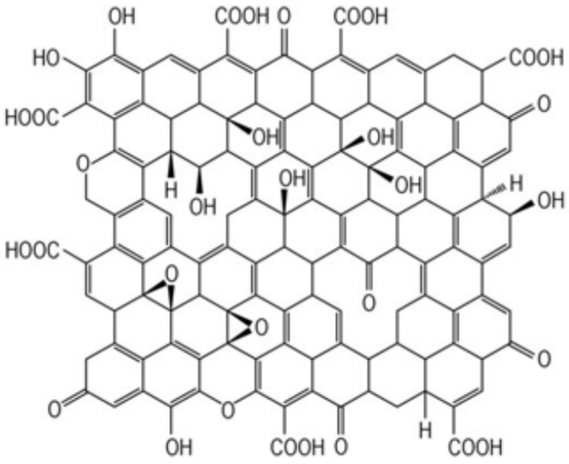

Figure 2.7: A typical depiction of graphene oxide, with vacancies and various oxygen-containing functional groups[43].

The oxidation of graphite was first reported by Brodie in 1859, who gave a vivid description of the material and its properties: *“The substance after the acid has been washed from it by water, has much the appearance of graphite itself, but is darker in colour. […] when heated it undergoes a remarkable change; gases are given off in the interior of the substance, which swells up in a most singular manner and is reduced to the minutest state of division. The residue consists of carbon, which has the appearance and the structure of the lamellar graphite. […] I found that graphite, when heated with a mixture of nitric acid and chlorate of potash, increased in weight, and that the substance formed was, on the application of heat, disintegrated with evolution of gas. The disintegrated substance differed but little in appearance from the original graphite.”*[36] The Brodie oxidation method, though no longer used in the industry, is still on occasion employed in the laboratory. As Brodie noticed, graphene oxide is darker in color than graphite, heavier than the starting material and it decomposes when heated with the simultaneous evolution of gas – mainly CO_2, but also water and CO. The lamellar structure of graphite is retained despite the oxidation, but the distance between adjacent sheets is larger, compared to that in graphite, as evidenced by X-ray diffraction patterns. The oxide contains sp^2 as well as sp^3 carbon atoms, so the neat, planar arrangement found in graphite is lost and the individual sheets are often more wrinkled

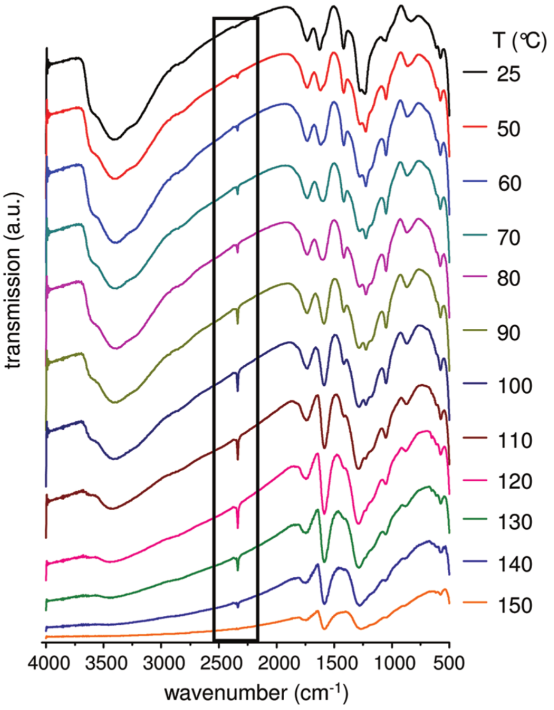

Figure 2.8: Evolution of CO_2 from GO, as it is annealed at temperatures between 25°-130°C in Ar. The marked peak corresponds to the asymmetric stretching of the C-O bonds in CO_2 (FTIR spectra)[37].

than graphene. These structural and electronic alterations result in GO being an insulator. Recent measurements have shown that the evolution of CO_2 can start in temperatures as low as 50°C (Figure 2.8). The gas that forms at these temperatures remains trapped between the sheets, until the heat is raised to 130°C, at which point occurs the explosive exfoliation of graphite oxide to graphene oxide[37]. This is what Brodie described as *“the minutest state of division”*.

Brodie's oxidation method involved mixing graphite with $KClO_3$, adding fuming HNO_3 and keeping the mixture for 3-4 days at 60°C in a water bath. This was then thrown in a large quantity of water, filtered, washed and dried and then submitted anew to the same process, for at least four times[36]. In 1898 Staudenmaier proposed another method in which $KClO_3$ was slowly (over the period of one week) added to a mixture of concentrated H_2SO_4, concentrated HNO_3 and graphite. The container needed to be kept cool and as ClO_2 was a byproduct of the reaction, posing a constant explosion hazard (it may explosively decompose into chlorine and oxygen), an inert gas was used to purge it away[38]. A safer and faster alternative was invented by Hummers and Offeman in 1958. Their oxidation method consisted of mixing graphite with $NaNO_3$ in concentrated H_2SO_4 and then adding $KMnO_4$, while keeping the reaction container in an ice bath. The ice bath was then removed, warm water was added to the mixture and after a while, a solution of 3% H_2O_2, in order to reduce any residual MnO_4^{2-} and MnO_2. The resulting suspension was further diluted, filtered and washed. It is worth noting that the oxidation part of the process was completed in under 2 hours[39]. For decades, these three methods, sometimes with small variations, have been used for the production of GO on any scale. Recently, two new approaches have appeared in the literature: The first, by Peng et al., is a “greener”, even faster alternative to the Hummers method. It substitutes K_2FeO_4 (a highly reactive and rare example of an iron(VI) compound) for $KMnO_4$. Potassium ferrate has a higher electrode potential, which allows the oxidation to proceed much faster and complete in just under an hour. As it does not produce any explosive intermediates, it can be used safely in temperatures up to 100°C. In addition, any resulting byproducts are environmentally friendly and the remaining sulfuric acid can be reused at least 10 times, without any loss in process efficiency or GO quality[40]. The other method, proposed by Tang et al., takes a radically different approach, in that it is in essence a direct, bottom up synthesis of GO. The researchers have succeeded to synthesize graphene oxide nanosheets via a simple hydrothermal method, with a glucose solution in water as the starting material. They have demonstrated that by varying the reaction and annealing times and temperatures it is possible to obtain GO sheets of tunable size, thickness and oxygen content[41].

It must be noted that graphene/graphite oxide is not a stoichiometric compound. The oxygen content, the quantity and quality of functional groups and the amount of each group in the basal plane or the edges of the graphene sheets are highly dependent on the oxidation method, the reaction time, the quality of the starting material and any pre or post-treatments. As demonstrated in Figure 2.7, the oxygen-bearing functional groups that may be present in graphene oxide, commonly include carboxyl and hydroxy groups, epoxides, ethers and lactones. The amount of groups capable of forming hydrogen bonds plays an important role in the hydrophilicity and the stability of GO suspensions in polar solvents, though in general and unlike graphene, GO is described as hydrophilic[42].

Graphene oxide may lack some of the features that helped in graphene's rise to fame, but it possesses some interesting properties of its own. One potential application that is based on them is water treatment. In fact, graphite oxide had been considered for such use long before the discovery of graphene, in the 1960s. GO either right after oxidation, or after partial reduction can form networks between the sheets, which allow only water to flow through them, under pressure or via reverse osmosis[43]. Recently, it was reported that the same principle could be applied for the purification of other solvents, by tuning the width of those networks[44].

There is an unsettled debate whether GO is actually a one or two-component system. This stems from the observation that when GO is washed with a strong base, e.g. NaOH, the bulk of the material sediments and the remaining liquid is a solution of several acenes and other polyaromatic hydrocarbons, heavily substituted with oxygen-containing groups, collectively referred to as oxidative debris (OD). This has led some researchers to believe that GO is actually a two-component system, with the OD adsorbed onto the much less oxidized sheets. Though a number of characterization techniques disprove that theory, the matter warrants further investigation[45,46].

Reduced graphene oxide

Reduced graphene oxide (rGO) – also a non-stoichiometric compound – can have properties that range anywhere between those of pristine graphene and graphene oxide, depending on the amount of effort that has gone into the restoration of the lattice. For example, it can be an insulator like GO, conducting like graphene or semiconducting. Its behavior is determined by the ratio between sp^3 and sp^2 regions in the sheets, as well as the number of other residual defects, namely vacancies and functional groups. Given that one usually goes through all the trouble of oxidizing graphene in the first place in order to functionalize the material and that with sufficient energy the carbon atoms become real “xenophobes”, ditching every heteroatom and bonding with their peers, it is not typical to allow the reduction to proceed to completion. If the material is thermally annealed and the application calls for a specific property, e.g. band gap, the temperature and the duration of the procedure need to be carefully selected and that entails some trial and error. Chemical reduction is easier to control and it should be the preferred method when the aim is mainly the removal of excess functional groups.

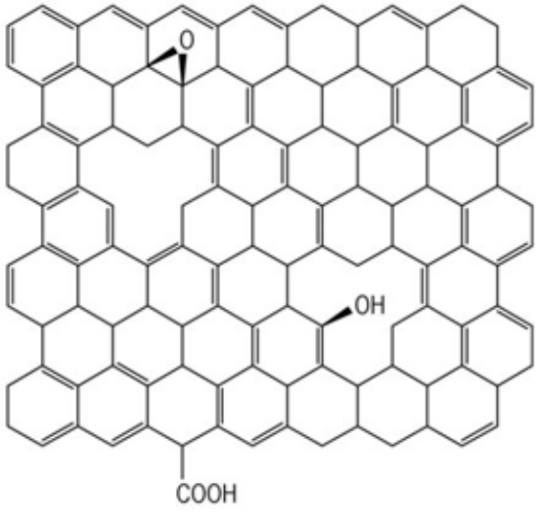

Figure 2.9: A typical depiction of reduced graphene oxide, with some vacancies and a few leftover oxygen-containing functional groups[43]

The reduction process and its progress have been examined extensively by several groups and with various techniques. Nikolakopoulou et al.[47] studied the thermal transformation of GO to rGO on FTO glasses with XPS, after annealing the samples at various temperatures for 15 minutes (Figure 2.10):

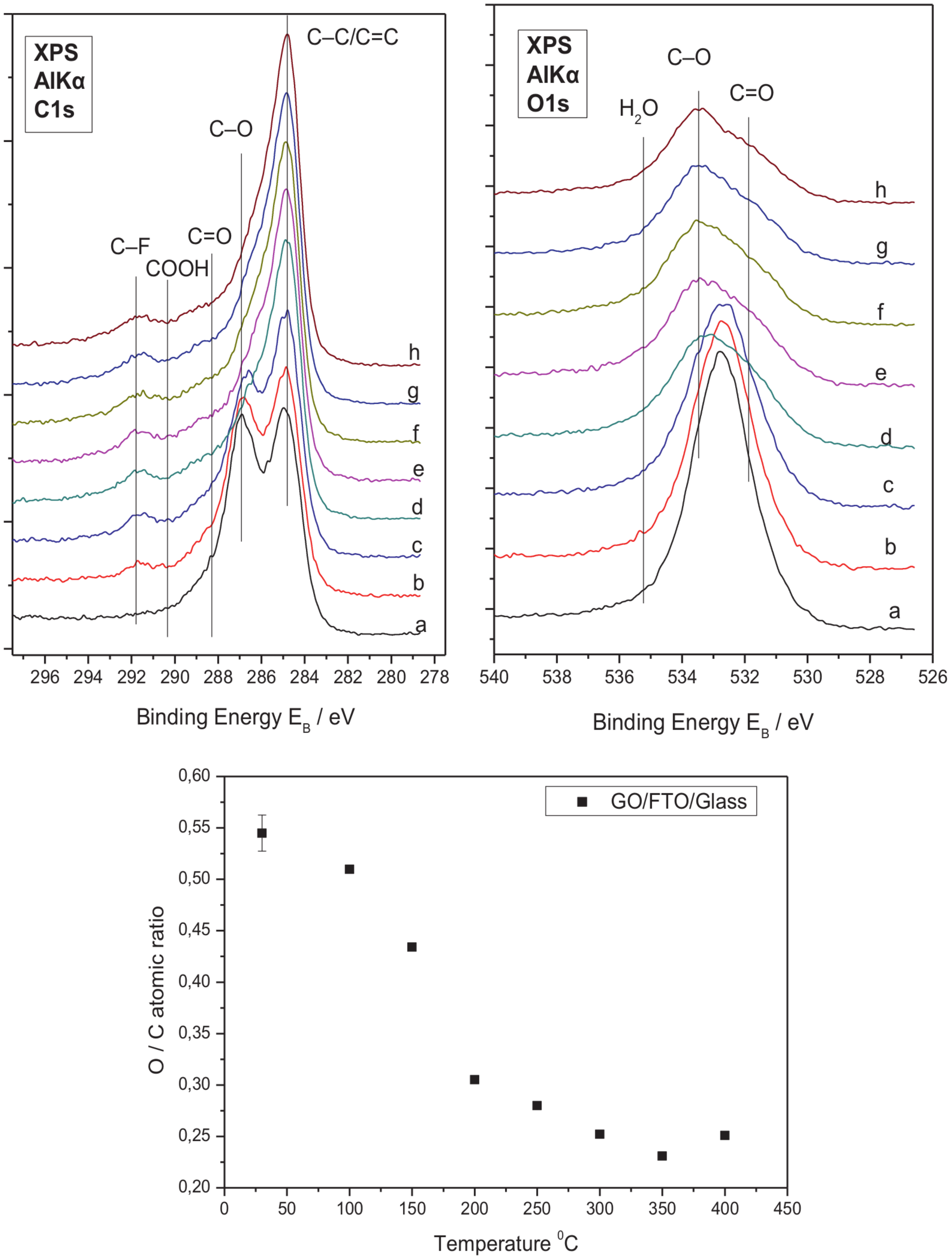

Figure 2.10: Top: C1s (left) and O1s (right) XP spectra of GO on FTO/Glass as deposited (a) and after heating in UHV for 15 min at (b) 100°C, (c) 150°C, (d) 200°C, (e) 250°C, (f) 300°C, (g) 350°C and (h) 400°C. Bottom: The corresponding O/C atomic ratio of the same samples.[47]

While one might draw some general conclusions from such studies, again, it should be noted that the reduction profiles of different samples of GO depend largely on the oxidation method and an array of other factors. For example, Nikolakopoulou et al. found that decarboxylation is not noticeable in annealing temperatures up to 200°C, whereas in the Eigler study[37], it is evident from the FTIR spectra that as the CO_2 signal increases, the characteristic peak of the carboxyl O-H stretching wanes. However, the Eigler group used the Hummers oxidation method and the solid material was obtained with freeze-drying; Nikolakopoulou followed a different protocol, which involved a pre-oxidation step and the solids were isolated after evaporation at 120°C.

Cobalt(II) phthalocyanine

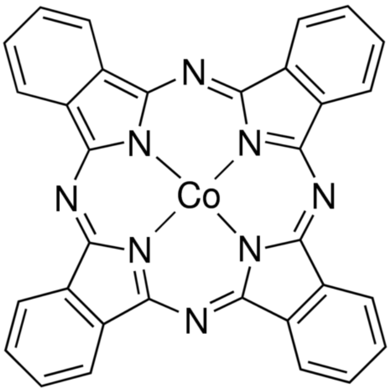

Figure 2.11: Structure of cobalt(II) phthalocyanine.

Phthalocyanines (Pcs) are aromatic macrocyclic compounds, that are closely related to porphyrins and porphyrazines. These structures or fragments are often found at the center of biologically active molecules, such as chlorophyll and hemoglobin, which makes them prime candidates for – among other uses – various biomimetic applications. For this reason, phthalocyanines have been employed as catalysts and because of their deep blue color, they have been used extensively as dyes and pigments.

The chemistry of phthalocyanines is interesting enough to the extent that there is a scientific journal devoted entirely to them and porphyrins. They are planar in shape, with an aromatic system throughout the molecule. They bind tetradentally to metals, in octahedral and – more commonly – square planar complexes, contributing up to eight electrons (one pair from each of the internal nitrogen atoms) to the outer molecular orbitals.

They dissolve very poorly in water and common organic solvents; they are more soluble in acidic solutions, primarily due to the protonation of the nitrogen atoms that bond the pyrrole rings together[48]. Their solubility can be increased via substitution, but that affects their overall stability, as well as their optical properties.

The extended π system of phthalocyanine can stabilize the molecule well enough for it to undergo reversible redox reactions. Metallated phthalocyanines can take part in redox reactions either through their ring or through the metal center (or both). If there are empty or full metal d orbitals between the HOMO – LUMO orbitals of the Pc ring, the metal ions can be reduced or oxidized respectively before the ring[49].

Unsubstituted phthalocyanines possess another remarkable property, especially considering their organic nature: they are surprisingly thermally stable. At high temperatures (and under an inert atmosphere), instead of decomposing, they sublime. While precise measurements are scarce, PcCu has been found to be stable at 580°C[50], a compound molecule consisting of two PcNi units joined by two diacetylene moieties through the phenyl rings was reported stable at 700°C[51] and we managed to retrieve needle-like PcCo crystals from a sample that had been heat-treated at 700°C for an hour:

Image 2.3: Needle-shaped crystals of PcCo.

The spectra of phthalocyanines in various bands have also been studied and while it is relatively easy to assign specific vibrations to IR and Raman peaks, even though their spectra are rather complex, things are considerably more difficult in other parts of the EM spectrum. Several metal-Pc complexes display features that can not be adequately described by theoretical interpretations[49,52–54].

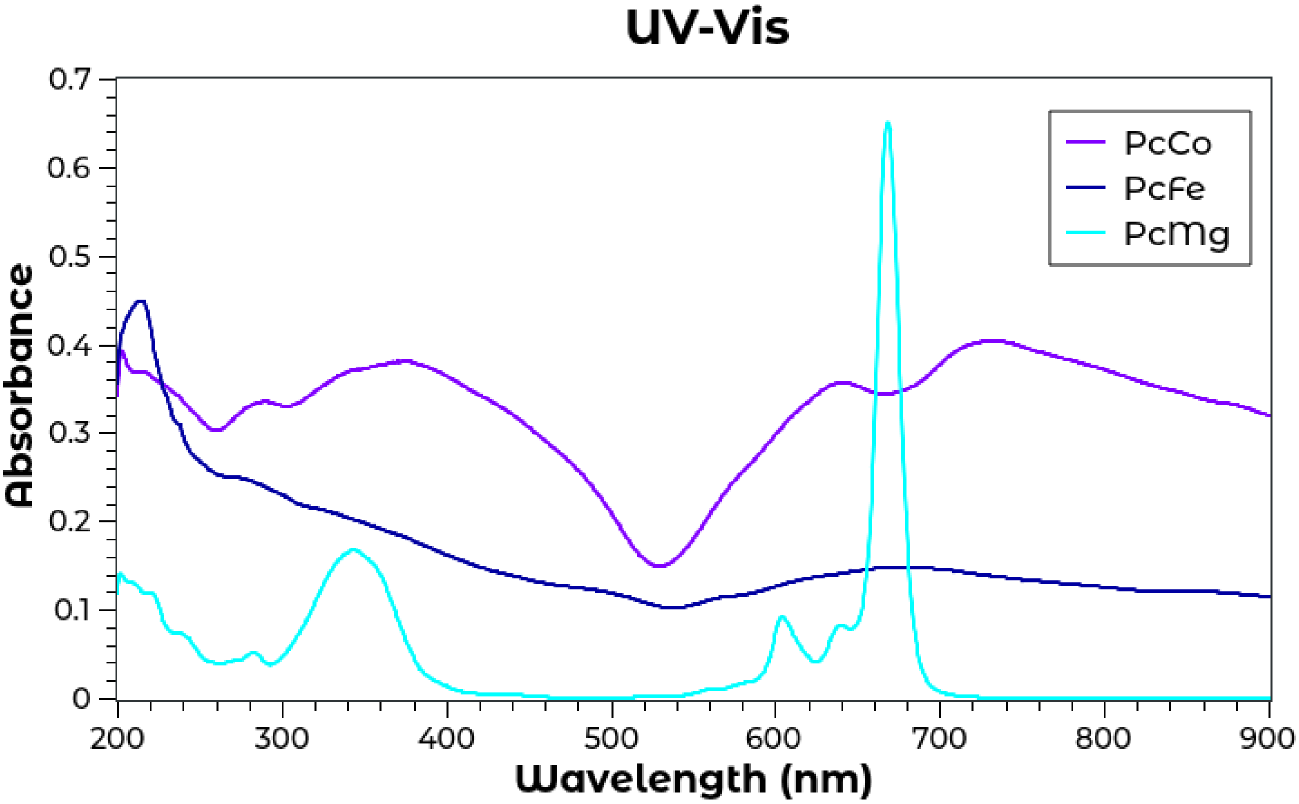

Figure 2.12: UV-Vis spectra of Pcs used in this work, dissolved in isopropanol.

Monolayers and oligolayers of phthalocyanines are usually flat, but that depends on the nature of the surface on which they are deposited. As larger crystals start to form, they adopt either a herringbone arrangement or they are stacked slanted in molecule-wide columns (Image 2.4), or something in between; there are at least five known polymorphs of cobalt(II) phthalocyanine (PcCo).

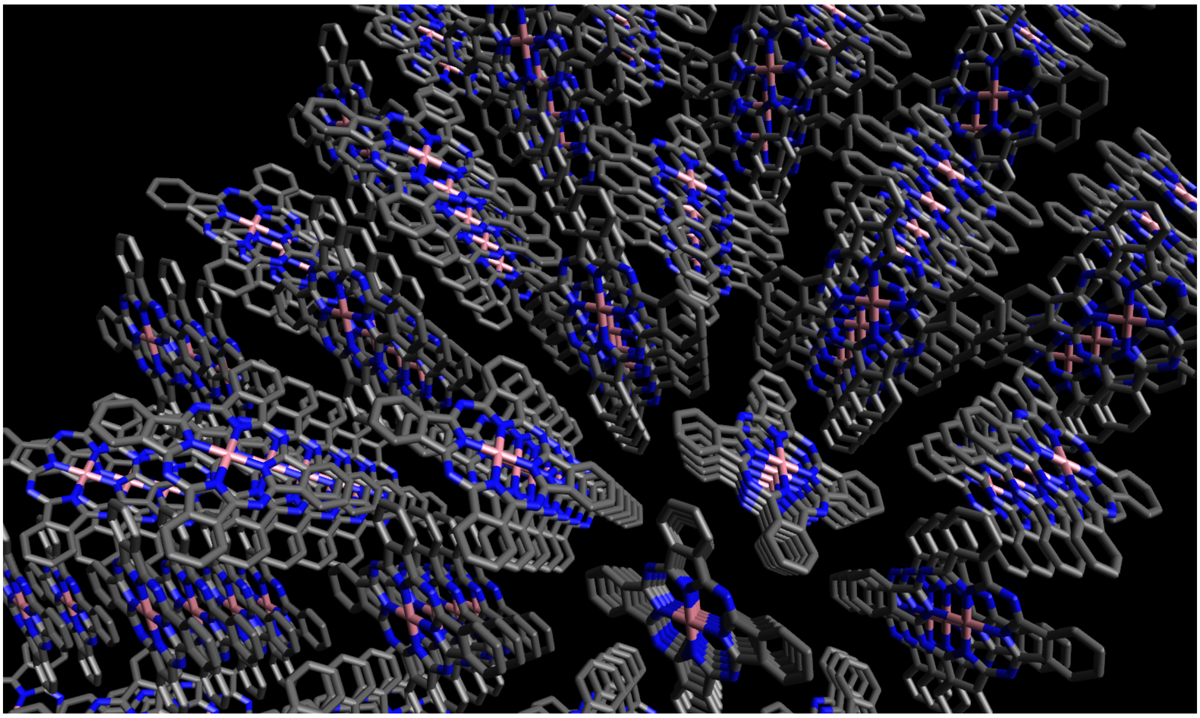

Image 2.4: Rendering of a monoclinic PcCo crystal. Original crystallographic data obtained with neutron scattering and deposited at the Crystallography Open Database (COD ID: 2100746).

Phthalocyanines and porphyrins have been used in DSSCs, primarily as dyes[55]. Their low solubility is actually an asset in that role, as this makes it difficult for them to be desorbed from the semiconducting substrate by the electrolyte solution. Substituted, metal-free and metallated phthalocyanines have also been used in organic solar cells[56] and in MOF-based solar devices[57], demonstrating their light-harvesting and charge transport capabilities.

Cobalt(II) phthalocyanine is a low-spin (S=½) paramagnetic complex. Because of its unpaired 3d electron (from which its paramagnetic character is derived, see Figure 2.13), it has been described as a molecular magnet[54]. In solid form, the color of PcCo ranges from deep blue to deep purple, depending on the polymorph. Its solutions and suspensions are blue-colored.

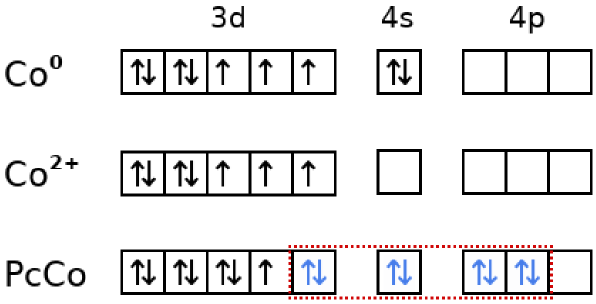

Figure 2.13: Electron configurations of cobalt (top), its +2 cation (middle) and of PcCo (bottom).

Poly(3,4-ethylenedioxythiophene)

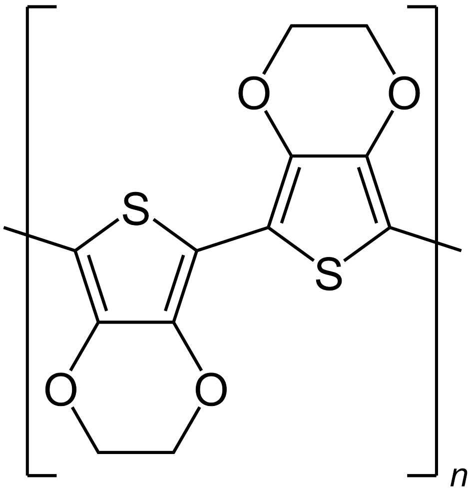

Figure 2.14: Structure of the alternating EDOT monomers in PEDOT.

Poly(3,4-ethylenedioxythiophene), commonly abbreviated as PEDOT, is a transparent conducting polymer. Its conductivity is the result of an extended, conjugated system along the polymeric chain, in which – due to steric effects – EDOT monomers alternate above and below the main axis. PEDOT is highly stable, in a variety of solvents, pH and temperature ranges. It has a low redox potential, maintaining its optical transparency even in an oxidized state and it has a reduced band gap. As it is both chemically stable and conducting, it can be used to coat electrodes and contacts, protecting them from corrosion, without hindering charge transfer. In the same vein, PEDOT can be added to electrodes and surfaces, on which active species have been deposited (e.g. quantum dots), achieving simultaneously an enhancement of their function, as well as their protection from the environment.

All of these properties make PEDOT ideal for innumerable electronic and optoelectronic applications (solar cells, (O)LEDs, photodetectors, analytical techniques, etc.). However, after its formation, PEDOT is very poorly soluble in most solvents. In the past, this had been circumvented either by modification of the polymeric chain (like in PEDOT-TMA) or by mixing it with a soluble polymer (such as PEDOT:PSS). In recent years, a third route has emerged as a preferred alternative: electrogeneration or electropolymerization. This procedure allows for a very fine control over the texture and thickness of the polymer layer, which is synthesized from aqueous or organic solutions of EDOT monomers, directly onto the surface to be coated. Unlike “traditional” polymerization or the aforementioned solubilization strategies, which are susceptible to convection and diffusion phenomena and which usually result in uneven, “lumpy” coats, by carefully selecting the aspects of the current used in electropolymerization, it is possible to produce very uniform and almost defect-free films, with nanometer precision.

PEDOT can also be combined with graphene and graphene derivatives, to improve upon their conductivity. As we have already seen, gaps between graphene sheets and residual defects in rGO can be an issue, in particular when high conductivity is a requisite. Application permitting, the addition of a layer of PEDOT over a film of such materials can boost their charge transfer, by providing more avenues for electrons to travel.[58–62]

The state of the art

Before we set out on our efforts, and while the work progressed, we did keep a keen eye on the literature covering the advances made in the last nine years or so, in the field of graphene-based counter-electrodes for DSSCs. A review of the most noteworthy of these works (excluding systems that used redox pairs other than I^-/I_3^-) was recently published[63]; here follows a summary of that overview.

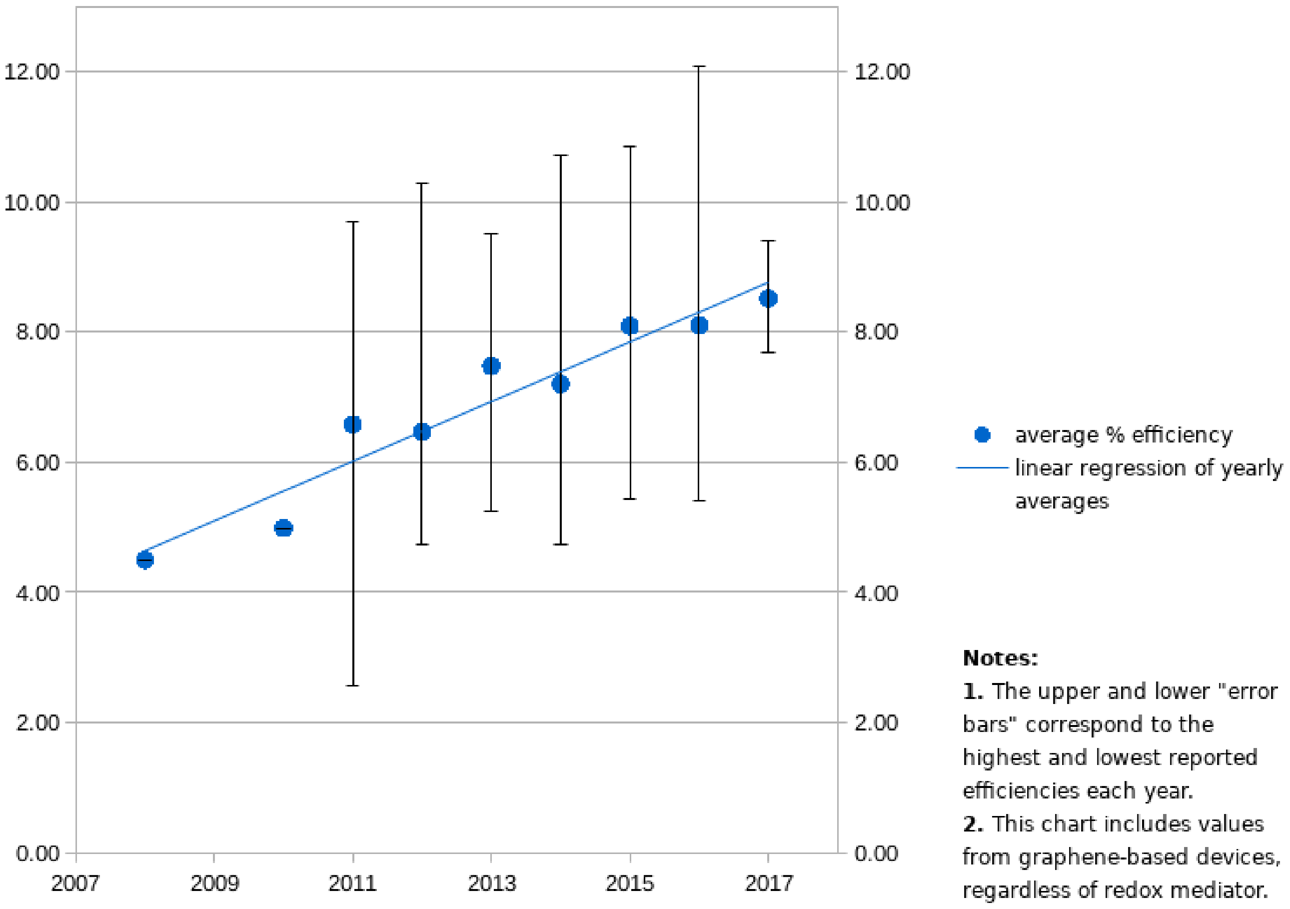

Notes:
1. The upper and lower "error bars" correspond to the highest and lowest reported efficiencies each year.
2. This chart includes values from graphene-based devices, regardless of redox mediator.

Figure 2.15: Reported efficiencies of graphene-based DSSC devices since 2008. Data points gathered from ~200 articles, spanning almost a decade.

On average, reported efficiencies have been slowly, but steadily increasing every year, since 2008 (Figure 2.15). The current record holders are Wei et al.[64], whose device achieved a conversion efficiency of 11.03%. In the time span we examined (2008 to mid-2017), the highest reported efficiencies were 4.5%, 4.99%, 6.81%, 7.07%, 9.54%, 10.71%, 9.39%, 11.03% and 9.4%.

The testing methodology used to assess these devices has somewhat converged to a minimum battery of tests over the years, but there are still many points that need to be improved upon before one is able to draw direct comparisons between materials. For one, not everybody tests their cells under the same irradiation conditions; most research groups opt for an air mass coefficient of 1.5, which corresponds to the spectrum of the Sun's radiation that reaches the Earth in temperate latitudes (actual solar zenith angle z=48.2°), others use AM1, which corresponds to conditions at the equator, while some just report the wattage of the lamp they used. Measuring the charge transfer resistance of a device will reveal how much energy will be lost as heat when the device is in operation and can hint at phenomena that take place at the nanoscale. Here too, approaches vary. One would assume that the testing apparatus should be as close an approximation of the actual device as possible, which entails fabricating electrodes similar to those used in the cells, as well as submerging them in the same electrolyte solution. Most researchers do take that route and report the sheet resistance of their materials. However, some take surface conductivity measurements, others report specific resistivity without mentioning film thickness and few just provide a simple resistance readout. A third point of contention, but of lesser consequence, is the Pt reference electrode and the effort that has gone into its fabrication, when it has not been purchased directly from a manufacturer. On the bright side of things and perhaps in part due to the peer review system, such discrepancies are becoming increasingly rare.

Other than the fact that all the materials in the portion of the literature that we examined had to be graphene-based, they were actually quite diverse, although they do fall under three very broad categories: almost half of them contained metals in a variety of shapes and forms, some were graphene (either doped or pristine)/polymer composites and the third variety includes graphene structured in unusual conformations. Of course there were combinations of the above.

As for the synthetic procedures, they ranged from the ingeniously simple to the magnificently elaborate. These are some generalized examples:

- Ball-milling or pin-grinding graphene in the presence of a dopant.
- Co-annealing graphene oxide with a dopant.
- Pyrolysis/graphitization of an organic precursor along with a substance containing the desired heteroatoms.
- One and two-step solvothermal/hydrothermal reactions between dopant precursors and graphene oxide.
- Treatment of GO with plasma jets.
- Polymerization of monomers mixed with graphene/GO, annealing of the mixed-matrix material and partial decomposition, followed by electrodeposition of a conducting polymer.
- Reduction of CO or CO_2 over molten alkali metals.
- Fashioning GO into a paste, impregnating it with metal oxide precursors and reducing the mixture with plasma.
- CVD growth of graphene, followed by dip-coating in dopant solution and annealing.
- CVD growth of graphene in a fluidized bed and plasma treatment.

The following table lists the electrocatalytic performance data for some of the most noteworthy counter-electrode materials:

Table 2.1: Electrocatalytic performance data for some of the best performing counter-electrode materials. In bold: highest reported efficiency, open circuit voltage and short-circuit current.

Year	**Counter electrode material**	**η (%)**	**η_{Pt} (%)**	**V_{OC} (V)**	**I_{SC} (mA·cm^{-2})**
2011	Ti nitride – n-doped rGO (TiN/NG) hybrid[65]	5.78	5.03	0.728	12.34
2011	Pt nanoparticles/rGO hybrid[66]	6.35	5.27	0.79	12.06
2013	rGO nanoribbons/CNT hybrids[67]	8.23	7.61	0.734	16.73
2013	Electrochemically Reduced Graphene Oxide Multilayer Films[68]	9.54	9.14	0.692	18.77
2013	NiS$_2$/rGO nanocomposites[69]	8.55	8.15	0.749	16.55
2014	Quasi core-shell nitrogen-doped rGO/cobalt sulfide[70]	10.71	9.73	0.71	20.38
2014	Edge-carboxylated graphene nanoplatelets[71]	9.31	8.67	**0.889**	14.07
2014	p-Doped (N & O) 3D graphene networks[72]	8.46	7.98	0.713	17.2
2014	3D cauliflower-fungus-like rGO[25]	8.07	7.5	0.79	19.04
2015	CoS/rGO hybrid film[73]	9.39	7.34	0.764	19.42
2015	N-doped rGO nanoribbons[74]	8.57	7.84	0.78	15.18
2015	PEDOT-decorated nitrogen-doped graphene[75]	8.3	8.17	0.739	15.60
2016	N-doped rGO – FeN core-shell nanoparticles[76]	10.86	9.93	0.74	18.83
2016	N-doped graphene nanosheets with active metal (Co) sites[77]	8.4	7.98	0.72	17.32
2016	CoS/rGO hybrid[78]	9.82	8.24	0.767	18.903
2016	B,N co-doped rGO[79]	8.08	6.34	0.77	15.3
2016	CoSeO$_3$·2H$_2$O with traces of rGO[80]	9.89	8.39	0.747	19.94
2016	Pt-Ru nanoparticles supported on rGO[81]	8.44	7.54	0.745	16.25
2016	3D flower-like graphene made from CO$_2$[26]	10.1	7.7	0.78	19.29
2016	TiS$_2$-rGO hybrids[82]	8.8	8	0.72	17.76
2016	Electrochemically exfoliated graphene/PEDOT composite films[83]	8	7.7	0.64	**22.8**
2016	Thin films of graphene flakes produced by thermal plasma jet[84]	9.03	9.07	0.78	16.25
2016	rGO hybrid with a macrocyclic Ni complex[85]	8.3	7.96	0.75	17.8
2016	N & P co-doped rGO[86]	8.57	7.58	0.77	15.91
2016	Highly conductive porous Na-embedded carbon[64]	**11.03**	7.89	0.8	20.95
2017	PtMo alloy on rGO[87]	9.11	8.03	0.745	18.73
2017	N-doped holey graphene[88]	9.07	8.19	0.744	17.19
2017	3D N & S co-doped rGO networks[89]	9.4	9.1	0.744	16.86
2017	Porous S-doped rGO[90]	8.67	7.88	0.75	16.70

Where: **η** = conversion efficiency, **η_{Pt}** = conversion efficiency of the Pt reference counter-electrode, **V_{OC}**= open circuit voltage, **I_{SC}**= short-circuit current

Chapter Bibliography

[1] Novoselov, K. S.; Geim, A. K.; Morozov, S. V.; Jiang, D.; Zhang, Y.; Dubonos, S. V.; Grigorieva, I. V.; Firsov, A. A. Electric Field Effect in Atomically Thin Carbon Films. *Science* **2004**, *306* (5696), 666 DOI: 10.1126/science.1102896.

[2] Georgakilas, V.; Otyepka, M.; Bourlinos, A. B.; Chandra, V.; Kim, N.; Kemp, K. C.; Hobza, P.; Zboril, R.; Kim, K. S. Functionalization of Graphene: Covalent and Non-Covalent Approaches, Derivatives and Applications. *Chem. Rev.* **2012**, *112* (11), 6156–6214 DOI: 10.1021/cr3000412.

[3] Koshino, M. Stacking-Dependent Optical Absorption in Multilayer Graphene. *New J. Phys.* **2013**, *15* (1), 015010 DOI: 10.1088/1367-2630/15/1/015010.

[4] Lipson, H.; Stokes, A. R. A New Structure of Carbon. *Nature* **1942**, *149*, 328.

[5] Fitzer E.; Kochling K.-H.; Boehm H. P.; Marsh H. Recommended Terminology for the Description of Carbon as a Solid (IUPAC Recommendations 1995). *Pure Appl. Chem.* **2009**, *67* (3), 473 DOI: 10.1351/pac199567030473.

[6] Liu, Z.; Suenaga, K.; Harris, P. J. F.; Iijima, S. Open and Closed Edges of Graphene Layers. *Phys. Rev. Lett.* **2009**, *102* (1) DOI: 10.1103/PhysRevLett.102.015501.

[7] Lee, C.; Wei, X.; Kysar, J. W.; Hone, J. Measurement of the Elastic Properties and Intrinsic Strength of Monolayer Graphene. *Science* **2008**, *321* (5887), 385–388 DOI: 10.1126/science.1157996.

[8] Zhu, Y.; Murali, S.; Cai, W.; Li, X.; Suk, J. W.; Potts, J. R.; Ruoff, R. S. Graphene and Graphene Oxide: Synthesis, Properties, and Applications. *Adv. Mater.* **2010**, *22* (35), 3906–3924 DOI: 10.1002/adma.201001068.

[9] Pumera, M. Graphene-Based Nanomaterials and Their Electrochemistry. *Chem. Soc. Rev.* **2010**, *39* (11), 4146 DOI: 10.1039/c002690p.

[10] Avouris, P.; Dimitrakopoulos, C. Graphene: Synthesis and Applications. *Mater. Today* **2012**, *15* (3), 86–97.

[11] Zhang, D.-B.; Dumitrică, T. Effective-Tensional-Strain-Driven Bandgap Modulations in Helical Graphene Nanoribbons. *Small* **2011**, *7* (8), 1023–1027 DOI: 10.1002/smll.201001890.

[12] Kahlert, J. U.; Rawal, A.; Hook, J. M.; Rendina, L. M.; Choucair, M. Carborane Functionalization of the Aromatic Network in Chemically-Synthesized Graphene. *Chem. Commun.* **2014**, *50* (77), 11332 DOI: 10.1039/C4CC04521A.

[13] Loh, K. P.; Bao, Q.; Eda, G.; Chhowalla, M. Graphene Oxide as a Chemically Tunable Platform for Optical Applications. *Nat. Chem.* **2010**, *2* (12), 1015–1024 DOI: 10.1038/nchem.907.

[14] Szostak, R.; Morais, A.; Carminati, S. A.; Costa, S. V.; Marchezi, P. E.; Nogueira, A. F. Application of Graphene and Graphene Derivatives/Oxide Nanomaterials for Solar Cells. In *The Future of Semiconductor Oxides in Next-Generation Solar Cells*; Elsevier, 2018; pp 395–437.

[15] Jayasena, B.; Subbiah, S. A Novel Mechanical Cleavage Method for Synthesizing Few-Layer Graphenes. *Nanoscale Res. Lett.* **2011**, *6* (1), 95.

[16] Varrla, E.; Paton, K. R.; Backes, C.; Harvey, A.; Smith, R. J.; McCauley, J.; Coleman, J. N. Turbulence-Assisted Shear Exfoliation of Graphene Using Household Detergent and a Kitchen Blender. *Nanoscale* **2014**, *6* (20), 11810–11819 DOI: 10.1039/C4NR03560G.

[17] Shen, J.; He, Y.; Wu, J.; Gao, C.; Keyshar, K.; Zhang, X.; Yang, Y.; Ye, M.; Vajtai, R.; Lou, J.; Ajayan, P. M. Liquid Phase Exfoliation of Two-Dimensional Materials by Directly Probing and Matching Surface Tension Components. *Nano Lett.* **2015**, *15* (8), 5449–5454 DOI: 10.1021/acs.nanolett.5b01842.

[18] Ciesielski, A.; Samorì, P. Grapheneviasonication Assisted Liquid-Phase Exfoliation. *Chem Soc Rev* **2014**, *43* (1), 381–398 DOI: 10.1039/C3CS60217F.

[19] Haar, S.; Ciesielski, A.; Clough, J.; Yang, H.; Mazzaro, R.; Richard, F.; Conti, S.; Merstorf, N.; Cecchini, M.; Morandi, V.; Casiraghi, C.; Samorì, P. A Supramolecular Strategy to Leverage the Liquid-Phase Exfoliation of Graphene in the Presence of Surfactants: Unraveling the Role of the Length of Fatty Acids. *Small* **2015**, *11* (14), 1691–1702 DOI: 10.1002/smll.201402745.

[20] Zhao, J.; Pei, S.; Ren, W.; Gao, L.; Cheng, H.-M. Efficient Preparation of Large-Area Graphene Oxide Sheets for Transparent Conductive Films. *ACS Nano* **2010**, *4* (9), 5245–5252 DOI: 10.1021/nn1015506.

[21] Juang, Z.-Y.; Wu, C.-Y.; Lu, A.-Y.; Su, C.-Y.; Leou, K.-C.; Chen, F.-R.; Tsai, C.-H. Graphene Synthesis by Chemical Vapor Deposition and Transfer by a Roll-to-Roll Process. *Carbon* **2010**,

48 (11), 3169–3174 DOI: 10.1016/j.carbon.2010.05.001.

[22] Polsen, E. S.; McNerny, D. Q.; Viswanath, B.; Pattinson, S. W.; John Hart, A. High-Speed Roll-to-Roll Manufacturing of Graphene Using a Concentric Tube CVD Reactor. *Sci. Rep.* **2015**, *5* (1) DOI: 10.1038/srep10257.

[23] Kim, S.-M.; Jang, B.; Jo, K.; Kim, D.; Lee, J.; Kim, K.-S.; Lee, S.-M.; Lee, H.-J.; Han, S. M.; Kim, J.-H. Mechanics-Driven Patterning of CVD Graphene for Roll-Based Manufacturing Process. *2D Mater.* **2017**, *4* (2), 024003 DOI: 10.1088/2053-1583/aa59af.

[24] Van Bommel, A. J.; Crombeen, J. E.; Van Tooren, A. LEED and Auger Electron Observations of the SiC (0001) Surface. *Surf. Sci.* **1975**, *48* (2), 463–472.

[25] Wei, W.; Sun, K.; Hu, Y. H. Synthesis of 3D Cauliflower-Fungus-like Graphene from CO2 as a Highly Efficient Counter Electrode Material for Dye-Sensitized Solar Cells. *J. Mater. Chem. A* **2014**, *2* (40), 16842–16846 DOI: 10.1039/C4TA03909B.

[26] Wei, W.; Sun, K.; Hu, Y. H. Direct Conversion of CO_2 to 3D Graphene and Its Excellent Performance for Dye-Sensitized Solar Cells with 10% Efficiency. *J Mater Chem A* **2016**, *4* (31), 12054–12057 DOI: 10.1039/C6TA04008J.

[27] Müllen, K. Evolution of Graphene Molecules: Structural and Functional Complexity as Driving Forces behind Nanoscience. *ACS Nano* **2014**, *8* (7), 6531–6541 DOI: 10.1021/nn503283d.

[28] Dötz, F.; Brand, J. D.; Ito, S.; Gherghel, L.; Müllen, K. Synthesis of Large Polycyclic Aromatic Hydrocarbons: Variation of Size and Periphery. *J. Am. Chem. Soc.* **2000**, *122* (32), 7707–7717 DOI: 10.1021/ja000832x.

[29] Choucair, M.; Thordarson, P.; Stride, J. A. Gram-Scale Production of Graphene Based on Solvothermal Synthesis and Sonication. *Nat. Nanotechnol.* **2009**, *4* (1), 30–33 DOI: 10.1038/nnano.2008.365.

[30] Duan, J.; Chen, S.; Jaroniec, M.; Qiao, S. Z. Heteroatom-Doped Graphene-Based Materials for Energy-Relevant Electrocatalytic Processes. *ACS Catal.* **2015**, *5* (9), 5207–5234.

[31] Vo, T. H.; Shekhirev, M.; Kunkel, D. A.; Orange, F.; Guinel, M. J.-F.; Enders, A.; Sinitskii, A. Bottom-up Solution Synthesis of Narrow Nitrogen-Doped Graphene Nanoribbons. *Chem. Commun.* **2014**, *50* (32), 4172 DOI: 10.1039/c4cc00885e.

[32] Kawai, S.; Saito, S.; Osumi, S.; Yamaguchi, S.; Foster, A. S.; Spijker, P.; Meyer, E. Atomically Controlled Substitutional Boron-Doping of Graphene Nanoribbons. *Nat. Commun.* **2015**, *6*, 8098 DOI: 10.1038/ncomms9098.

[33] Guo, B.; Liu, Q.; Chen, E.; Zhu, H.; Fang, L.; Gong, J. R. Controllable N-Doping of Graphene. *Nano Lett.* **2010**, *10* (12), 4975–4980 DOI: 10.1021/nl103079j.

[34] Yang, Z.; Yao, Z.; Li, G.; Fang, G.; Nie, H.; Liu, Z.; Zhou, X.; Chen, X.; Huang, S. Sulfur-Doped Graphene as an Efficient Metal-Free Cathode Catalyst for Oxygen Reduction. *ACS Nano* **2012**, *6* (1), 205–211 DOI: 10.1021/nn203393d.

[35] Willke, P.; Amani, J. A.; Sinterhauf, A.; Thakur, S.; Kotzott, T.; Druga, T.; Weikert, S.; Maiti, K.; Hofsäss, H.; Wenderoth, M. Doping of Graphene by Low-Energy Ion Beam Implantation: Structural, Electronic, and Transport Properties. *Nano Lett.* **2015**, *15* (8), 5110–5115 DOI: 10.1021/acs.nanolett.5b01280.

[36] Brodie, B. C. On the Atomic Weight of Graphite. *Philos. Trans. R. Soc. Lond.* **1859**, *149*, 249–259.

[37] Eigler, S.; Dotzer, C.; Hirsch, A.; Enzelberger, M.; Müller, P. Formation and Decomposition of CO_2 Intercalated Graphene Oxide. *Chem. Mater.* **2012**, *24* (7), 1276–1282 DOI: 10.1021/cm203223z.

[38] Staudenmaier, L. Verfahren Zur Darstellung Der Graphitsäure. *Eur. J. Inorg. Chem.* **1898**, *31* (2), 1481–1487.

[39] Hummers Jr, W. S.; Offeman, R. E. Preparation of Graphitic Oxide. *J. Am. Chem. Soc.* **1958**, *80* (6), 1339–1339.

[40] Peng, L.; Xu, Z.; Liu, Z.; Wei, Y.; Sun, H.; Li, Z.; Zhao, X.; Gao, C. An Iron-Based Green Approach to 1-h Production of Single-Layer Graphene Oxide. *Nat. Commun.* **2015**, *6*, 5716 DOI: 10.1038/ncomms6716.

[41] Tang, L.; Li, X.; Ji, R.; Teng, K. S.; Tai, G.; Ye, J.; Wei, C.; Lau, S. P. Bottom-up Synthesis of Large-Scale Graphene Oxide Nanosheets. *J. Mater. Chem.* **2012**, *22* (12), 5676 DOI: 10.1039/c2jm15944a.

[42] Eda, G.; Chhowalla, M. Chemically Derived Graphene Oxide: Towards Large-Area Thin-Film Electronics and Optoelectronics. *Adv. Mater.* **2010**, *22* (22), 2392–2415 DOI:

10.1002/adma.200903689.
[43] Griggs, C. S.; Medina, V. F. Graphene and Graphene Oxide Membranes for Water Treatment. In *McGraw Hill Encyclopedia of Science & Technology, 11th Edition*; McGraw Hill.
[44] Yang, Q.; Su, Y.; Chi, C.; Cherian, C. T.; Huang, K.; Kravets, V. G.; Wang, F. C.; Zhang, J. C.; Pratt, A.; Grigorenko, A. N.; Guinea, F.; Geim, A. K.; Nair, R. R. Ultrathin Graphene-Based Membrane with Precise Molecular Sieving and Ultrafast Solvent Permeation. *Nat. Mater.* **2017**, *16* (12), 1198–1202 DOI: 10.1038/nmat5025.
[45] Thomas, H. R.; Day, S. P.; Woodruff, W. E.; Vallés, C.; Young, R. J.; Kinloch, I. A.; Morley, G. W.; Hanna, J. V.; Wilson, N. R.; Rourke, J. P. Deoxygenation of Graphene Oxide: Reduction or Cleaning? *Chem. Mater.* **2013**, *25* (18), 3580–3588 DOI: 10.1021/cm401922e.
[46] Naumov, A.; Grote, F.; Overgaard, M.; Roth, A.; Halbig, C. E.; Nørgaard, K.; Guldi, D. M.; Eigler, S. Graphene Oxide: A One- versus Two-Component Material. *J. Am. Chem. Soc.* **2016** DOI: 10.1021/jacs.6b05928.
[47] Nikolakopoulou, A.; Tasis, D.; Sygellou, L.; Dracopoulos, V.; Galiotis, C.; Lianos, P. Study of the Thermal Reduction of Graphene Oxide and of Its Application as Electrocatalyst in Quasi-Solid State Dye-Sensitized Solar Cells in Combination with PEDOT. *Electrochimica Acta* **2013**, *111*, 698–706 DOI: 10.1016/j.electacta.2013.08.064.
[48] Ghani, F.; Kristen, J.; Riegler, H. Solubility Properties of Unsubstituted Metal Phthalocyanines in Different Types of Solvents. *J. Chem. Eng. Data* **2012**, *57* (2), 439–449 DOI: 10.1021/je2010215.
[49] Liao, M.-S.; Scheiner, S. Electronic Structure and Bonding in Metal Phthalocyanines, Metal=Fe, Co, Ni, Cu, Zn, Mg. *J. Chem. Phys.* **2001**, *114* (22), 9780–9791 DOI: 10.1063/1.1367374.
[50] Petraki, F. Study of the Interfaces Formed between Thin Films of Phthalocyanines and Inorganic as Well as Organic Substrates by Photoelectron Spectroscopies, Department of Chemical Engineering, University of Patras: Patras.
[51] Nishihara, H.; Hirota, T.; Matsuura, K.; Ohwada, M.; Hoshino, N.; Akutagawa, T.; Higuchi, T.; Jinnai, H.; Koseki, Y.; Kasai, H.; Matsuo, Y.; Maruyama, J.; Hayasaka, Y.; Konaka, H.; Yamada, Y.; Yamaguchi, S.; Kamiya, K.; Kamimura, T.; Nobukuni, H.; Tani, F. Synthesis of Ordered Carbonaceous Frameworks from Organic Crystals. *Nat. Commun.* **2017**, *8* (1) DOI: 10.1038/s41467-017-00152-z.
[52] Jennings, C.; Aroca, R.; Hor, A.-M.; Loutfy, R. O. Raman Spectra of Solid Films 3—Mg, Cu and Zn Phthalocyanine Complexes. *J. Raman Spectrosc.* **1984**, *15* (1), 34–37.
[53] Bartholomew, C. R.; McConnell, A. A.; Smith, W. E. Resonance Raman Excitation Profile of Cobalt Phthalocyanine at Room Temperature and 10 K. *J. Raman Spectrosc.* **1989**, *20* (9), 595–600.
[54] Kroll, T.; Aristov, V. Y.; Molodtsova, O. V.; Ossipyan, Y. A.; Vyalikh, D. V.; Büchner, B.; Knupfer, M. Spin and Orbital Ground State of Co in Cobalt Phthalocyanine. *J. Phys. Chem. A* **2009**, *113* (31), 8917–8922 DOI: 10.1021/jp903001v.
[55] Arkan, F.; Izadyar, M. The Investigation of the Central Metal Effects on the Porphyrin-Based DSSCs Performance; Molecular Approach. *Mater. Chem. Phys.* **2017**, *196*, 142–152 DOI: 10.1016/j.matchemphys.2017.04.054.
[56] Usui, T.; Nakata, Y.; De Romeo Banoukepa, G.; Fujita, K.; Nishikawa, Y.; Shimizu, Y.; Fujii, A.; Ozaki, M. Glass-Sandwich-Type Organic Solar Cells Utilizing Liquid Crystalline Phthalocyanine. *Appl. Phys. Express* **2017**, *10* (2), 021602 DOI: 10.7567/APEX.10.021602.
[57] Son, H.-J.; Jin, S.; Patwardhan, S.; Wezenberg, S. J.; Jeong, N. C.; So, M.; Wilmer, C. E.; Sarjeant, A. A.; Schatz, G. C.; Snurr, R. Q.; Farha, O. K.; Wiederrecht, G. P.; Hupp, J. T. Light-Harvesting and Ultrafast Energy Migration in Porphyrin-Based Metal–Organic Frameworks. *J. Am. Chem. Soc.* **2013**, *135* (2), 862–869 DOI: 10.1021/ja310596a.
[58] Kumar, S. S.; Mathiyarasu, J.; Phani, K. L. N.; Yegnaraman, V. Simultaneous Determination of Dopamine and Ascorbic Acid on Poly (3,4-Ethylenedioxythiophene) Modified Glassy Carbon Electrode. *J. Solid State Electrochem.* **2006**, *10* (11), 905–913 DOI: 10.1007/s10008-005-0041-7.
[59] Bello, A.; Giannetto, M.; Mori, G.; Seeber, R.; Terzi, F.; Zanardi, C. Optimization of the DPV Potential Waveform for Determination of Ascorbic Acid on PEDOT-Modified Electrodes. *Sens. Actuators B Chem.* **2007**, *121* (2), 430–435 DOI: 10.1016/j.snb.2006.04.066.
[60] Dhar, S.; Majumder, T.; Chakraborty, P.; Mondal, S. P. DMSO Modified PEDOT:PSS Polymer/ZnO Nanorods Schottky Junction Ultraviolet Photodetector: Photoresponse, External Quantum Efficiency, Detectivity, and Responsivity Augmentation Using N Doped Graphene

Quantum Dots. *Org. Electron.* **2017** DOI: 10.1016/j.orgel.2017.11.024.
[61] Zhang, X.; MacDiarmid, A. G.; Manohar, S. K. Chemical Synthesis of PEDOT Nanofibers. *Chem. Commun.* **2005**, No. 42, 5328 DOI: 10.1039/b511290g.
[62] Paterakis, G.; Raptis, D.; Ploumistos, A.; Belekoukia, M.; Sygellou, L.; Ramasamy, M. S.; Lianos, P.; Tasis, D. N-Doped Graphene/PEDOT Composite Films as Counter Electrodes in DSSCs: Unveiling the Mechanism of Electrocatalytic Activity Enhancement. *Appl. Surf. Sci.* **2017**, *423*, 443–450 DOI: 10.1016/j.apsusc.2017.06.180.
[63] Tasis, D. Recent Progress on the Synthesis of Graphene-Based Nanostructures as Counter Electrodes in DSSCs Based on Iodine/Iodide Electrolytes. *Catalysts* **2017**, *7* (8), 234 DOI: 10.3390/catal7080234.
[64] Wei, W.; Chang, L.; Sun, K.; Pak, A. J.; Paek, E.; Hwang, G. S.; Hu, Y. H. The Bright Future for Electrode Materials of Energy Devices: Highly Conductive Porous Na-Embedded Carbon. *Nano Lett.* **2016**, *16* (12), 8029–8033 DOI: 10.1021/acs.nanolett.6b04742.
[65] Wen, Z.; Cui, S.; Pu, H.; Mao, S.; Yu, K.; Feng, X.; Chen, J. Metal Nitride/Graphene Nanohybrids: General Synthesis and Multifunctional Titanium Nitride/Graphene Electrocatalyst. *Adv. Mater.* **2011**, *23* (45), 5445–5450 DOI: 10.1002/adma.201102772.
[66] Yen, M.-Y.; Teng, C.-C.; Hsiao, M.-C.; Liu, P.-I.; Chuang, W.-P.; Ma, C.-C. M.; Hsieh, C.-K.; Tsai, M.-C.; Tsai, C.-H. Platinum Nanoparticles/Graphene Composite Catalyst as a Novel Composite Counter Electrode for High Performance Dye-Sensitized Solar Cells. *J. Mater. Chem.* **2011**, *21* (34), 12880 DOI: 10.1039/c1jm11850a.
[67] Yang, Z.; Liu, M.; Zhang, C.; Tjiu, W. W.; Liu, T.; Peng, H. Carbon Nanotubes Bridged with Graphene Nanoribbons and Their Use in High-Efficiency Dye-Sensitized Solar Cells. *Angew. Chem.* **2013**, *125* (14), 4088–4091 DOI: 10.1002/ange.201209736.
[68] Xu, X.; Huang, D.; Cao, K.; Wang, M.; Zakeeruddin, S. M.; Grätzel, M. Electrochemically Reduced Graphene Oxide Multilayer Films as Efficient Counter Electrode for Dye-Sensitized Solar Cells. *Sci. Rep.* **2013**, *3* (1) DOI: 10.1038/srep01489.
[69] Li, Z.; Gong, F.; Zhou, G.; Wang, Z.-S. NiS_2 /Reduced Graphene Oxide Nanocomposites for Efficient Dye-Sensitized Solar Cells. *J. Phys. Chem. C* **2013**, *117* (13), 6561–6566 DOI: 10.1021/jp401032c.
[70] Bi, E.; Chen, H.; Yang, X.; Peng, W.; Grätzel, M.; Han, L. A Quasi Core–shell Nitrogen-Doped Graphene/Cobalt Sulfide Conductive Catalyst for Highly Efficient Dye-Sensitized Solar Cells. *Energy Env. Sci* **2014**, *7* (8), 2637–2641 DOI: 10.1039/C4EE01339E.
[71] Ju, M. J.; Jeon, I.-Y.; Lim, K.; Kim, J. C.; Choi, H.-J.; Choi, I. T.; Eom, Y. K.; Kwon, Y. J.; Ko, J.; Lee, J.-J. Edge-Carboxylated Graphene Nanoplatelets as Oxygen-Rich Metal-Free Cathodes for Organic Dye-Sensitized Solar Cells. *Energy Environ. Sci.* **2014**, *7* (3), 1044–1052.
[72] Ahn, H.-J.; Kim, I.-H.; Yoon, J.-C.; Kim, S.-I.; Jang, J.-H. P-Doped Three-Dimensional Graphene Nano-Networks Superior to Platinum as a Counter Electrode for Dye-Sensitized Solar Cells. *Chem Commun* **2014**, *50* (19), 2412–2415 DOI: 10.1039/C3CC48920E.
[73] Huo, J.; Wu, J.; Zheng, M.; Tu, Y.; Lan, Z. High Performance Sponge-like Cobalt Sulfide/Reduced Graphene Oxide Hybrid Counter Electrode for Dye-Sensitized Solar Cells. *J. Power Sources* **2015**, *293*, 570–576 DOI: 10.1016/j.jpowsour.2015.05.117.
[74] Meng, X.; Yu, C.; Song, X.; Liu, Y.; Liang, S.; Liu, Z.; Hao, C.; Qiu, J. Nitrogen-Doped Graphene Nanoribbons with Surface Enriched Active Sites and Enhanced Performance for Dye-Sensitized Solar Cells. *Adv. Energy Mater.* **2015**, *5* (11), 1500180 DOI: 10.1002/aenm.201500180.
[75] Chen, P.-Y.; Li, C.-T.; Lee, C.-P.; Vittal, R.; Ho, K.-C. PEDOT-Decorated Nitrogen-Doped Graphene as the Transparent Composite Film for the Counter Electrode of a Dye-Sensitized Solar Cell. *Nano Energy* **2015**, *12*, 374–385 DOI: 10.1016/j.nanoen.2015.01.010.
[76] Balamurugan, J.; Thanh, T. D.; Kim, N. H.; Lee, J. H. Nitrogen-Doped Graphene Nanosheets with FeN Core-Shell Nanoparticles as High-Performance Counter Electrode Materials for Dye-Sensitized Solar Cells. *Adv. Mater. Interfaces* **2016**, *3* (1), 1500348 DOI: 10.1002/admi.201500348.
[77] Cui, X.; Xiao, J.; Wu, Y.; Du, P.; Si, R.; Yang, H.; Tian, H.; Li, J.; Zhang, W.-H.; Deng, D.; Bao, X. A Graphene Composite Material with Single Cobalt Active Sites: A Highly Efficient Counter Electrode for Dye-Sensitized Solar Cells. *Angew. Chem. Int. Ed.* **2016**, *55* (23), 6708–6712 DOI: 10.1002/anie.201602097.
[78] Huo, J.; Wu, J.; Zheng, M.; Tu, Y.; Lan, Z. A Transparent Cobalt Sulfide/Reduced Graphene

Oxide Nanostructure Counter Electrode for High Efficient Dye-Sensitized Solar Cells. *Electrochimica Acta* **2016**, *187*, 210–217 DOI: 10.1016/j.electacta.2015.11.071.

[79] Yu, C.; Fang, H.; Liu, Z.; Hu, H.; Meng, X.; Qiu, J. Chemically Grafting Graphene Oxide to B,N Co-Doped Graphene via Ionic Liquid and Their Superior Performance for Triiodide Reduction. *Nano Energy* **2016**, *25*, 184–192 DOI: 10.1016/j.nanoen.2016.04.039.

[80] Dong, J.; Wu, J.; Jia, J.; Fan, L.; Lan, Z.; Lin, J.; Wei, Y. Cobalt Selenite Dihydrate as an Effective and Stable Pt-Free Counter Electrode in Dye-Sensitized Solar Cells. *J. Power Sources* **2016**, *336*, 83–90 DOI: 10.1016/j.jpowsour.2016.10.056.

[81] Dao, V.-D.; Jin, I.-K.; Choi, H.-S. Design of PtRu Alloy/Reduced Graphene Oxide Nanohybrid Counter Electrodes for Highly Efficient Dye-Sensitized Solar Cells. *Electrochimica Acta* **2016**, *201*, 1–7 DOI: 10.1016/j.electacta.2016.03.192.

[82] Meng, X.; Yu, C.; Lu, B.; Yang, J.; Qiu, J. Dual Integration System Endowing Two-Dimensional Titanium Disulfide with Enhanced Triiodide Reduction Performance in Dye-Sensitized Solar Cells. *Nano Energy* **2016**, *22*, 59–69 DOI: 10.1016/j.nanoen.2016.02.010.

[83] Belekoukia, M.; Ramasamy, M. S.; Yang, S.; Feng, X.; Paterakis, G.; Dracopoulos, V.; Galiotis, C.; Lianos, P. Electrochemically Exfoliated Graphene/PEDOT Composite Films as Efficient Pt-Free Counter Electrode for Dye-Sensitized Solar Cells. *Electrochimica Acta* **2016**, *194*, 110–115 DOI: 10.1016/j.electacta.2016.02.073.

[84] Lee, M. W.; Kim, H.-Y.; Yoon, H.; Kim, J.; Suh, J. S. Fabrication of Dispersible Graphene Flakes Using Thermal Plasma Jet and Their Thin Films for Solar Cells. *Carbon* **2016**, *106*, 48–55 DOI: 10.1016/j.carbon.2016.05.018.

[85] Yu, Y.-H.; Chi, W.-F.; Huang, W.-C.; Wang, W.-S.; Shih, C.-J.; Tsai, C.-H. High-Efficiency Counter Electrodes Using Graphene Hybrid with a Macrocyclic Nickel Complex for Dye-Sensitized Solar Cells. *Org. Electron.* **2016**, *31*, 207–216 DOI: 10.1016/j.orgel.2016.01.038.

[86] Yu, C.; Liu, Z.; Meng, X.; Lu, B.; Cui, D.; Qiu, J. Nitrogen and Phosphorus Dual-Doped Graphene as a Metal-Free High-Efficiency Electrocatalyst for Triiodide Reduction. *Nanoscale* **2016**, *8* (40), 17458–17464 DOI: 10.1039/C6NR00839A.

[87] Dao, V.-D.; Larina, L. L.; Tran, Q. C.; Bui, V.-T.; Nguyen, V.-T.; Pham, T.-D.; Mohamed, I. M. A.; Barakat, N. A. M.; Huy, B. T.; Choi, H.-S. Evaluation of Pt-Based Alloy/Graphene Nanohybrid Electrocatalysts for Triiodide Reduction in Photovoltaics. *Carbon* **2017**, *116*, 294–302 DOI: 10.1016/j.carbon.2017.02.004.

[88] Yang, W.; Xu, X.; Hou, L.; Ma, X.; Yang, F.; Wang, Y.; Li, Y. Insight into the Topological Defects and Dopants in Metal-Free Holey Graphene for Triiodide Reduction in Dye-Sensitized Solar Cells. *J. Mater. Chem. A* **2017**, *5* (12), 5952–5960 DOI: 10.1039/C7TA00278E.

[89] Yu, Z.; Bai, Y.; Wang, Y.; Liu, Y.; Zhao, Y.; Liu, Y.; Sun, K. One-Step Synthesis of Three-Dimensional Nitrogen and Sulfur Co-Doped Graphene Networks as Low Cost Metal-Free Counter Electrodes for Dye-Sensitized Solar Cells. *Chem. Eng. J.* **2017**, *311*, 302–309 DOI: 10.1016/j.cej.2016.11.093.

[90] Meng, X.; Yu, C.; Song, X.; Liu, Z.; Lu, B.; Hao, C.; Qiu, J. Rational Design and Fabrication of Sulfur-Doped Porous Graphene with Enhanced Performance as a Counter Electrode in Dye-Sensitized Solar Cells. *J. Mater. Chem. A* **2017**, *5* (5), 2280–2287 DOI: 10.1039/C6TA09505D.

3. Characterization Techniques

In this section we will present a number of techniques that have been employed and in particular, what sort of clues they can give about the nature of our materials. Details about the instrumentation will also be provided here. As we were interested in knowing if our materials could satisfactorily replace Pt in DSSCs, this was always our first measurement; if the devices underpeformed, there was no need to examine anything else.

X-ray powder diffraction

The diffraction patterns of graphite and graphite oxides have been studied extensively[1–3] with X-rays as well as neutron scattering. The different stacking arrangements of graphene sheets in graphite were discovered using X-ray photographs, almost 80 years ago[4].

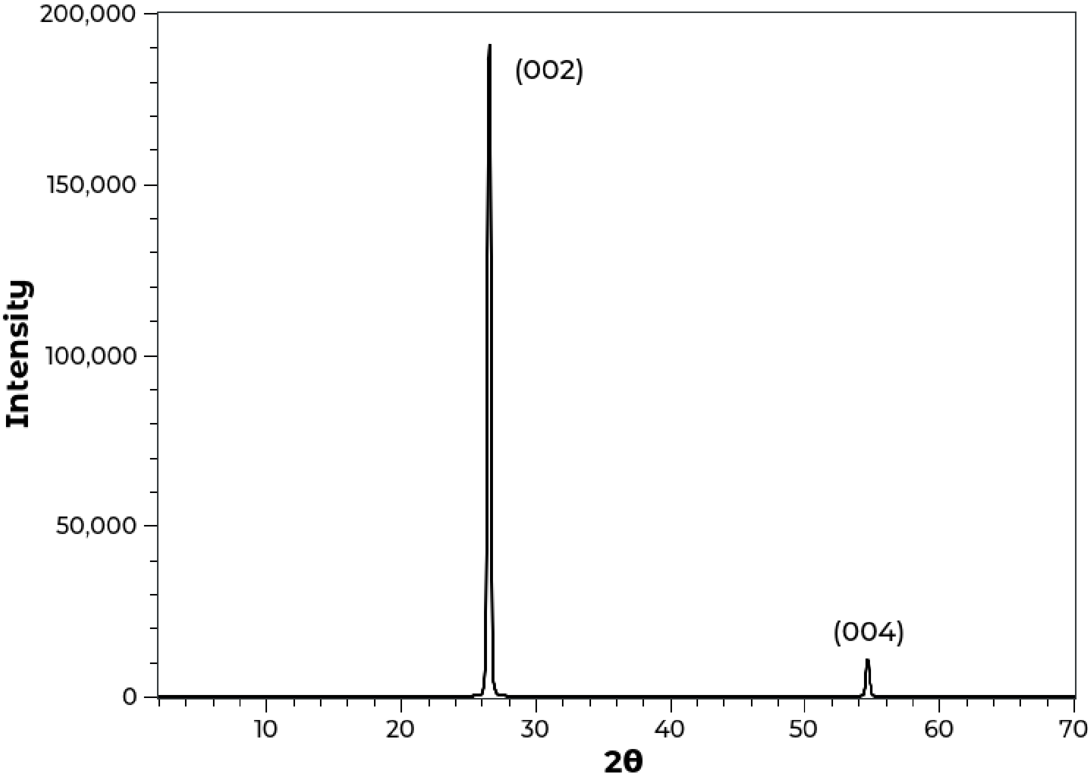

Figure 3.1: XRD diffraction pattern of graphite powder. Diffractions from crystallographic planes other than (002) and (004) are too weak to be discernible at this scale.

We have used graphite powder as the starting material for our composites. The graphite was oxidized and submitted to ultrasonication, so the size of the crystallites was further reduced down to several μm. For these reasons, Powder X-Ray Diffraction was the most appropriate crystallographic technique for the study of our samples.

Bragg's Law correlates the distance between two crystallographic planes with the angle of diffraction, stating that $\mathbf{n \cdot \lambda = 2 \cdot d \cdot \sin\theta}$, where n is a positive integer, λ is the wavelength of incident wave, d is the interplanar distance and θ is the scattering angle. Given the “statistical” nature of the technique, as graphite is exfoliated down to few-layer graphene, we expect the intensity of the peaks to decrease, as there are fewer planes (the **n** in Bragg's Law) contributing to the constructive interference. We have already seen that as graphite is oxidized, the distance between adjacent sheets increases; solving Bragg's Law for θ, this increase of d entails the shifting of signals to lower angles. Furthermore, oxidation of the graphene sheets causes them to deform and become misaligned in the crystallites. As a result, while the principal signal will be at a certain angle, the peaks will not be as sharp and well-defined as in graphite; rather, there will be a distribution of signals around the main angle of diffractions.

All that becomes immediately apparent, when the following diffractogram (Figure 3.2) is contrasted with that of graphite (Figure 3.1):

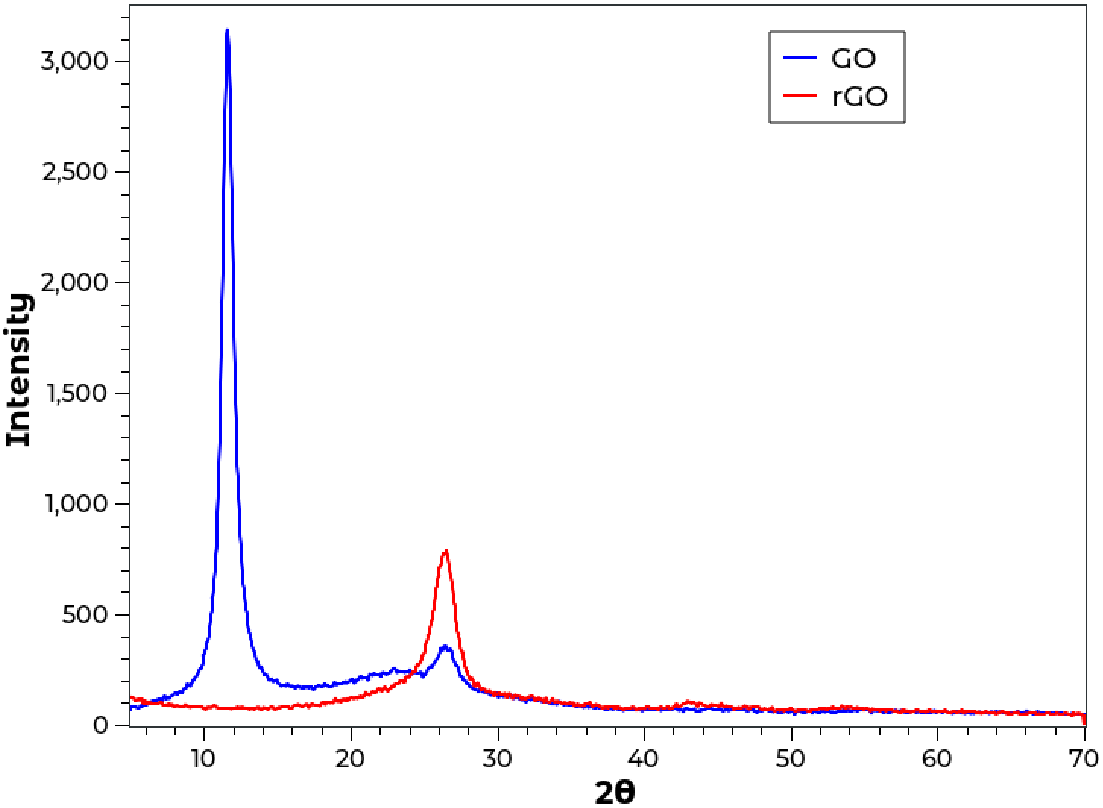

Figure 3.2: Diffraction patterns of GO (in blue) and rGO, annealed at 700°C (red).

First of all, the intensity of the signal has dropped by several orders of magnitude. The oxide has a relatively broad peak, with its center shifted by ~15° compared to that of graphite. The small peak at 26.5° is a sign that there is still a quantity of material that has not been oxidized. There is a curve between the two peaks, from which we can tell that another quantity of material is in an intermediate, disordered state. After the consecutive treatments, there are even less graphene sheets stacked together, which is evident from the intensity of rGO's signal, relative to that of GO. The peak of rGO is also broad, spread over several degrees, hinting at defects and orientation issues in the lattice.

X-ray diffraction was also useful in “fingerprinting” our materials. Since there were no reference materials we could compare our samples to, especially when we needed to replicate a synthesis, PXRD was the quickest way to confirm that we had obtained a structurally similar material.

Obviously, when we had a dopant that formed crystals and it managed to retain its crystallinity throughout the treatments (and as long as it was not in trace amounts), we could confirm its presence, as well as its structure by looking at the diffractogram of the composite. The nature of the technique allows one to add or subtract patterns of known substances, making easier the identification of substances that coexist in the same sample.

All of our XRD measurements were taken using the diffractometer at the Department of Physics at the University of Ioannina. It is an AXS D8 Advance X-Ray diffractometer, made by Bruker, with a Cu Kα radiation source (λ=1.54178Å), equipped with a secondary graphite monochromator. Unless otherwise noted, all our samples were scanned at a speed of 0.2°/s in the range 2°-70°.

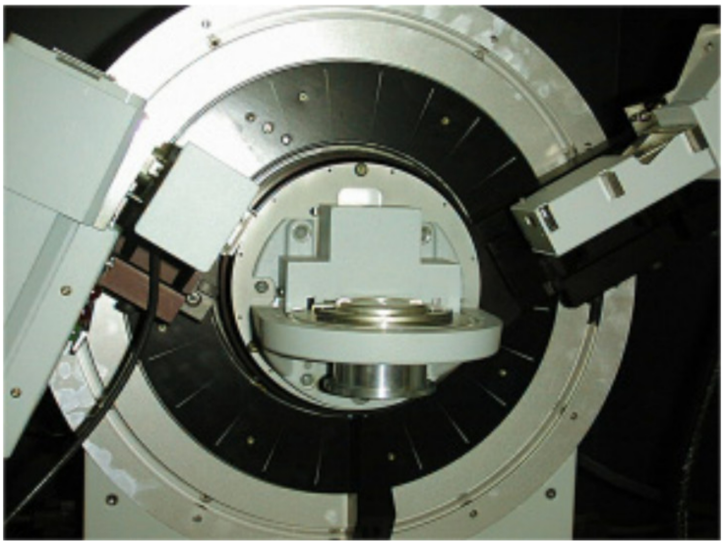

Image 3.1: A close-up of the Bruker D8. The Cu source, the sample holder and the detector are all visible in this picture.

Raman spectroscopy

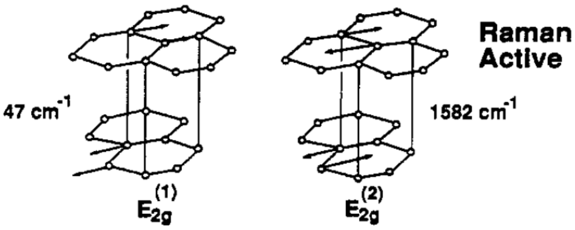

Figure 3.3: The two primary Raman-active vibrational modes of graphite.[5]

Carbon materials like graphite and diamond were among the first substances to be studied after lasers had been incorporated in Raman spectroscopy. Their ordered nature (which had been established decades ago via XRD) meant that it was easy to study their Raman-active vibrational modes and assign Stokes and anti-Stokes scattering frequencies to them (Figure 3.3). As lasers, optics and signal processing progressed in the following years, researchers were able to identify a dopant or the extent of oxidation[5] in graphite by the corresponding Raman shift, or by the ratio of the Stokes and the anti-Stokes intensities.

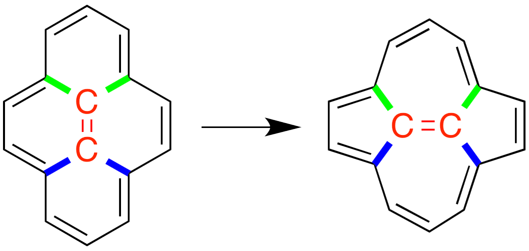

Figure 3.4: Formation of a Stone-Wales defect.

Graphene and its derivatives have been probed and studied exhaustively with Raman spectroscopy. A trained scientist can accurately estimate the number of stacked graphene sheets, just by looking at their Raman spectrum. It is possible to identify signals from specific imperfections in the lattice, such as 5-7-7-5 Stone-Wales defects (Figure 3.4), or 5-8-5 rings[6]. When graphene has been modified via the GO route, it is of particular interest to see the extent of restoration of the π system. For this assessment, the best criterion is the ratio of intensities between the vibrations of sp^3 carbon bonds, usually referred to as the D peak or frequency, to that of sp^2 carbon bonds, the E_{2g} or more commonly, the G frequency. The simplicity of the technique, enables the monitoring of the GO reduction process, which is no more involved than monitoring a reaction with common spectroscopy. The constant improvement of the components used therein has permitted Raman operators to discern negligible harmonic vibrations and distinguish between signals from the basal plane and the edges of graphene sheets[6].

We did not have such high aspirations for our measurements. As we were interested in the electrochemical application of our materials, it was important to "see" the extent of the π system in our composites and the reduction of the lattice induced by our treatments. For that, we mainly needed the intensity ratio of the D and G bands (I_D/I_G) that was mentioned earlier.

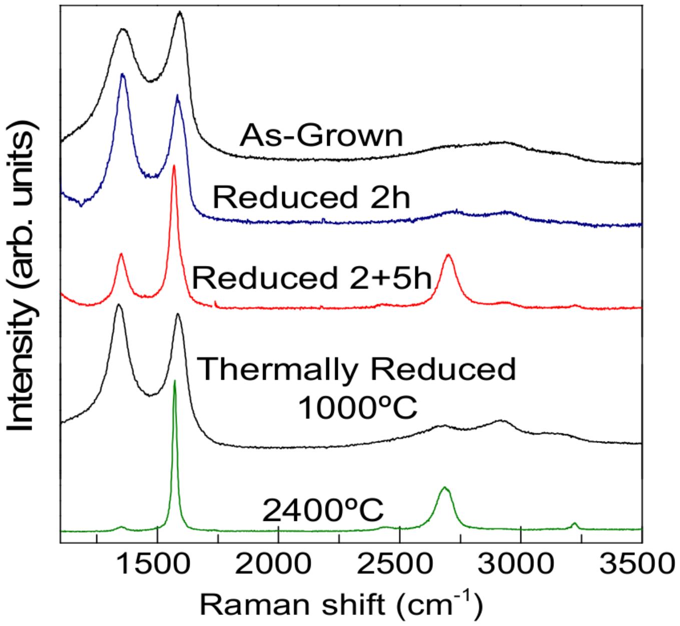

Figure 3.5: Raman spectra of GO (top black), chemically (blue & red) and thermally (bottom black & green) reduced rGO. The spectrum of the sample annealed at 2400°C is almost indistinguishable to that of pristine graphene.[6]

All Raman measurements were taken at ICE-HT in Patras, with a Renishaw InVia Raman 2000 spectrometer equipped with a 2400 grooves/mm grating providing 2cm^{-1} resolution. The λ=514.5 nm beam of a solid state laser, which was used for excitation, was focused on the sample by means of a 100x objective lens, with a numerical aperture of 0.85.

Thermal analysis

As we fabricated our materials using heat treatment, at times we needed to peer into the processes that took place as the samples were annealed and in particular when we used volatile dopants, such as phthalocyanines. For the same class of composites, it was also important to assess their thermal stability and – by extension – their optimal operating conditions. Such insights were afforded through

Image 3.2: Equipment at the Thermal Analysis Unit at the University of Ioannina. Far right: The STA 449C Jupiter thermo-microbalance.

the thermal analysis of our samples, using thermogravimetric analysis (TGA) and its “sister” techniques, DTA and DSC.

Thermal analyses were conducted at the Thermal Analysis Unit, at the Department of Chemistry, using a Netzsch STA 449C Jupiter thermo-microbalance, capable of carrying out TGA, DTA and DSC analyses simultaneously.

X-ray photoelectron spectroscopy

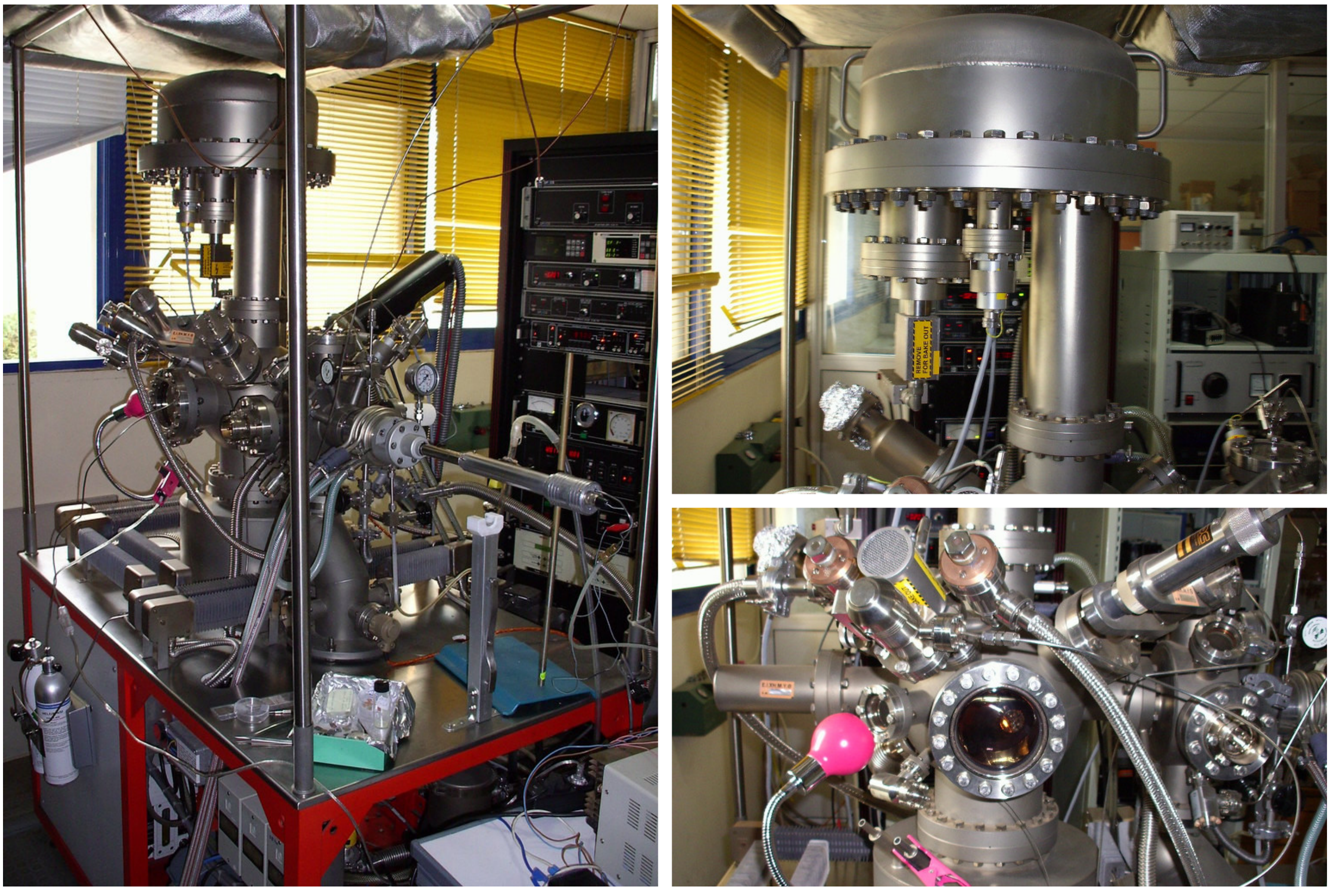

Image 3.3: Left: the XP spectrometer at the Institute of Chemical Engineering Sciences (Patras). The X-ray source is inside the black tube towards the back. Top right: view of the detector. Bottom right: sample chamber.

XPS is a very sensitive surface analysis (10-15nm) technique, able to detect elements heavier than H or He with high precision and also able to distinguish between different electronic configurations of the same element, e.g. sp^2 and sp^3 carbon atoms. It can also perform a quantitative analysis, albeit within a lesser degree of accuracy (at best with a margin of error between 5-10%, depending on the instrument and the analytical software).

The spectrometer at the Institute of Chemical Engineering Sciences (Patras) is also equipped with a source of high-energy UV radiation, which can knock off electrons from the outer shells (HOMO) of the molecules. Knowing the energy level of the HOMO electrons helps in estimating the work function of the material with increased accuracy.

Our samples were prepared by depositing the synthesized materials as thin films via spin-coating on TCO-coated glasses. XP spectroscopy was very well suited for their study, as the measured samples were not processed in a different manner than those that went in the actual devices. XPS not only confirmed that doping of graphene was successful, it gave us ample clues as to how the dopants were incorporated into the graphitic lattice.

XPS and UPS measurements were carried out in an ultra high vacuum system (UHV) with base pressure in both chambers at 1×10^{-9}mbar. Unmonochromatized AlKα line at 1486.6eV and an analyzer pass energy of 36eV, giving a full width at half maximum (FWHM) of 0.9eV for the Au $4f_{7/2}$ peak, were used in all XPS measurements. Errors in our quantitative data are found in the range of ~10%, (peak areas) while the accuracy for BEs assignments is ~0.1eV. The UPS spectra were obtained using HeI irradiation with hν = 21.23eV produced by a UV source (model UVS 10/35). The energy of the Highest Occupied Molecular Orbital (HOMO) was calculated from the sum of the measured energy values of the work function (WF) and the HOMO cut off at the low binding energy (BE) side of the spectra. The work function was determined by subtracting the width of the UPS spectra from the HeI excitation energy. For these measurements a bias of -12.3V was applied to the sample in order to avoid interference of the spectrometer threshold in the UPS spectra. For the measurements, the samples were deposited (by spin coating) on oxygen plasma cleaned ITO coated glass substrate in order to eliminate carbon contaminants of the surface and increase the surface's wettability.

Transmission electron microscopy

Through TEM we are able to observe the most minute details of our samples, almost down to the atomic scale. Contrast in transmission electron micrographs is dependent upon matter density. The thicker or denser the observed region, the more beam electrons it deflects and the darker it appears. This working principle of TEM not only allows us to actually see graphene sheets, but it also enables us to count how many of them are stacked together. Sample regions with densely packed adducts or dopants can be clearly visible as well.


Image 3.4: The transmission electron microscope at the Department of Biology, University of Patras.

Transmission electron microscopy observations were made on a JEOL JEM-2100 microscope using dispersions of doped rGO in isopropanol/water 2:1, which were cast on carbon grids.

Scanning electron microscopy

Though not as powerful as TEM, SEM has its own merits. A scanning electron microscope usually has two modes of operation: In the first mode, it collects the secondary electrons that are ejected from the k-shell of the specimen atoms by inelastic scattering interactions with beam electrons. These electrons reveal the surface topography of the sample. Protrusions, elevated regions and edges appear brighter, as there are more atoms exposed to the beam, while troughs, holes and other conformations with smaller exposed areas appear darker. Secondary electrons are emitted from depths up to 50nm from the surface. In its second mode of operation, the microscope collects the backscattered electrons of the beam, which interact elastically and are scattered by specimen atoms. Heavier atoms (high atomic number) backscatter electrons more strongly than lighter ones and thus appear brighter. This mode of operation gives us a visual depiction of a sample's chemical composition and its variance along the sample surface. Backscattered electrons are of higher energy, and they may originate from atoms up to 300nm from the surface.

The morphology of the samples deposited as thin films was studied using a Zeiss SUPRA 35VP Field-Emission Scanning Electron Microscope (FESEM), equipped with an EDS analyzer. Our samples did not require a metal coating, as they were conducting themselves.

Atomic force microscopy

Atomic force microscopes operate by “caressing” a sample with the tip of a cantilever. As it scans the surface of a sample in the xy plane, the vertical movement or deflection (z axis) of the cantilever is measured through piezoelectric and/or optical components within fractions of a nanometer. The recorded signals are translated into a digital, false color image, with each x,y coordinate corresponding to a single pixel and the deflection along the z axis mapped to a specific color. AFM data complement those acquired with TEM and SEM and provide us with extremely detailed measurements of the sample topography, revealing the exact dimensions of morphological elements observed with the other microscopy techniques.

AFM images were produced by a Bruker Dimension Icon atomic force microscope.

Solar cell performance assessment

This was the first and most important test for our materials. Electrodes that did not perform at least as well as reference Pt electrodes were discarded and no further analysis was conducted on them.

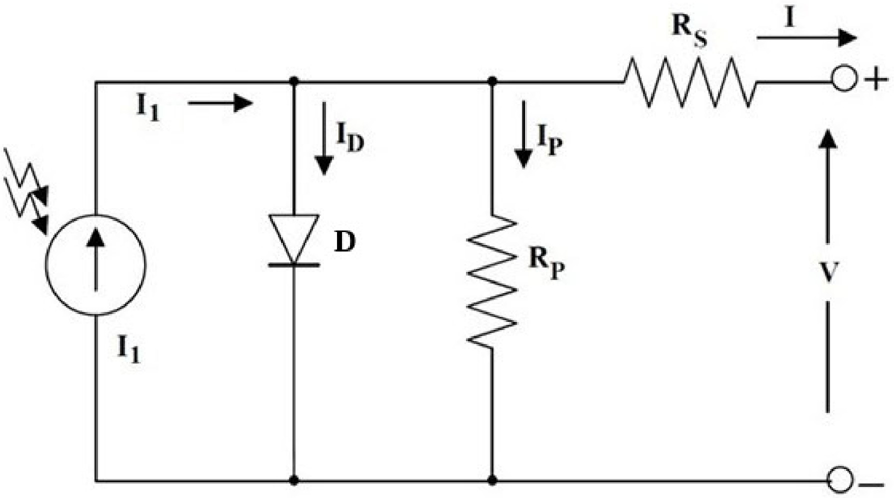

Figure 3.6: Ideal schematic representation of a solar cell.

The methodology used in assessing the performance of the devices is the same as that for conventional solar panels. An ideal solar cell (Figure 3.6) is represented as a current source in antiparallel with a diode (D) and in parallel with a resistance (R_P). These three components correspond to the internals of a solar cell. The diode exists because current can only flow in one direction and can not be reversed. The internal resistance – also called shunt resistance – should be infinitely big, so that no current flows through it. The shunt resistance represents losses and dark currents inside the cell itself. The whole system is connected in series with another resistance (R_S), which represents the outer components (connectors, cabling, etc.) of the cell. When the cell is illuminated, a current (I_1) is generated, which varies linearly with solar radiation and some part of it is wasted on R_P and R_S. I is the useful current exiting the device and V is the measured voltage across the terminals of the device.

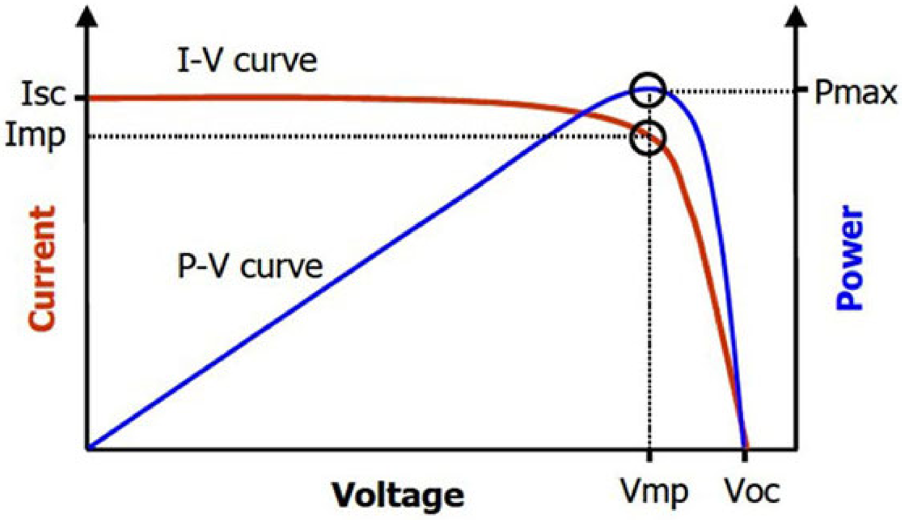

Figure 3.7: I-V and P-V curves of a solar cell.

The electric power (**P**) of a device is equal to the work done per unit of time, so **(V·Q)/t**, where V is the electric potential, measured in Volts, which is applied on a charge Q, measured in Coulombs, per time, t, measured in seconds. Since charge per time is equal to current, I, measured in Amperes, we end up with the well-known **P = IV**. This means that the power output of an ideal cell is the product of its maximum current output, i.e. the current we would obtain by short-circuiting the device, or short-circuit current, I_{SC}, times its maximum voltage, i.e. the voltage theoretically measured at the terminals when the circuit is open, V_{OC}. Solar cells deviate from that ideal circuit and their current and voltage vary non-linearly, so we use I-V plots (Figure 3.7) to calculate their actual power output under set conditions of irradiance and temperature.

By using what is in essence a very sophisticated rheostat, we vary the resistance between the terminals from infinite, which gives us the open circuit voltage, V_{OC} to almost zero, to measure the short-circuit current, I_{SC}, recording every value pair in between. The ratio of the area defined by the I-V plot to the area of the rectangle with dimensions $I_{SC} \cdot V_{OC}$ is termed the fill factor of a given device. The higher the fill factor, the closer the device's behavior to the ideal. For a particular device under given conditions, the stationary point of the I-V curve corresponds to the current and voltage combination that yields the maximum output power (maximum power point, mp). This can be located by plotting a P-V curve for the device under those conditions (see the P-V curve of Figure 3.7). In actual solar power installations, this has to be taken into account in order to maximize energy production, so inverters and other “smart” devices connected to solar panels vary their load according to insolation and temperature.

I-V curves were recorded with a Keithley 2601 source meter at ambient temperature. A Solar Light XPS-300 solar simulator set at $100mW/cm^2$ was used for illumination of the samples.

Cyclic voltammetry

Cyclic voltammetry might seem superfluous when the performance of actual devices has been measured. However, by subjecting our system to cyclic voltammetry measurements, we can reaffirm its electrocatalytic activity and better compare it to the reference. A higher reduction peak current density and a lower peak-to-peak voltage separation (the horizontal distance between a reduction and the corresponding oxidation peaks in a typical voltammogram) indicate a higher catalytic activity[7].

We can also verify that there are no secondary electrochemical reactions taking place inside the cell. The peaks in the reduction and the oxidation curves should correspond to the electron transfers between the redox pair. Since the overall reduction and oxidation processes involve two electron transfers ($I_3^- + 2e^- \rightleftharpoons 3I^-$ & $3I_2 + 2e^- \rightleftharpoons 2I_3^-$), we expect two peaks in each curve.

Electrochemical behavior of the samples was studied by cyclic voltammetry measurements using three-electrode cells in which Ag/AgCl and platinum sheet were used as reference and counter electrodes, respectively. The electrolyte was 0.1M $LiClO_4$, 0.001M I_2 and 0.01M LI in acetonitrile solution.

Electrochemical impedance spectroscopy

As it has already been discussed, the behavior of solar cells is not ideal. The performance of DSSCs in particular may be impacted by charge transport, transfer, and accumulation processes in the cell. These include (i) charge transport due to electron diffusion through TiO_2 and ionic diffusion in the electrolyte solution; (ii) charge transfer due to electron back reaction at the FTO/electrolyte interface and recombination at the TiO_2/electrolyte interface and the regeneration of the redox species at counter-electrode/electrolyte interfaces; and (iii) charging of the capacitive elements in the cells including the interfaces, the conduction band, and surface states of the porous network of TiO_2[8].

The EIS technique involves applying an alternating voltage to the system under study and analyzing the resulting alternating current. During the EIS measurements, the small signal sinusoidal voltage $V(\omega,t)=V_0\sin(\omega t)$ with amplitude V_0 and variable frequency f ($f=\omega/2\pi$, where ω is the angular frequency) is applied to the system, and the response current $I(\omega,t)$ is measured at the same frequencies. The impedance $Z(\omega,t)$ related to the system can be calculated through Ohm's law as:

$$Z(\omega,t)=\frac{V(\omega,t)}{I(\omega,t)}$$

For a given ω, the current response could be in-phase or out-of-phase with respect to the voltage stimulus, so that its general expression is given by $I(\omega,t)=I_0\sin(\omega t-\theta)$, where I_0 is the current signal amplitude and θ is the phase angle between voltage and current.

By exploiting the complex number notation and applying Euler's relationship, we get:

$Z(\omega,t) = Z(\omega)(\cos\theta + j\sin\theta) = Z'(\omega)+ jZ''(\omega)$

where $Z'=|Z|\cos\theta$ and $Z''= |Z|\sin\theta$ are the real and the imaginary part of the impedance, respectively. From that last equation, the modulus and the phase of the impedance can be obtained from:

$$|Z(\omega)|=\sqrt{Z'^2(\omega)+Z''^2(\omega)}$$

and

$$\theta(\omega)=\tan^{-1}\left\{\frac{Z''(\omega)}{Z'(\omega)}\right\}$$

The data obtained via EIS are usually represented in two different ways. The first one reports Z” as a function of Z' in the complex plane and it is referred to as the Nyquist plot. The second representation, referred to as the Bode plot, reports (usually) log|Z| and θ as a function of logf (less used representations report Z’ and Z” as a function of logf).[9]

Through some complex calculations and software analysis, an equivalent circuit is deduced. The type of components in that circuit (resistors, capacitors, coils, etc.) and how these are connected to each other might hint at the nature of the phenomena that affect the processes listed earlier. It is up to the researcher to interpret that data, but it is not always feasible to extrapolate from there. On the bright side, EIS does at least measure the impedance and it is always possible to compare a sample to a reference material.

Electrochemical impedance spectroscopy was carried out on symmetric dummy cells using the synthesized materials or Pt as electrocatalyst and the same electrolyte as the one filling the solar cell devices. All electrochemical measurements were made by employing an Autolab PGSTAT 128N potentiostat.

Chapter Bibliography

[1] Jeong, H.-K.; Lee, Y. P.; Lahaye, R. J. W. E.; Park, M.-H.; An, K. H.; Kim, I. J.; Yang, C.-W.; Park, C. Y.; Ruoff, R. S.; Lee, Y. H. Evidence of Graphitic AB Stacking Order of Graphite Oxides. *J. Am. Chem. Soc.* **2008**, *130* (4), 1362–1366 DOI: 10.1021/ja076473o.

[2] Zhou, Z.; Bouwman, W. G.; Schut, H.; Pappas, C. Interpretation of X-Ray Diffraction Patterns of (Nuclear) Graphite. *Carbon* **2014**, *69*, 17–24 DOI: 10.1016/j.carbon.2013.11.032.

[3] Li, Z. Q.; Lu, C. J.; Xia, Z. P.; Zhou, Y.; Luo, Z. X-Ray Diffraction Patterns of Graphite and Turbostratic Carbon. *Carbon* **2007**, *45* (8), 1686–1695 DOI: 10.1016/j.carbon.2007.03.038.

[4] LIPSON, H.; STOKES, A. R. A New Structure of Carbon. *Nature* **1942**, *149*, 328.

[5] Wang, Y.; Alsmeyer, D. C.; McCreery, R. L. Raman Spectroscopy of Carbon Materials: Structural Basis of Observed Spectra. *Chem. Mater.* **1990**, *2* (5), 557–563.

[6] Díez-Betriu, X.; Álvarez-García, S.; Botas, C.; Álvarez, P.; Sánchez-Marcos, J.; Prieto, C.; Menéndez, R.; de Andrés, A. Raman Spectroscopy for the Study of Reduction Mechanisms and Optimization of Conductivity in Graphene Oxide Thin Films. *J. Mater. Chem. C* **2013**, *1* (41), 6905 DOI: 10.1039/c3tc31124d.

[7] Yang, Z.; Liu, M.; Zhang, C.; Tjiu, W. W.; Liu, T.; Peng, H. Carbon Nanotubes Bridged with Graphene Nanoribbons and Their Use in High-Efficiency Dye-Sensitized Solar Cells. *Angew. Chem.* **2013**, *125* (14), 4088–4091 DOI: 10.1002/ange.201209736.

[8] Sarker, S.; Ahammad, A. J. S.; Seo, H. W.; Kim, D. M. Electrochemical Impedance Spectra of Dye-Sensitized Solar Cells: Fundamentals and Spreadsheet Calculation. *Int. J. Photoenergy* **2014**, *2014*, 1–17 DOI: 10.1155/2014/851705.

[9] Sacco, A. Electrochemical Impedance Spectroscopy: Fundamentals and Application in Dye-Sensitized Solar Cells. *Renew. Sustain. Energy Rev.* **2017**, *79*, 814–829 DOI: 10.1016/j.rser.2017.05.159.

4. Experimental Section

Syntheses

Graphite with an average particle size of 500µm and a purity of >95% was supplied from NGS Naturgraphit GmbH (batch: large flakes). Deionized water was produced via filtration through an ion-exchange resin. All reagents and solvents were used as purchased.

Graphene oxide

For our experiments, we used three different batches of GO, two of them prepared according to the protocol described by Kovtyukhova et al.[1] and the other following a process proposed by Zhao et al.[2]. Both of them are variations of the Hummers & Offeman method, with the former adding a pre-oxidation step to the process, while the latter relies on milder oxidation conditions and separation of the particulates based on their size via centrifugation. The detailed steps of each procedure are taken directly from each publication and listed below.

Kovtyukhova et al.

"The graphite powder (20g) was put into an 80°C solution of concentrated H_2SO_4 *(30mL),* $K_2S_2O_8$ *(10g), and* P_2O_5 *(10g). The resultant dark blue mixture was thermally isolated and allowed to cool to room temperature over a period of 6h. The mixture was then carefully diluted with distilled water, filtered, and washed on the filter until the rinse water pH became neutral. The product was dried in air at ambient temperature overnight. This preoxidized graphite was then subjected to oxidation by Hummers' method. The oxidized graphite powder (20g) was put into cold (0°C) concentrated* H_2SO_4 *(460mL).* $KMnO_4$ *(60g) was added gradually with stirring and cooling, so that the temperature of the mixture was not allowed to reach 20°C. The mixture was then stirred at 35°C for 2h, and distilled water (920mL) was added. In 15min, the reaction was terminated by the addition of a large amount of distilled water (2.8L) and 30%* H_2O_2 *solution (50mL), after which the color of the mixture changed to bright yellow. The mixture was filtered and washed with 1:10 HCl solution (5L) in order to remove metal ions. The GO product was suspended in distilled water to give a viscous, brown, 2% dispersion, which was subjected to dialysis to completely remove metal ions and acids. The resulting 0.5% w/v GO dispersion, which is stable for a period of years, was used to prepare exfoliated GO.*

Exfoliation was achieved by dilution of the 0.5% GO dispersion (1mL) with deionized water (24mL), followed by 15min sonication. The resulting homogeneous yellow-brown sol, which contained 0.2g/L GO, was stable for a period of months and was used for film preparation."

Other than scaling down the quantities of the reagents by an order of magnitude and extending the ultrasonication period to 2h, the process was followed as laid out by the authors.

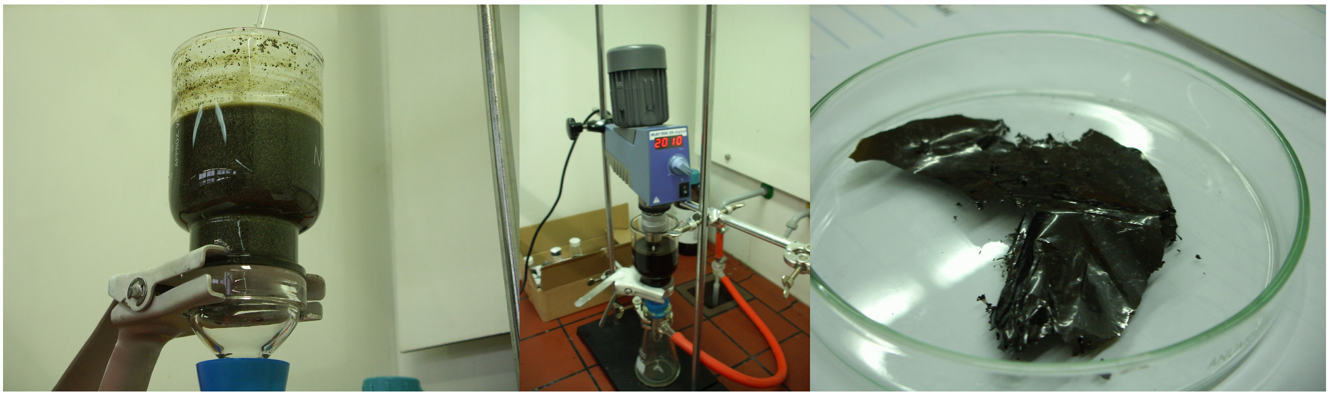

Image 4.1: Left: the oxidized suspension right after the addition of H_2O_2. The yellow-brown tint is visible. Middle: stirring was required during the washing stage to prevent the membrane pores from clogging. Right: a GO film, prepared by slow evaporation of the GO suspension in a Petri dish.

Zhao et al.

"A 2g portion of natural flake graphite with an average size of 500-600μm, 2g of $NaNO_3$ *, and 96mL of concentrated* H_2SO_4 *were mixed at 0°C. During the following stages the mixture was continuously stirred using a magnet stirrer. 12g of* $KMnO_4$ *was gradually added to the above mixture while keeping the temperature at 0°C. The mixture obtained was first stirred at 0°C for 90min and then at 35°C for 2h. Distilled water (80mL) was slowly dropped into the resulting solution, over a period of around 30min, to dilute the mixture. Then 200mL of distilled water was added followed by 10mL of* H_2O_2 *(30%), and the stirring continued for 10 min to obtain a graphite oxide suspension. During this final step,* H_2O_2 *(30%) reduced the residual permanganate and manganese dioxide to colorless soluble manganese sulfate. The graphite oxide deposit was collected from the graphite oxide suspension by high-speed centrifugation at 16000rpm for 10min, and repeatedly washed with distilled water until the pH = 7. Then a mild sonication (80W, 5min) was used to exfoliate the graphite oxide to obtain a GO suspension. To obtain uniform large-area GOs, a low-speed centrifugation at 3000rpm was first used to remove thick multilayer flakes until all the visible particles were removed (3-5min). Then the supernatant was further centrifuged at 5000rpm for 5min to separate large flakes (precipitate) and small flakes (supernatant). Finally, the obtained precipitates containing large flakes were redispersed in water to get a large-area GO sheet suspension."*

Thus, as a starting material, we used the large flakes derived from the Zhao protocol, suspended in water.

First attempts

All the materials, except the N-doped rGO mentioned later on, were prepared following the same protocol. The desired quantity of GO suspended in water was mixed with a solution of each dopant precursor. We opted to dissolve the precursors in solvents which were appropriate for each one and which – if possible – had a low boiling point, so as not to damage the substances before annealing. The precursors were selected based on the heteroatoms or functional moieties that could be produced during pyrolysis and potentially become incorporated into the graphitic lattice. The GO-dopant mixtures would be heated at 55°C-70°C, until the solvents had completely evaporated, under constant stirring. The remaining solid would then be transferred to a drying oven set at 80°C-90°C and left there for several hours. This was done to completely remove any residual solvent, so as to minimize contamination and the possibility of explosive exfoliation of the oxide.

Annealing temperatures ranged from 180°C to 900°C, depending on the sample and the application. For most of the samples, the initial annealing conditions were 700°C for 1h; if the results were promising, we would experiment with different annealing temperatures. At 700°C, most dopant precursors would decompose and at the same time, the lattice would be sufficiently restored. The samples reached that temperature at 10°C/min, under a constant flow of an inert gas (Ar or N_2), inside a tube furnace. Afterwards, the oven was left to cool down, while maintaining the gas flow, until the temperature had dropped to at least 50°C.

The pyrolyzed material would then be washed with a sufficient quantity of the same solvent as the one we had used to dissolve or suspend it, in order to remove any remaining residues of the precursor. It would then go back to the drying oven (set at 100°C-120°C) for several hours, in order to completely remove any solvent, as well as moisture from the atmosphere. Finally, we would place and store the dried material in a sealed container.

The following table lists a number of substances that were used to dope graphene for use in DSSCs, but the resulting materials showed little or no electrocatalytic activity and were subsequently abandoned. All of them were annealed at 700°C:

Table 4.1: List of dopant precursors that had no appreciable electrocatalytic effect.

Compound	Structural formula
N-Boc-pyrrole-2-boronic acid MIDA ester	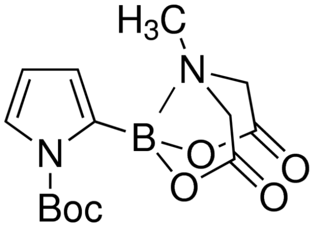
1-(p-Toluenesulfonyl)pyrrole-2-boronic acid MIDA ester	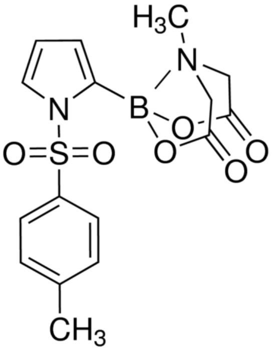

5-Carboxythiophene-2-boronic acid pinacol ester	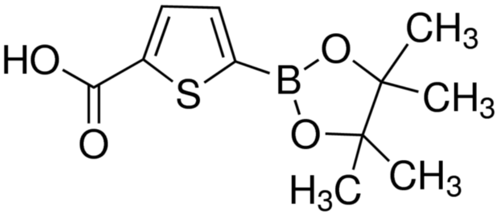
Tris(4-methyl-1-piperazinyl)phosphine	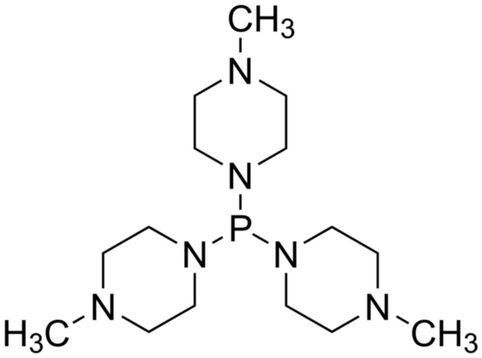
Thiophene-3-boronic acid MIDA ester	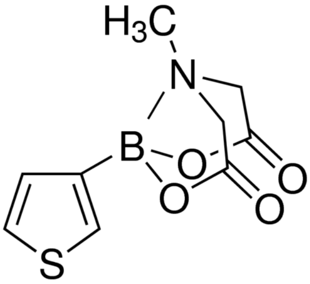
2-Thienylboronic acid	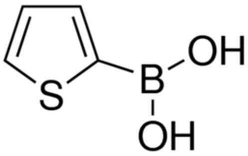
Boron subphthalocyanine chloride	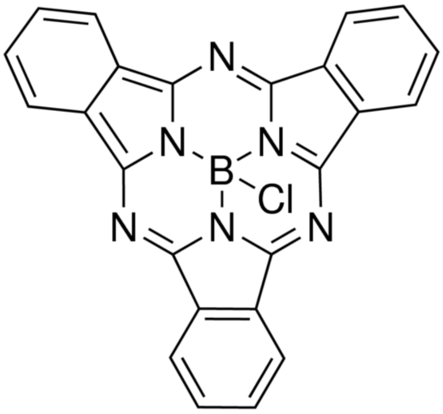
2,5-Bis(5-tert-butyl-benzoxazol-2-yl)thiophene	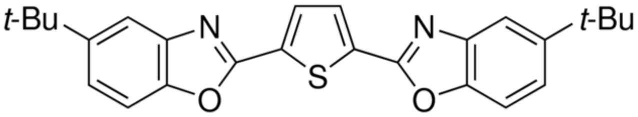
Difluoro{2-[1-(3,5-dimethyl-2H-pyrrol-2-ylidene-N)ethyl]-3,5-dimethyl-1H-pyrrolato-N}boron	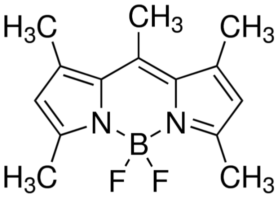

Thieno[3,2-b]thiophene-2,5-diboronic acid bis(pinacol ester)	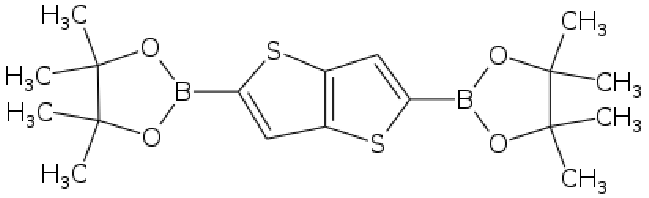
Ethyl 3-amino-5-(4-nitrophenyl)thiophene-2-carboxylate	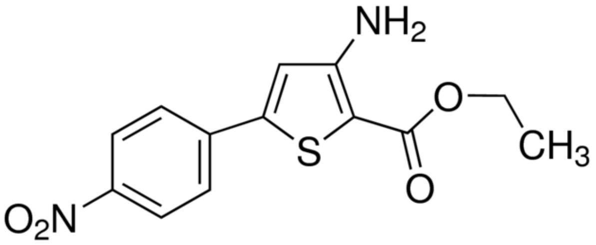
Iron(II) phthalocyanine	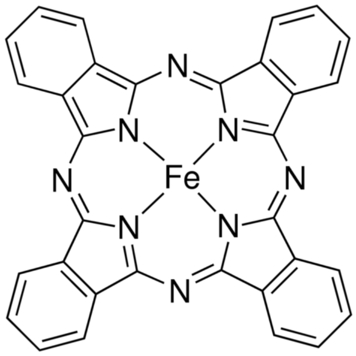
Magnesium phthalocyanine	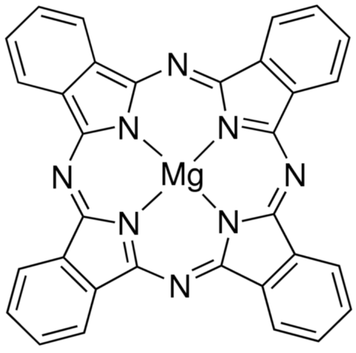

The poor electrocatalytic activity of some of the prepared heteroatom-doped rGO materials could be attributed to the low doping density of heteroatom-containing species into the graphitic lattice. This could be either because of insufficient adducts formed during the co-annealing process, or perhaps due to the expulsion of those species from the hybrid material at a later step, such as during the annealing of the electrodes right after spin coating.

Cobalt(II) phthalocyanine-reduced graphene oxide

30ml of a GO suspension in water (10 mg/ml) were placed in a beaker and were mixed with 60ml of a THF solution, containing 170 mg of cobalt(II)phthalocyanine (PcCo). The organic solution was added drop-wise under continuous stirring to the GO suspension. The mixture was placed onto a metal plate and heated for approximately 10h, until the complete evaporation of the solvents. During that time, the temperature of the metal plate was kept constant at about 70°C and stirring was maintained until the last possible moment. The solid residue was collected from the beaker and placed in an oven for 6h at 90°C. Subsequently, the blend was transferred to a porcelain combustion boat, which was inserted in a horizontal tube furnace. It was heated from room temperature up to 700°C at a rate of 10°C/min under Ar flow, and was left at the elevated temperature for 1h. After that period, the heat was turned off and the oven was allowed to cool to 50°C over a period of approx. 4h, before the combustion boat was removed. The black-colored powder was washed with THF by transferring it to a beaker containing ~30 ml of the solvent, while vigorously stirred. The organic solution turned blue-colored, due to the dissolution of unpyrolyzed phthalocyanine or byproducts of its thermal decomposition. The colored suspension was then filtered over a PTFE membrane (pore size 0.45μm) under vacuum and the doped graphitic material was washed with an excess of THF. The solid was left to dry in an oven at 80°C for 5h and was then stored in a sealed container.

Figure 4.1 depicts the various stages in the synthesis of the rGO-PcCo hybrid material:

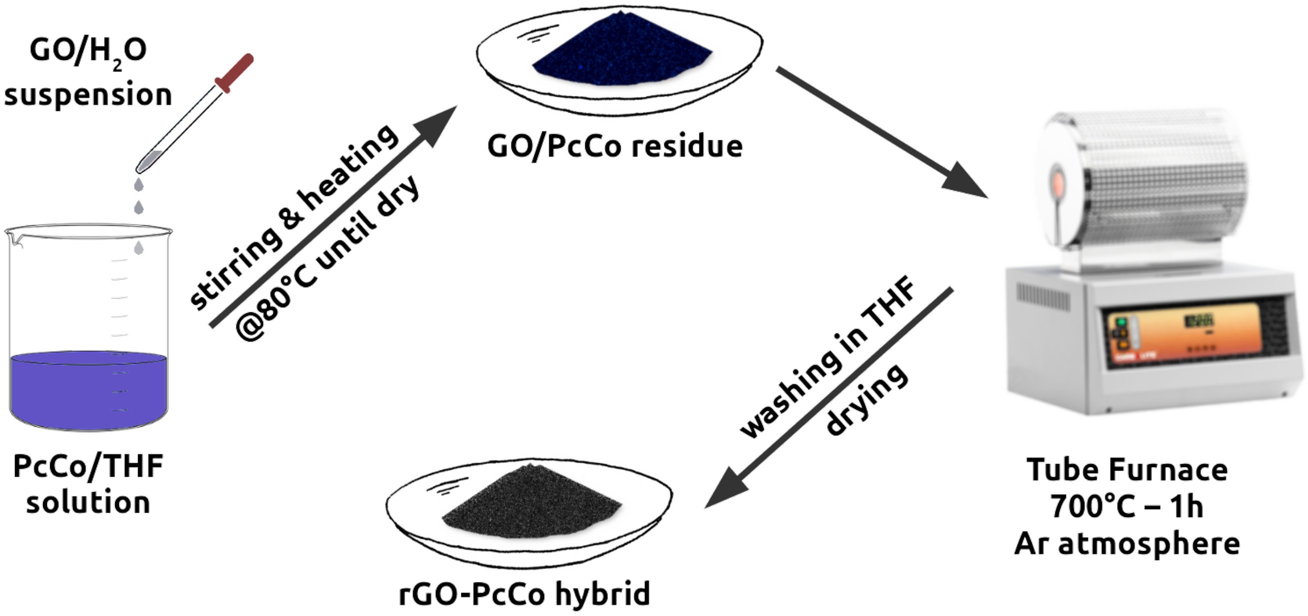

Figure 4.1: Schematic overview of the rGO-PcCo hybrid synthetic process.

Nitrogen-doped reduced graphene oxide

A GO suspension in water (4.5mg/ml) was mixed with aqueous solutions of urea to produce several suspensions with GO:urea mass ratios ranging from 85:15 to 45:55. The best electrocatalytic results were obtained with a ratio of 55:45 (1ml of the GO suspension + 0.4ml of a 0.9mg/ml urea solution). Unlike previous experiments, the solvent was not removed in order to collect the solid; instead, the as-prepared mixture was spin-coated onto FTO-coated glass, which was transferred to a horizontal quartz tube. The glass substrate with the deposited mixture was put in the center of the tube furnace under argon flow. After purging the tube with Ar for about 15min, the furnace was heated up to the programmed annealing temperature at a rate of 5°C/min and kept at that temperature for 15min. Samples were annealed at 180°C, 240°C, 300°C, 350°C, 400°C and 650°C. Subsequently, the furnace was cooled down to room temperature under Ar. The optimum results were obtained after annealing at 350°C.

Figure 4.2 provides an overview of the steps taken in fabricating the FTO substrates coated with the N-doped rGO/PEDOT composite films:

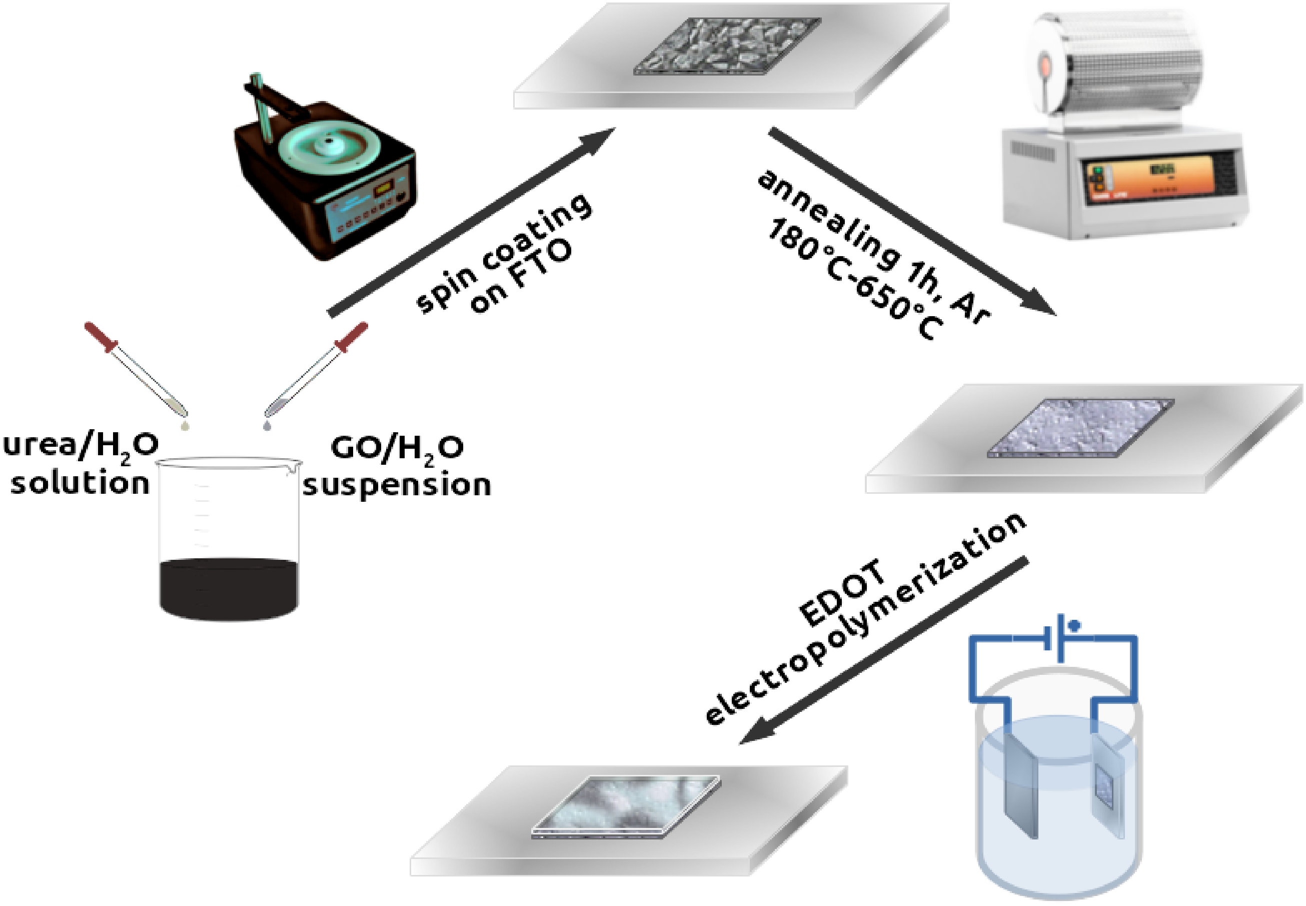

Figure 4.2: Schematic overview of the fabrication process of the N-doped rGO/PEDOT films.

Fabrication of DSSCs

Photoanode

FTO-coated glass substrates were cut in the desired dimensions (1.5cm x 2cm) and washed with a mild detergent, distilled water and subsequently with ethanol and acetone in an ultrasound bath, finally dried under air stream. A compact thin layer of TiO_2 was formed by aerosol spray pyrolysis using a solution of 0.2M titanium diisopropoxide bis(acetylacetonate) in ethanol and the coated substrates were then heated for 1h at 500°C. Subsequently, a mesoporous TiO_2 layer composed of titania paste made of P25 nanoparticles was deposited by doctor blading on the above compact layer and calcined for 15 min at 500°C. The last step was repeated twice more, so as to obtain a film about 10μm thick. Finally, a layer of $TiCl_4$ was deposited by dipping the patterned electrode in a solution of 0.04M $TiCl_4$ in H_2O for 30min and annealed at 500°C.

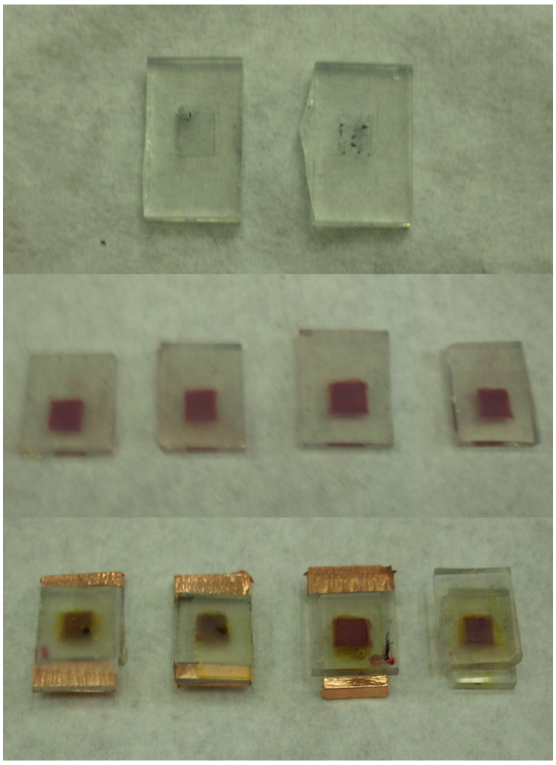

Image 4.2: Top: CEs coated with Pt (left) and a sample (right). Middle: photoanodes after dye adsorption. Bottom: assembled devices.

The active area of the film was made to match that of the counter electrode, e.g. 0.4cm x 0.4cm. Then the integrated photoanode electrode was dipped in the solution of the dye (0.5mM N719 dye in ethanol and 5mM chenodeoxycholic acid) for 24h. After the dye and the additive had been adsorbed, the samples were rinsed with ethanol, dried in a N_2 stream and used as photoanodes in the DSSCs.

Counter-Electrodes

Pt reference

For the sake of comparison, counter-electrodes with Pt as the electrocatalyst were constructed. A solution of 0.02M hexachloroplatinic acid in isopropanol was twice spin-coated (1000rpm) on an FTO-coated glass and it was annealed at 500°C. The dimensions of the active surface were tailored to match those of the tested CEs.

rGO-PcCo

The rGO-PcCo hybrid was dispersed (5mg/ml) in an isopropanol/water (2:1) mixture by ultrasonication for 2h. The mixture was spin-coated (1500rpm for 30s) as thin film on FTO-coated glass. The procedure was repeated twice. Finally, the samples were annealed at 350°C for 30min to complete the counter electrode fabrication. The active surface was 0.4 x 0.4cm^2.

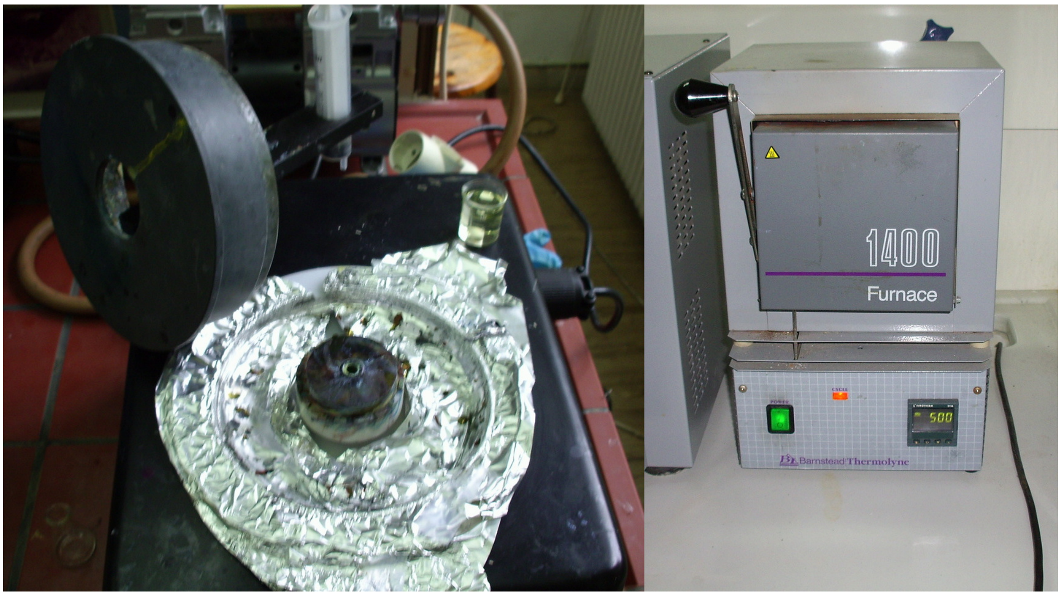

Image 4.3: Left: the vacuum spin coater used in the preparation of the films. A beaker containing hexachloroplatinate solution is also visible. Right: the furnace in which the hexachloroplatinate films were annealed to metallic Pt.

N-Doped graphene/PEDOT composites

N-doped graphene was prepared as described earlier, directly onto FTO-coated glasses. These were then combined with PEDOT, to yield the composite films.

PEDOT was deposited on either untreated or thermally annealed GO-urea films by potentiostatic electrodeposition, using the corresponding 3,4-ethylenedioxy-thiophene (EDOT) monomer. In the electrodeposition process, a potential of +2V was applied for 2s in a three-electrode setup using the doped-GO/FTO as working electrode, Ag/AgCl (reference electrode), Pt sheet (counter electrode) and acetonitrile as solvent. The acetonitrile solution contained 0.2M EDOT and 0.1M $LiClO_4$. Finally, the film was washed with acetonitrile several times and dried in a vacuum oven. The thicknesses of the GO-urea and rGO-urea films were ∼10nm and ∼5nm, respectively. Concerning the samples characterized by XPS analysis, a thin PEDOT layer was electrodeposited (thickness ∼8nm).

Electrolyte

The liquid electrolyte was prepared by mixing solutions of 0.5M 1-methyl-3-propylimidazolium iodide, 0.1M lithium iodide, 0.05M iodine and 0.5M tert-butylpyridine under prolonged magnetic stirring.

Chapter Bibliography

[1] Kovtyukhova, N. I.; Ollivier, P. J.; Martin, B. R.; Mallouk, T. E.; Chizhik, S. A.; Buzaneva, E. V.; Gorchinskiy, A. D. Layer-by-Layer Assembly of Ultrathin Composite Films from Micron-Sized Graphite Oxide Sheets and Polycations. *Chem. Mater.* **1999**, *11* (3), 771–778 DOI: 10.1021/cm981085u.

[2] Zhao, J.; Pei, S.; Ren, W.; Gao, L.; Cheng, H.-M. Efficient Preparation of Large-Area Graphene Oxide Sheets for Transparent Conductive Films. *ACS Nano* **2010**, *4* (9), 5245–5252 DOI: 10.1021/nn1015506.

5. Results – Discussion

Graphene Oxide – reduced Graphene Oxide

As it was mentioned earlier, we used three different GO batches for our experiments: the first and the third were prepared according to the method described by Kovtyukhova et al.[1] and the second one according to that of Zhao et al.[2]. After each batch was prepared, a sample was collected by slowly heating the suspension at ~50°C until all the water had evaporated. These samples were studied with XRD (Figure 5.1).

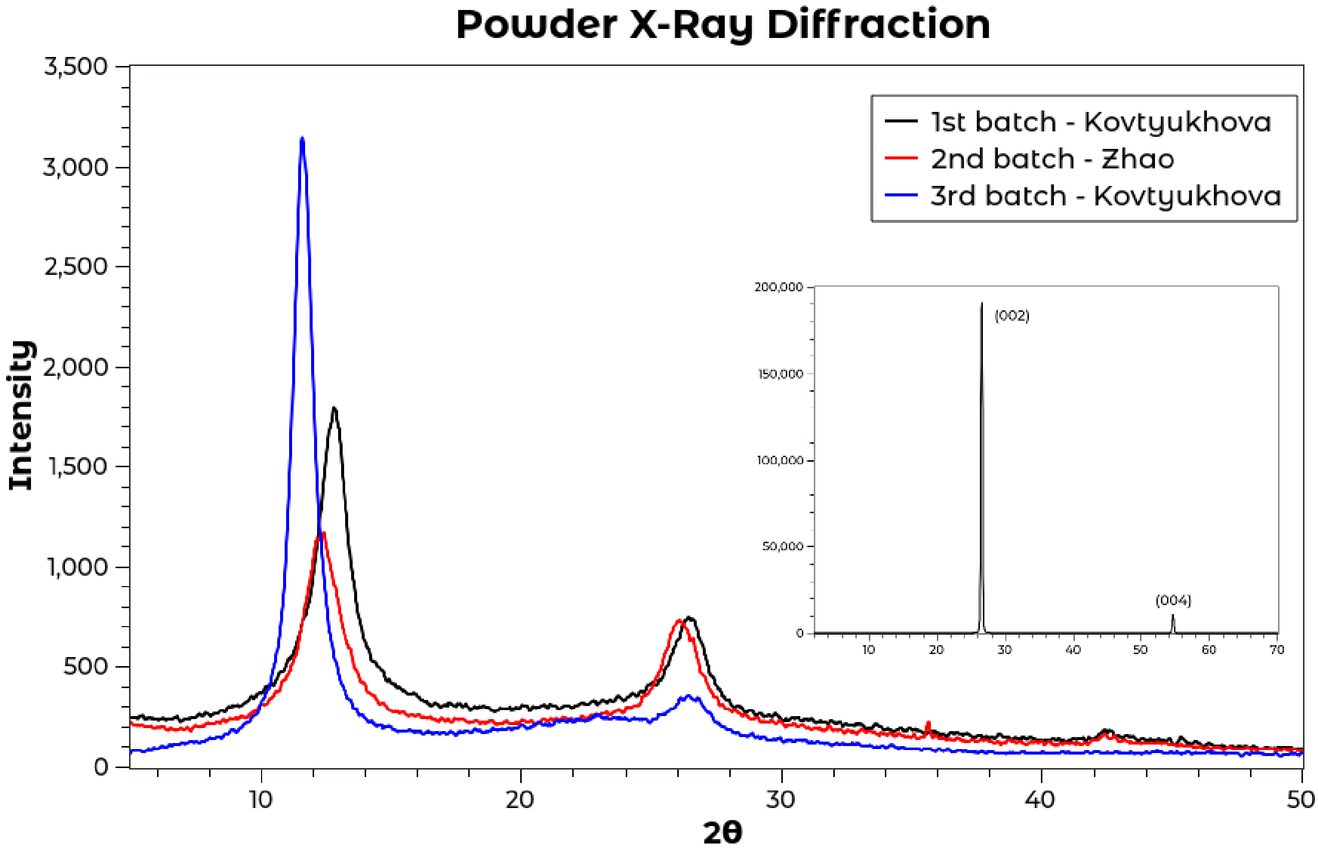

Figure 5.1: Powder X-ray diffractograms of the three different batches of GO.

It is immediately apparent that there are minor differences between the three samples. The main reflection of the (002) family of planes in graphite, which is located at 26.5°, has shifted by a different degree in each of them. From Bragg's Law (for λ=1.54178Å, n=2) we can calculate the spacing between adjacent sheets in each batch (Table 5.1).

Since no other process was involved, we can safely deduce that the difference in interplanar spacing is the result of a different degree of oxidation. The added, oxygen-containing functional groups are the ones pushing the sheets apart, to more than twice their original distance. As the spacing increases, water molecules, attracted by the newly added polar groups, enter the channels and become adsorbed between the layers of the oxide.

Table 5.1: Measured 2θ value and calculated interplanar spacing for each GO batch.

GO Batch	2θ	d
1	12.8°	6.96Å
2	12.3°	7.24Å
3	11.6°	7.67Å

We also notice that there are graphitic residues in all of the samples. While we can not directly quantify the signal centered at 26.5°, in general, a broad peak corresponds to a smaller particulate size. From that, we can hypothesize that the unoxidized graphitic regions in the crystallites are relatively small. For the third sample, we might say with a certain degree of confidence, that a smaller portion of material (compared to the other two) remained intact.

The small, yet discernible peak at ~42.5° in the diffractograms of the first and the second sample, is completely absent in that of the third. This is another indication that the third sample has been heavily oxidized, moving further away from its former graphitic structure than the other two samples.

After these results, we wanted to see if there were any differences between their thermal reduction products, especially between those that were produced following a different protocol. Figure 5.2 depicts the diffraction patterns of rGO samples from the second and third batches (the other was removed for clarity), which where annealed at 700°C for 1h:

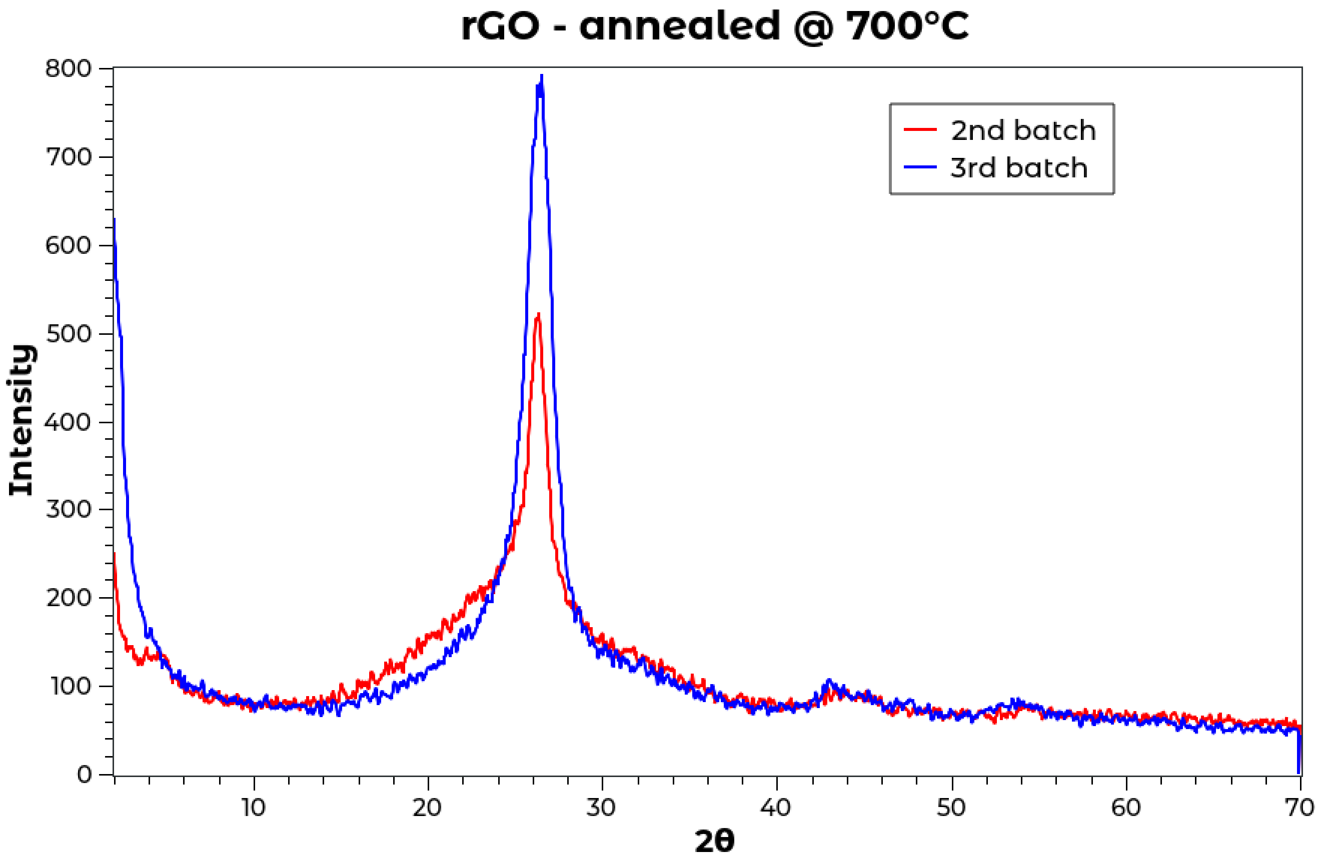

Figure 5.2: PXRD patterns of thermally reduced GO samples from batches 2 &3.

For all intents and purposes, both samples appear identical. In fact, every sample that was treated at the same temperature and for the same amount of time, displayed the exact same diffraction patterns. An obvious conclusion is that regardless of any initial dissimilarities, samples undergoing the same thermal reduction treatment, will eventually adopt the same structural conformation.

The sample from the second batch has a noticeably broad shoulder from ~13° to 24°, compared to that of the third batch. The Zhao process that was used in producing the batch, involved the separation of the graphene particles according to their size. We used the fraction with the larger-area graphene sheets. Due to their size, it is difficult for them to re-stack in an orderly fashion, which results in creases and intertwined formations. This disordered conformation, with many interstitial gaps, is most probably the reason for this consecutive series of reflections.

One might wonder about the intensities of the reflections in GO and rGO and in particular why after the restoration the signal is not stronger, since the (002) reflection returns to 26.5°. We discussed earlier, that as the temperature rises, CO_2, resulting from the decarboxylation of COOH groups and water/solvent molecules, adsorbed between the graphene oxide sheets start to escape. As their kinetic energy increases, they may force the sheets apart on their way out, resulting in the exfoliation of the crystallites. For that reason, we expect thermally treated GO specimens to be of fewer layers than the parent material.

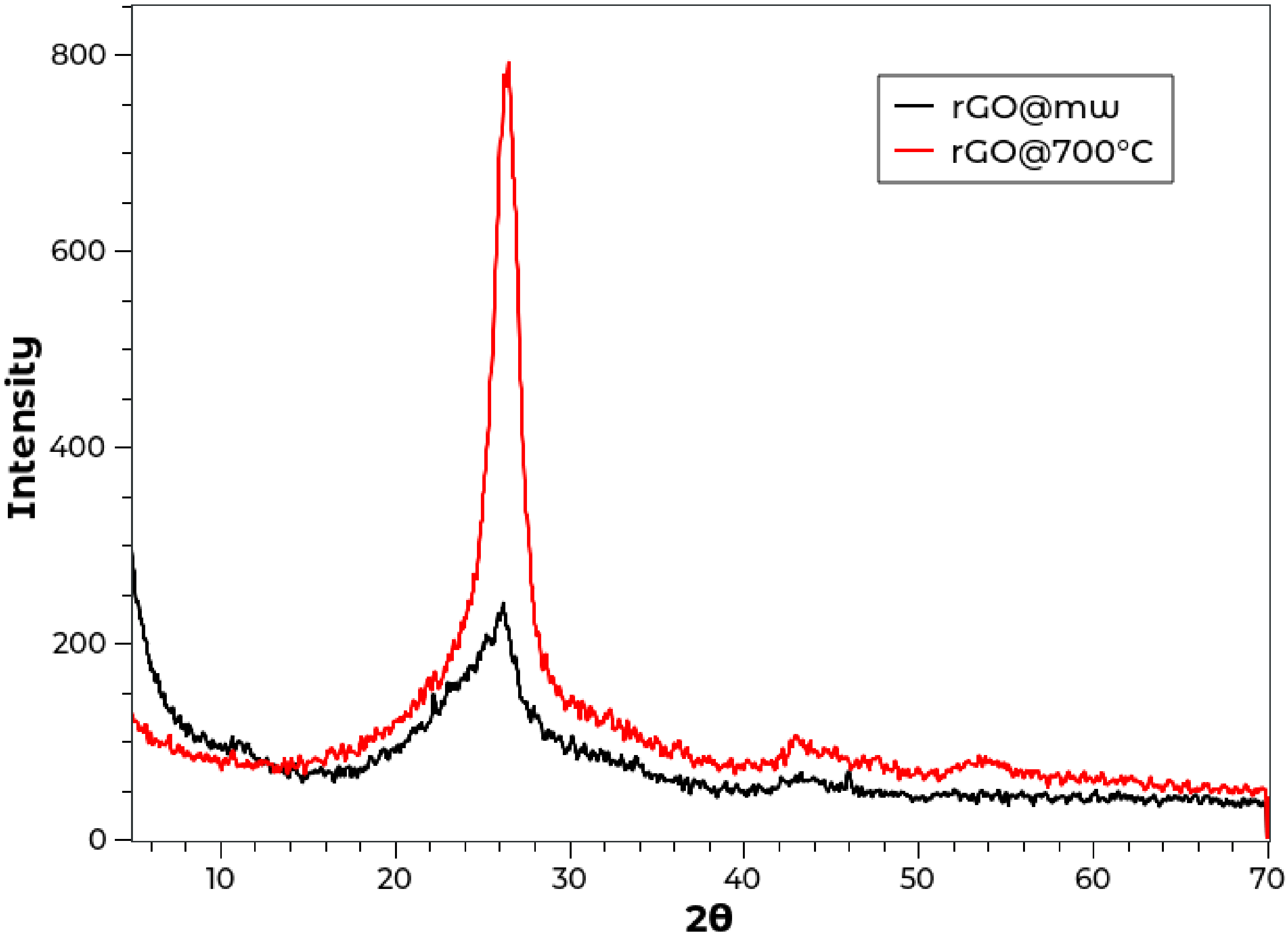

Figure 5.3: Powder X-ray diffractograms of microwave treated GO (black) and rGO annealed at 700°C for 1h.

For our future experiments, we wanted to see if a microwave treatment could be a viable alternative to the thermal one. To that end, we used a household microwave oven to anneal a GO membrane, formed by placing a quantity of GO suspension (Kovtyukhova) in a Petri dish and slowly evaporating the water. We set the sample on the rotating platter and dialed the magnetron to 700W (maximum setting). We retrieved it after 30s of irradiation (amid broken shards of glass, as the Petri dish was shattered because of the uneven and intense heating of the material). During those seconds, the radiation waves traced patterns on the film, accompanied by small bursts of vapors and finely powdered material. Apparently, it was a very localized form of "explosive exfoliation". We used powder X-ray diffraction (Figure 5.3) and Raman spectroscopy (Figure 5.4) to compare it to a sample annealed at 700°C for 1h and to the original material.

The fine black powder gave a significantly less intense reflection at 26.5°. This observation agrees with the "explosive exfoliation" hypothesis, as the sudden, concentrated heating caused by the waves, would result in gases escaping more violently than in a furnace, where the temperature is raised by 10°C/min. In turn, this would translate to a material with less sheets stacked together.

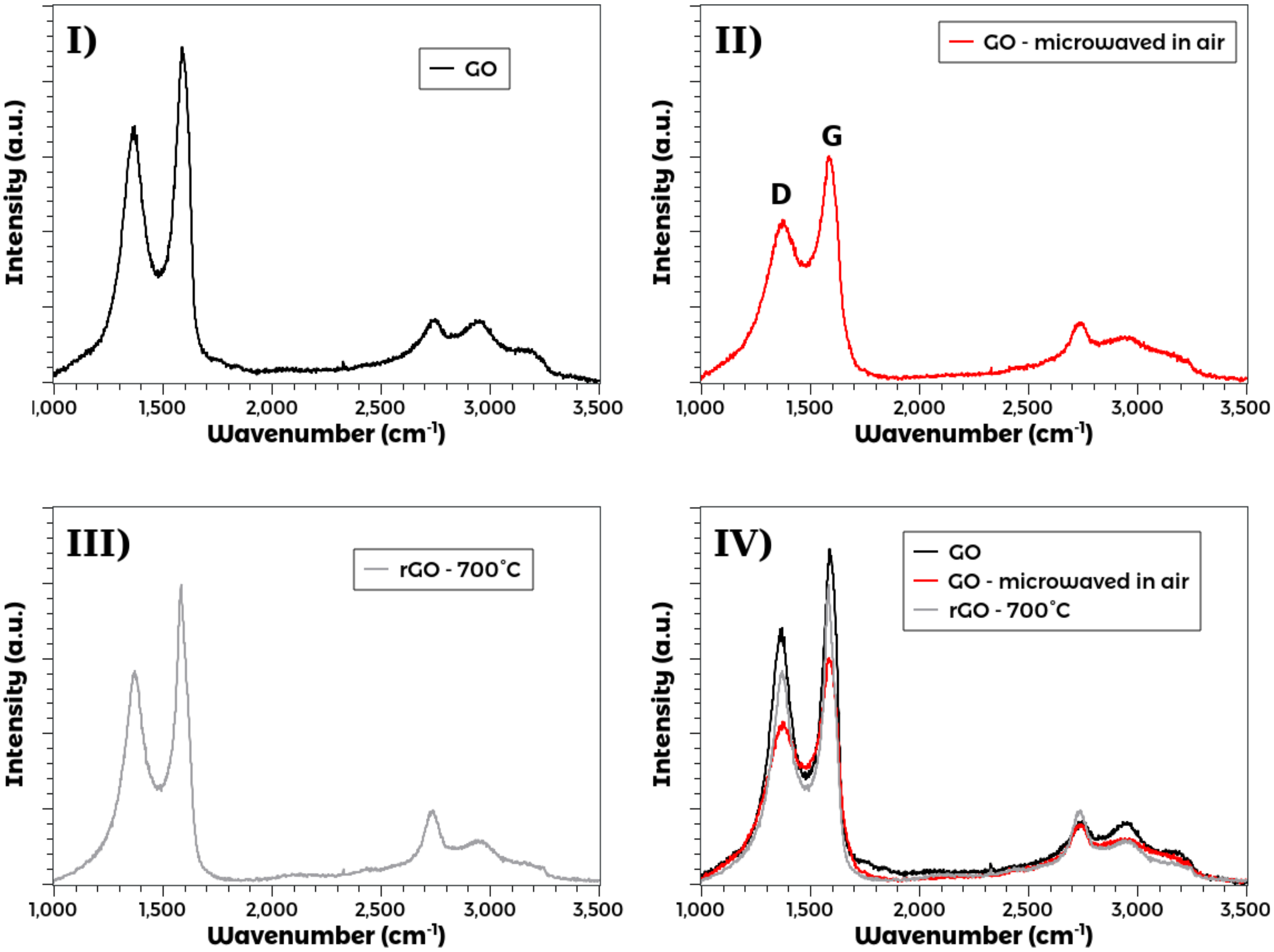

Figure 5.4: Raman spectra of: I) untreated GO, II) GO membrane treated in a microwave oven for 30s, III) rGO annealed at 700°C for 1h and IV) a superposition of the spectra. Bands D and G are marked in II).

The I_D/I_G ratios for the untreated GO, the microwaved sample and the thermally treated one were 1.22, 1.33 and 1.34 respectively. One might expect that the D/G intensity ratio in thermally treated GO would be lower than that of the starting material. This implies that the graphene films prepared by thermal reduction of GO possess additional defect sites. The increased I_D/I_G ratio of rGO after thermal reduction has been commonly reported in the literature[3] and could be ascribed to a slight decrease of the sp^2 domain size, due to possible fragmentation of graphene sheets throughout the basal plane. The latter process induces the generation of additional defect sites at the periphery of doped rGO flakes. However, the calculated ratios suggest that a microwave treatment of just 30s is sufficient to induce the same structural changes to the graphitic lattice as the thermal treatment of 1h at 700°C.

One very obvious drawback of this process, is that an inexpensive household oven produces a fixed pattern of waves. Despite the rotation of the platter, the specimen is irradiated unevenly, with some zones never receiving any radiation at all. Graphene oxide is an insulator and as such, it does not exhibit induced currents throughout the bulk of the material, that could help expand the effects of radiation. Still, the reduced material was easy to separate from the oxide, as the latter remained affixed to the glass surface, on which the membrane was formed. The process could be improved through the use of reflectors, or by suspending graphene oxide in a suitable solvent and irradiating it for longer periods of time.

Failed attempts

For most of the materials we tested as counter-electrodes in DSSCs, the current-voltage curves looked something like this:

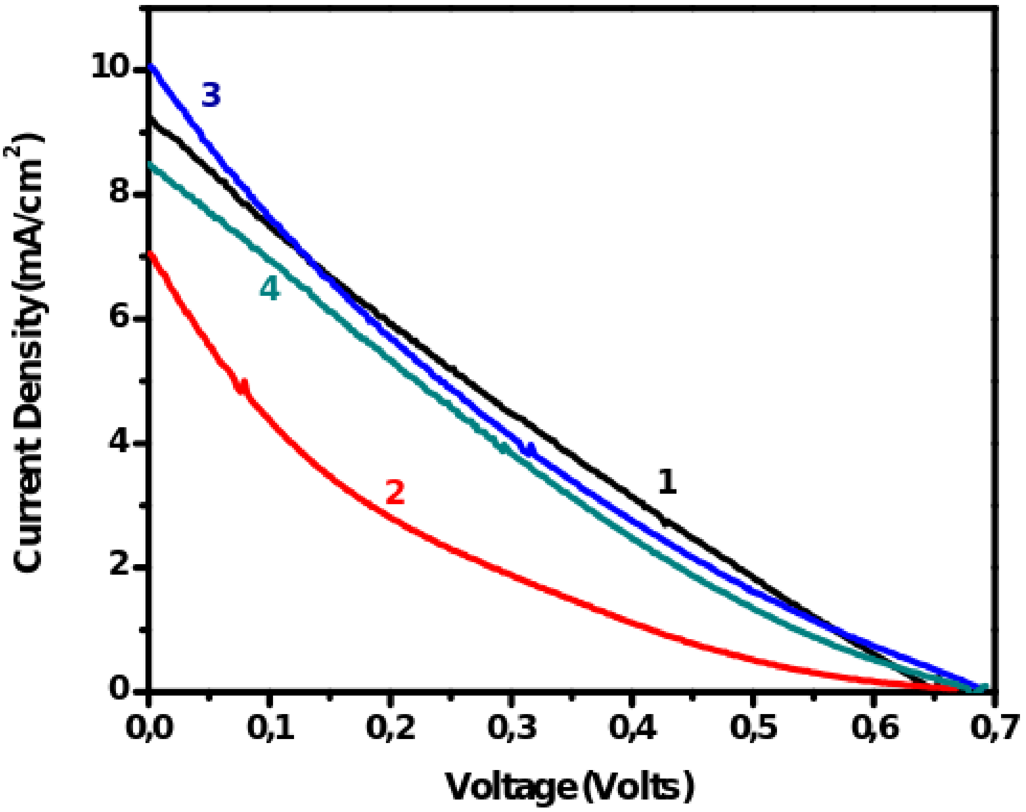

Figure 5.5: I-V plots for some unsuccessful counter-electrodes.

These four measurements are actually of two different, untreated mixtures of PcCo with exfoliated graphene (1 & 2) and with thermally annealed rGO (from the Zhao batch, curves 3 & 4). We had been experimenting with various coating methods, such as spray coating (2 & 4) and trapping the material in the interface between two non-miscible solvents (1 & 3). While both of these methods work very well with plain glass, the hydrophobicity of the FTO and ITO coatings resulted in non-uniform coverage of the substrates. In any case, the other unsuccessful materials displayed similar current-voltage characteristics. For the record, the best conversion efficiency was that of sample 1 (interface trapped graphene + PcCo), measured at 1.36%.

Samples 1 and 4 demonstrate a linear response as the rheostat's internal resistance goes from zero to infinity. These counter-electrodes function as simple resistors and have no electrocatalytic activity. The concavity of the curves for the samples 2 and 3, indicates that they are actively hindering the power production of the devices, probably through some form of induction or capacitance or both. These two are actually slowing down the regeneration of the redox pair. To at least consider a material as an electrocatalyst in a photogalvanic element, its characteristic I-V curve should be somewhat convex. Of course, its V_{OC} and I_{SC} values should be close to or better than those of the Pt reference.

rGO-PcCo

The rGO-PcCo hybrid, made from the first GO batch (Kovtyukhova), was our first successful attempt. The electrocatalytic performance of the counter-electrode made from that material closely matched that of the Pt reference electrode.

PV efficiency

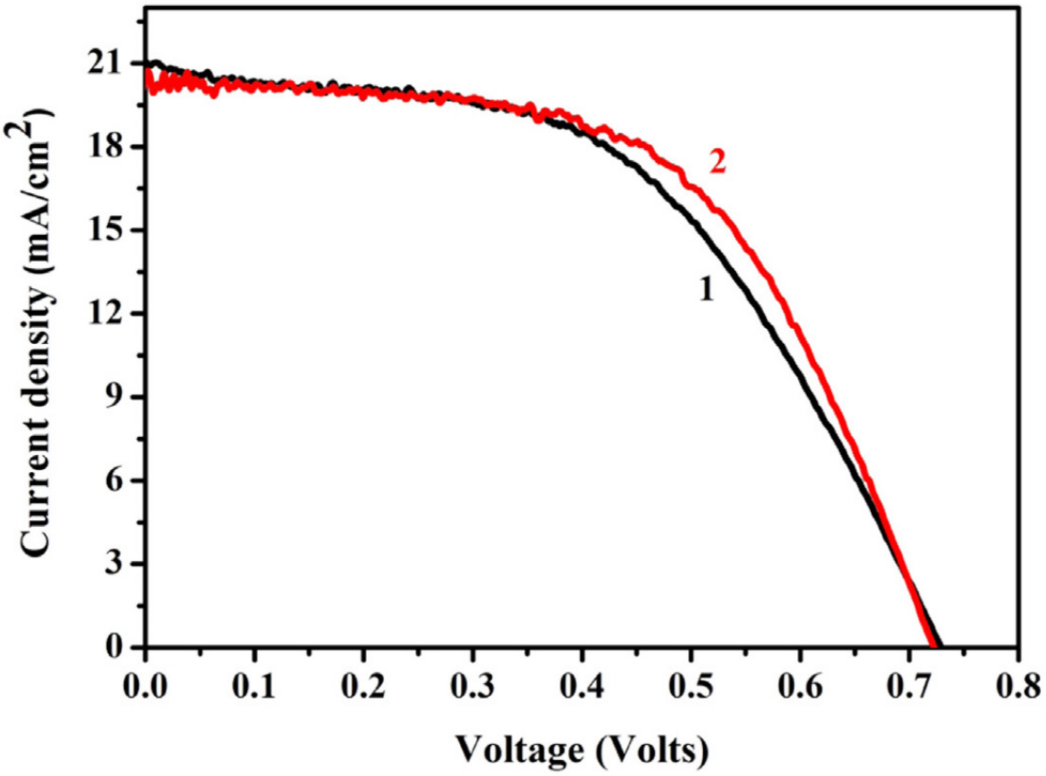

Figure 5.6: Current density-voltage curves obtained with DSSCs made with different counter electrodes: 1) rGO-PcCo and 2) Pt.

From the plot above, it is obvious that the counter-electrode coated with our material can compete with Pt and perhaps after some optimization, it could outperform it.

Table 5.2: Current–voltage data extracted from Figure 5.6

Counter electrode	I_{SC} (mA/cm^2)	V_{OC} (Volt)	Fill Factor	η%
rGO-PcCo	21.0	0.73	0.51	7.82
Pt	20.3	0.72	0.57	8.40

The data contained in Table 5.2 reveal that the rGO-PcCo hybrid produces a slightly higher open circuit voltage, a slightly lower short-circuit current. The fill factor of the plot is 51%, vs 57% for Pt, which means that the power output of the device is a little lower, as is its light-to-electricity conversion efficiency, 7.82% for the hybrid, 8.4% for Pt.

Cyclic Voltammetry

Cyclic voltammetry measurements in Figure 5.7 corroborate that story:

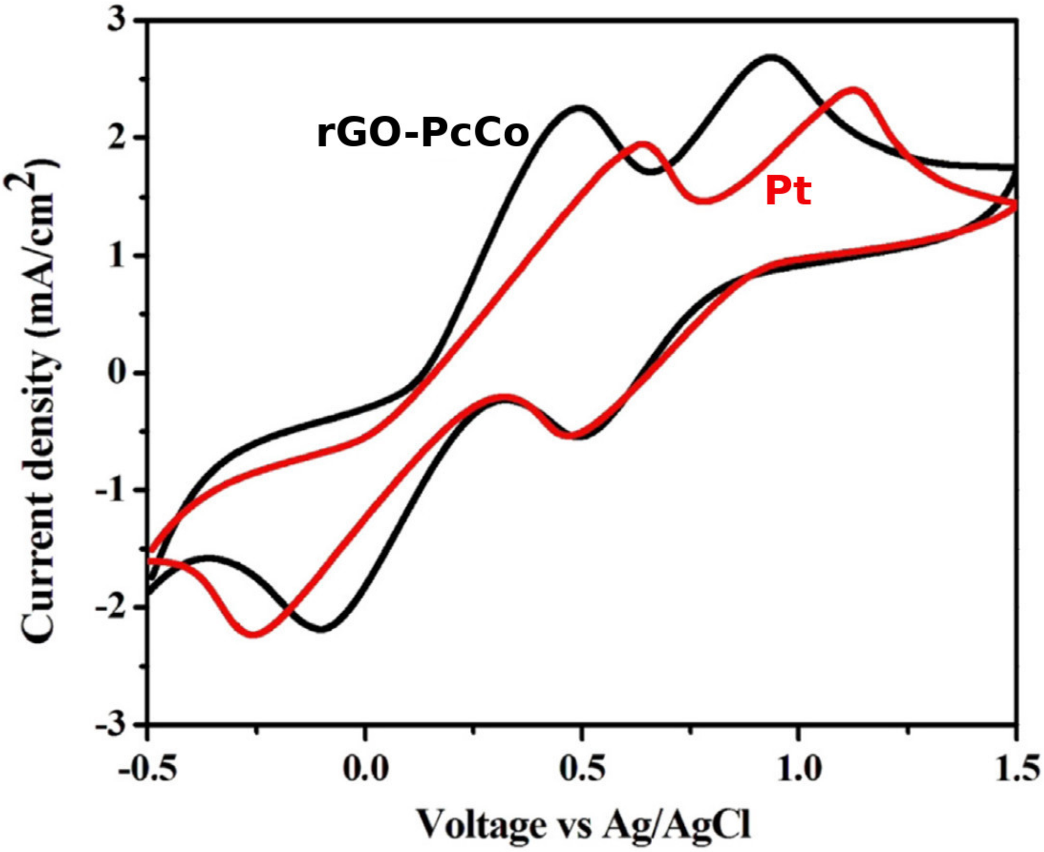

Figure 5.7: Cyclic voltammograms recorded with rGO-PcCo and Pt supported on an FTO electrode, using Ag/AgCl and a platinum sheet as reference and counter electrodes respectively. The electrolyte was 0.1M $LiClO_4$, 0.001M I_2 and 0.01M LI in acetonitrile.

There are no extraneous peaks in the voltammogram, which means that there are no secondary redox reactions taking place in the system. The reduction peaks for the rGO-PcCo hybrid display a higher current density than Pt, but at the same time, the peak separation (the horizontal distance between a reduction peak and the corresponding oxidation one) is smaller. As we have already discussed, both factors are an indication of electrocatalytic activity.

The higher difference between peak potentials for Pt, hints at a faster charge transfer rate at the electrode-electrolyte interface. Both voltammograms were recorded in the same solution, at the same scan rate and both films (Pt and rGO-PcCo) covered the same geometric area on the FTO support. It would stand to reason to attribute the higher cathodic current of the rGO-PcCo film to it possessing a higher specific surface area. A larger surface area would allow more electrolyte ions to come into contact with active sites on the counter-electrode per unit of time, increasing the measured current.

Electrochemical Impedance Spectroscopy

As we continue our investigation of the electrocatalytic activity of the rGO-PcCo counter-electrode, we turn to EIS for more clues.

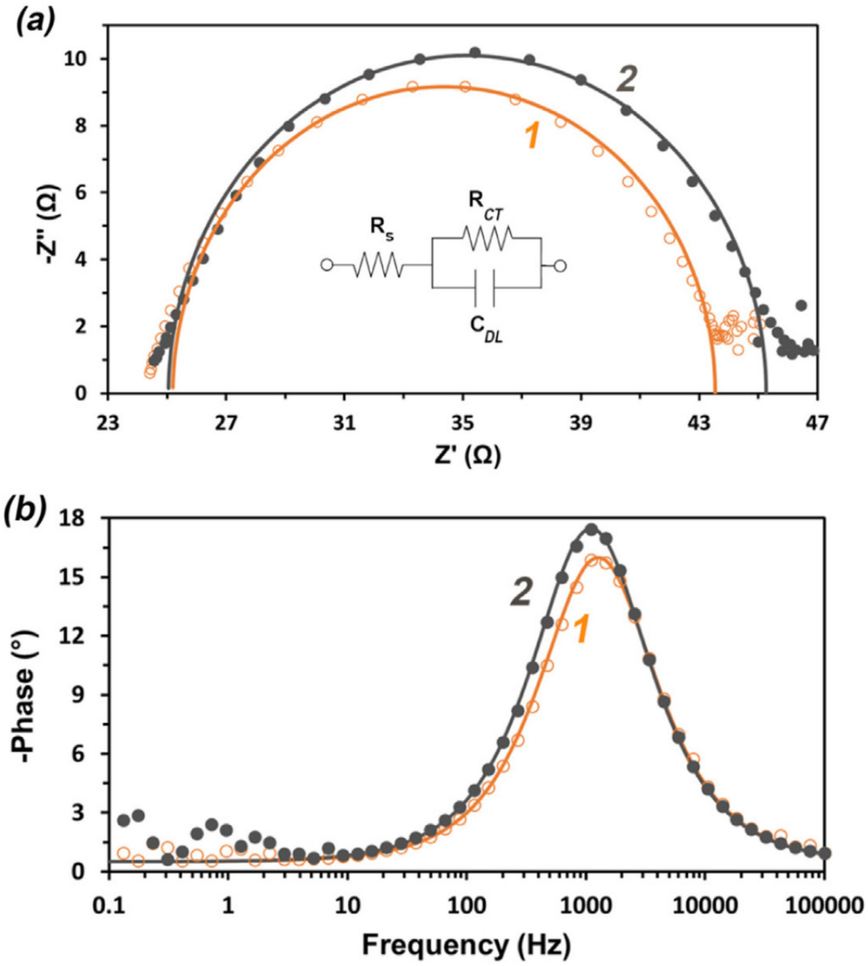

Figure 5.8: (a) Nyquist plots (the inset is the extrapolated equivalent circuit) and (b) Bode phase plots obtained by EIS measurements on symmetric dummy cells using two electrocatalysts: (1) Pt and (2) rGO-Pc.Co The experimental data are marked with circles and dots and the solid lines are the fitted curves.

Both materials display an almost identical frequency response, with rGO-PcCo exhibiting a slightly higher impedance than Pt. The automatically extrapolated equivalent circuit for each counter-electrode is that of a constant phase element, which models an imperfect capacitor and it is the same for both of them, another indication of their similarities. The circuit consists of a resistor, R_{CT}, representing the charge-transfer resistance of the material, connected in parallel with a capacitor, C_{DL}, which corresponds to the double layer capacity of the electrode-electrolyte interface and accounts for polarization effects occurring there. The two of them are connected in series with a resistor, R_S, (active electrolyte resistance) which roughly corresponds to the Ohmic resistance of the material.

EIS measurements yielded the data listed in Table 5.3:

Table 5.3: Data from EIS measurements.

Counter electrode	**R_S (Ω)**	**R_{CT} (Ω)**	**C_{DL} (μF)**
rGO-PcCo	24.5	20.18	8.92
Pt	25.2	18.40	8.97

The rGO-PcCo hybrid fares better than Pt in terms of conductivity (lower R_S) and it exhibits a slightly lower capacitance, but it has a higher charge-transfer resistance than platinum, almost by 10%. This finding confirms what we observed in the voltammogram, i.e. that the electron transfer takes place faster in the Pt-electrolyte interface.

UPS

To complete the electronic characterization of rGO-PcCo, we used UPS to measure its ionization potential (IP) and calculate its work function. The spectrum in the whole range of energies is shown in Figure 5.9b. A magnification in the valence band region (near the Fermi level) is shown in Figure 5.9a. The peak at ~1.3eV assigned to Co3d valence states, originates from the interaction of the Co3d electrons with those of the nitrogen electrons. The HOMO cut-off was found to be 0.5eV. Figure 5.9c is a magnification of the high binding energy cut off from which the work function was calculated to be 4.4eV.

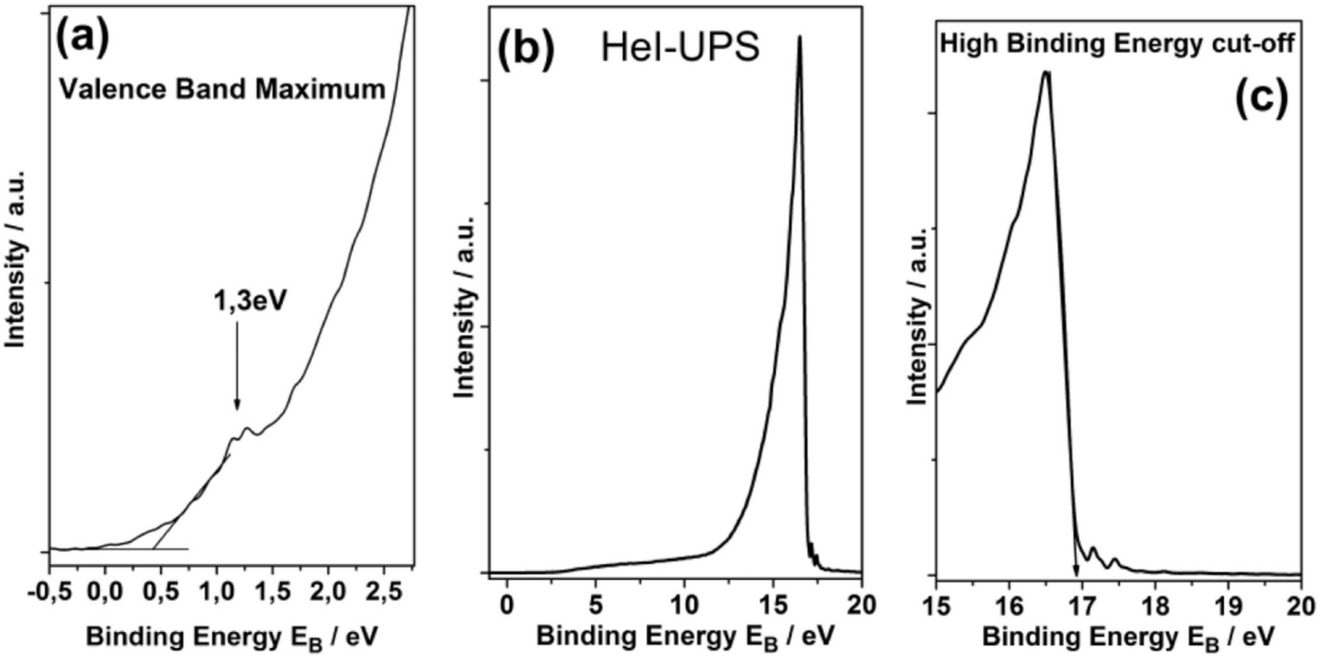

Figure 5.9: UPS spectra of an rGO-PcCo film. (a) the valence band region (b) the full spectrum and (c) the high binding energy cut off.

The IP was calculated by adding the absolute energy values of the work function and the HOMO cut off: (4.4+0.5)eV = 4.9±0.1eV. The work function of Pt is 5.12–5.93eV, therefore rGO-PcCo is more favorably located to become an electron donor. Its equivalent electrochemical potential is equal to +0.4V vs NHE, very close to that of the redox potential of the I^-/I_3^- pair, which is around +0.35 V vs NHE.

XPS

The composition of the rGO-PcCo hybrid was investigated via its XPS spectrum.

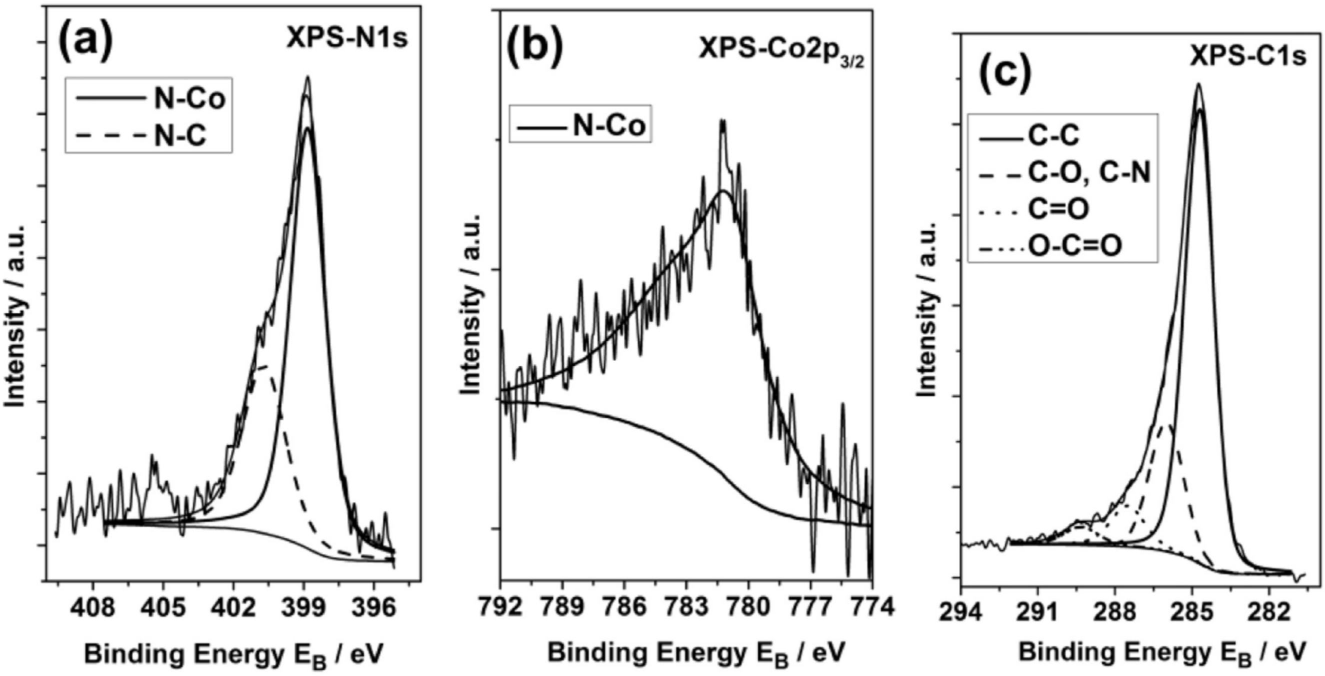

Figure 5.10: XP spectra of (a) N1s , (b) Co2p$_{3/2}$ for an rGO-PcCo film on ITO and (c) Deconvoluted XP spectra of C1s for the rGO-PcCo film.

Figures 5.10a and 5.10b show the N1s and Co2p 3/2 XP spectra of doped material, respectively. The N1s spectrum consists of two components, at binding energies 398.9±0.1eV and 400.5±0.1eV, assigned to N in PcCo-type functionalities and N in amine/amide/pyrrolic bonds, respectively. The presence of the latter component indicates that N (deriving from PcCo) is bonded to the defect sites of rGO flakes. The binding energy of the Co2p$_{3/2}$ peak is assigned to the central metal ion in PcCo-based fragments. Figure 5.10c shows the analyzed C1s core level peak. The peak is deconvoluted into four components, assigned to C–C bonds at binding energy 284.7±0.1eV, C–O and C–N bonds at 286.5±0.1 eV, C=O bonds at 288.0±0.1eV and O–C=O at 289.3±0.1eV. The shape of the peak is characteristic of an rGO film.

Within the structure of the doped material, the atomic N:Co ratio can be calculated by dividing the peak area of N1s and Co2p with the appropriate relative sensitivity factor after making appropriate corrections. Thus, the N:Co atomic ratio was calculated to be about 3:1, with the nominal being 8:1. This implies that cobalt-nitrogen fragments of CoN_3 type seem to decorate the graphitic lattice, rather than the parent dye molecules. In conclusion, XPS studies showed the presence of dye fragments grafted at defect sites of reduced graphene oxide. Specifically, from the N1s and Co2p peak intensity ratio, it was verified that CoN_3 type fragments are attached onto the rGO lattice. The mass of the fragments was estimated to be 2.2±0.1% of the hybrid material, based on the relative intensities of all the elements belonging to the sample.

Keeping in mind that the quantitave results of XP spectroscopy are given with a significant margin of error and having seen the PXRD pattern of the hybrid material, we were a bit skeptical of that last finding, the 3:1 N:Co ratio. We also came across the doctoral thesis of Dr. Petraki[4], who found that XPS failed to provide accurate measurements on deposited films of phthalocyanines below a certain thickness.

PXRD

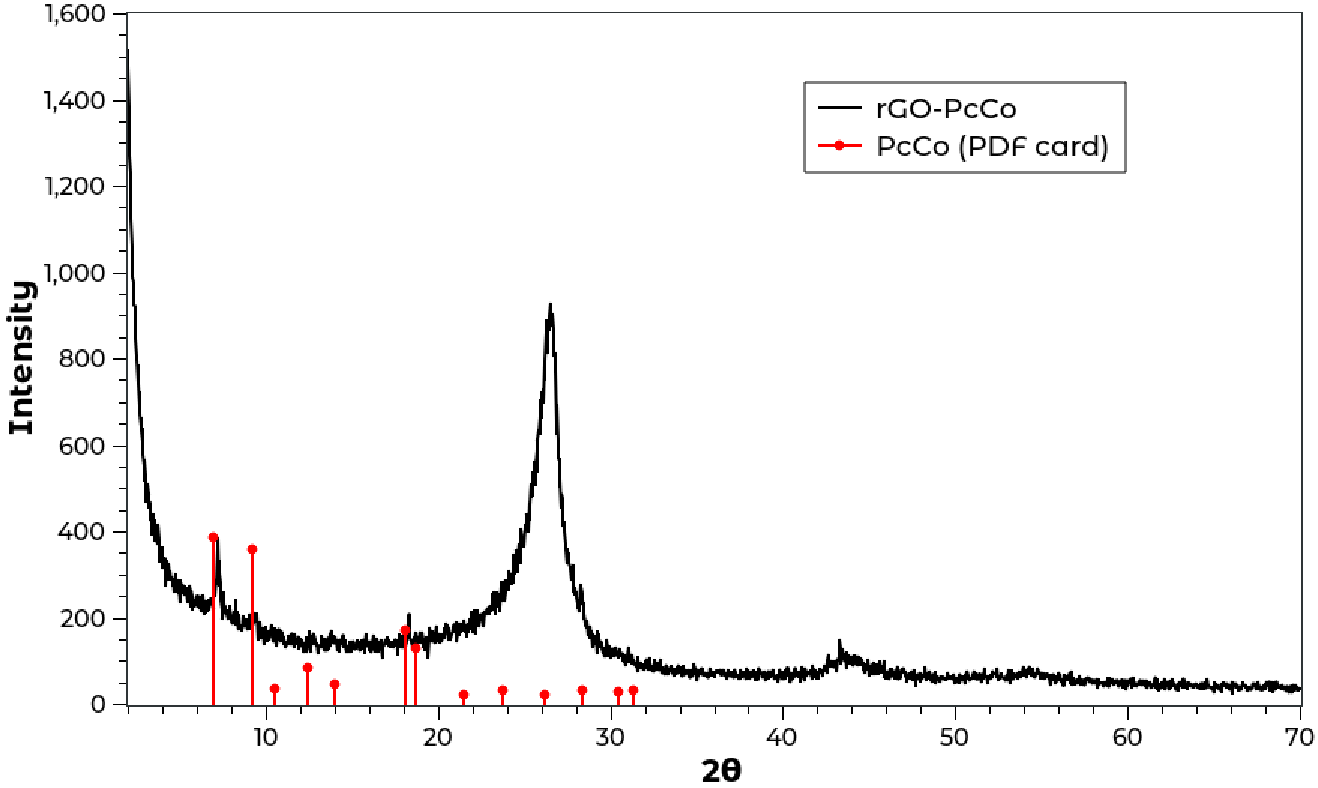

Figure 5.11: X-ray diffraction patterns of the rGO-PcCo hybrid (black) and of cobalt(II) phthalocyanine (red).

In the powder diffraction pattern of the hybrid material we observe the expected reflection of the (002) family of planes as well as two broader and less intense peaks at 43.5° and 54.5°, which are also assigned to a graphite-like structure, corresponding to the (100) and (004) crystallographic planes. In addition to those, there are three distinct peaks at 7.3°, 9.5° and 18.3°. These are attributed to a polymorph of PcCo, which means that there is a measurable quantity of PcCo in the hybrid material that retains its crystalline form.

Puzzled by the conflicting results from the XPS and PXRD measurements, we continued to examine the material with other techniques.

Raman

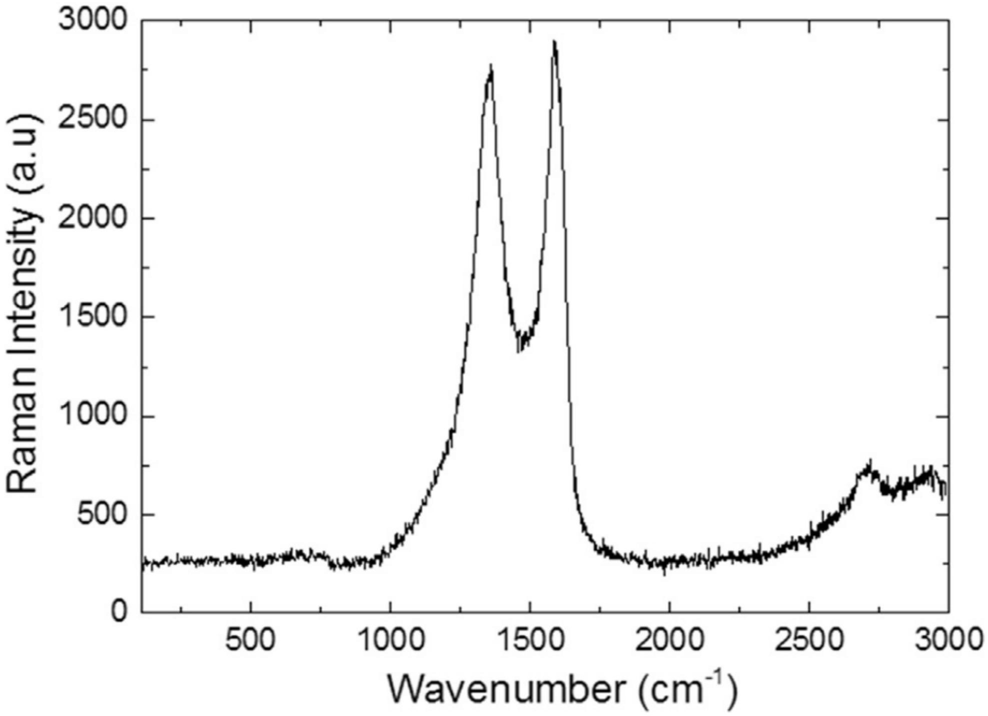

Figure 5.12: Raman spectrum of rGO-PcCo spin-coated onto a Si/SiO$_2$ wafer.

Figure 5.12 is an extended Raman spectrum of the rGO-PcCo material. Two major peaks were observed, referred to as D and G, at about 1350cm^{-1} and 1600cm^{-1}, respectively. From the analysis of the spectra, the intensity ratio of the D/G peaks (measured by dividing the corresponding integrated areas of the Raman peaks) was found to be about 1.7 for the doped material, whereas the corresponding value for the starting GO sample was 1.29.

Phthalocyanines have very distinct vibrational modes (Figure 5.13), but no signals attributable to PcCo molecules were observed in any of the Raman spectra obtained from that sample. This was an indirect indication that grafting of the doping species was rather sparse. This assumption was later confirmed by TEM imaging.

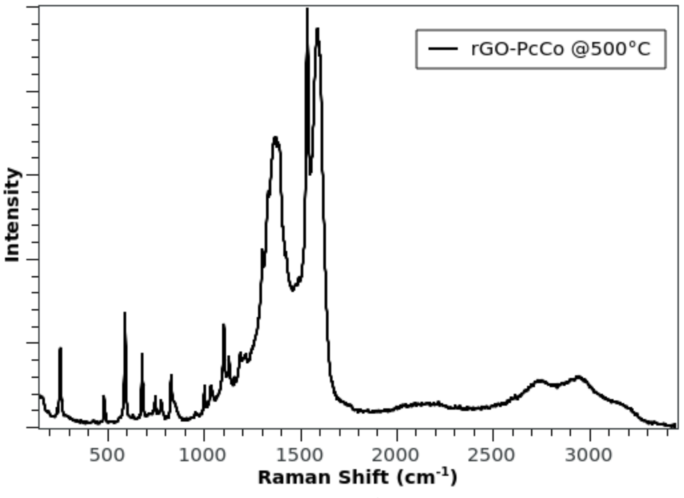

Figure 5.13: Raman spectrum of an rGO-PcCo hybrid, annealed at 500°C and which contained an excess of residual PcCo, not removed by washing. Signals belonging to PcCo molecules are clearly visible.

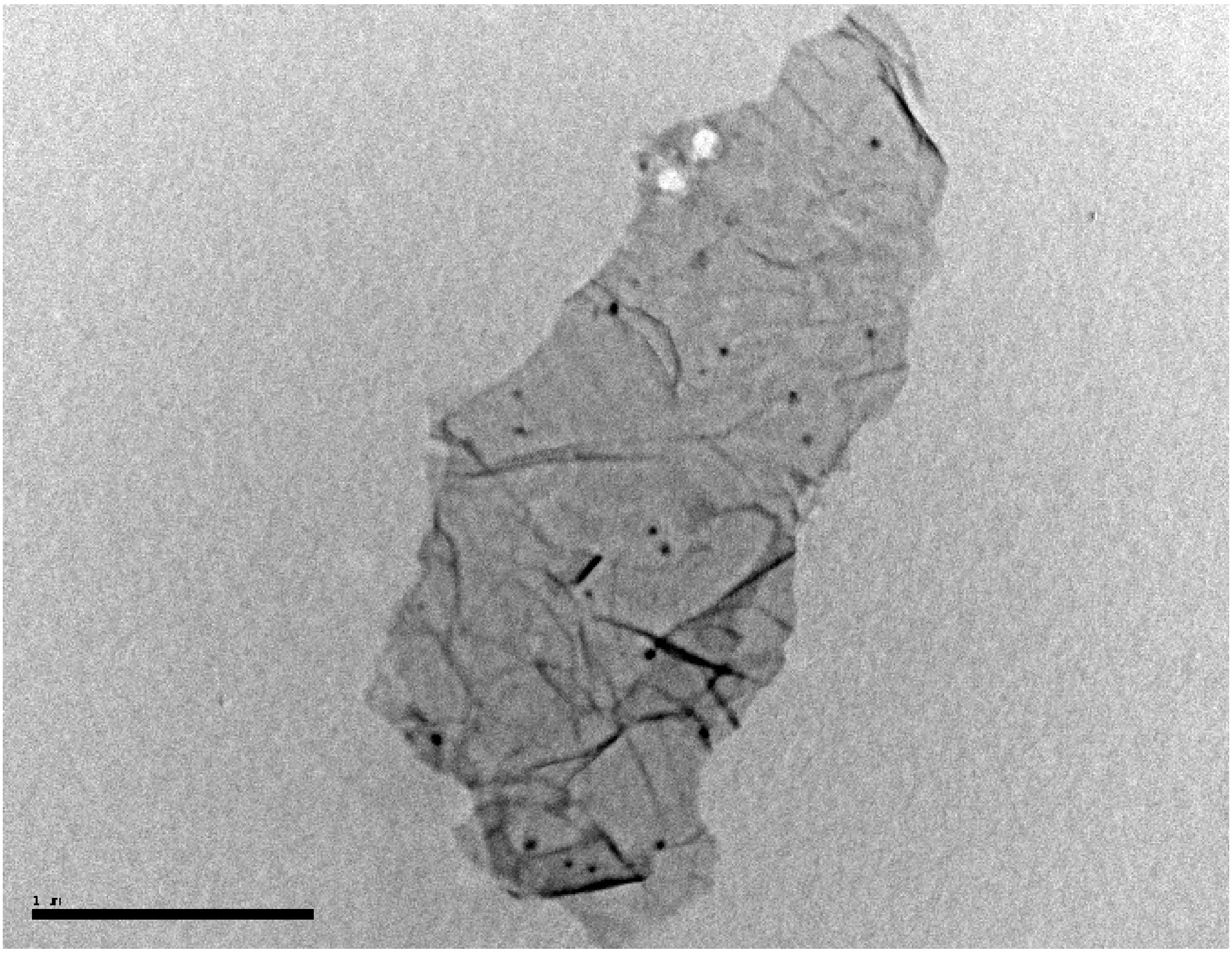

Image 5.1: Transmission electron micrograph of rGO-PcCo particles. The scale bar is 1μm.

The morphology of the doped rGO sheets was assessed by TEM imaging. Image 5.1 shows a representative TEM image of doped rGO sheets. The partial destruction of the graphitic structure and the appearance of wrinkled regions provides a visual confirmation of the observed Raman spectrum. The image also clearly shows the loading of the sheets with metal particles. The darker spots are areas of increased thickness/desnity compared with that of the reduced graphene oxide sheets. Small clusters of packed PcCo, decorating the sheets, are expected to result in such an image.

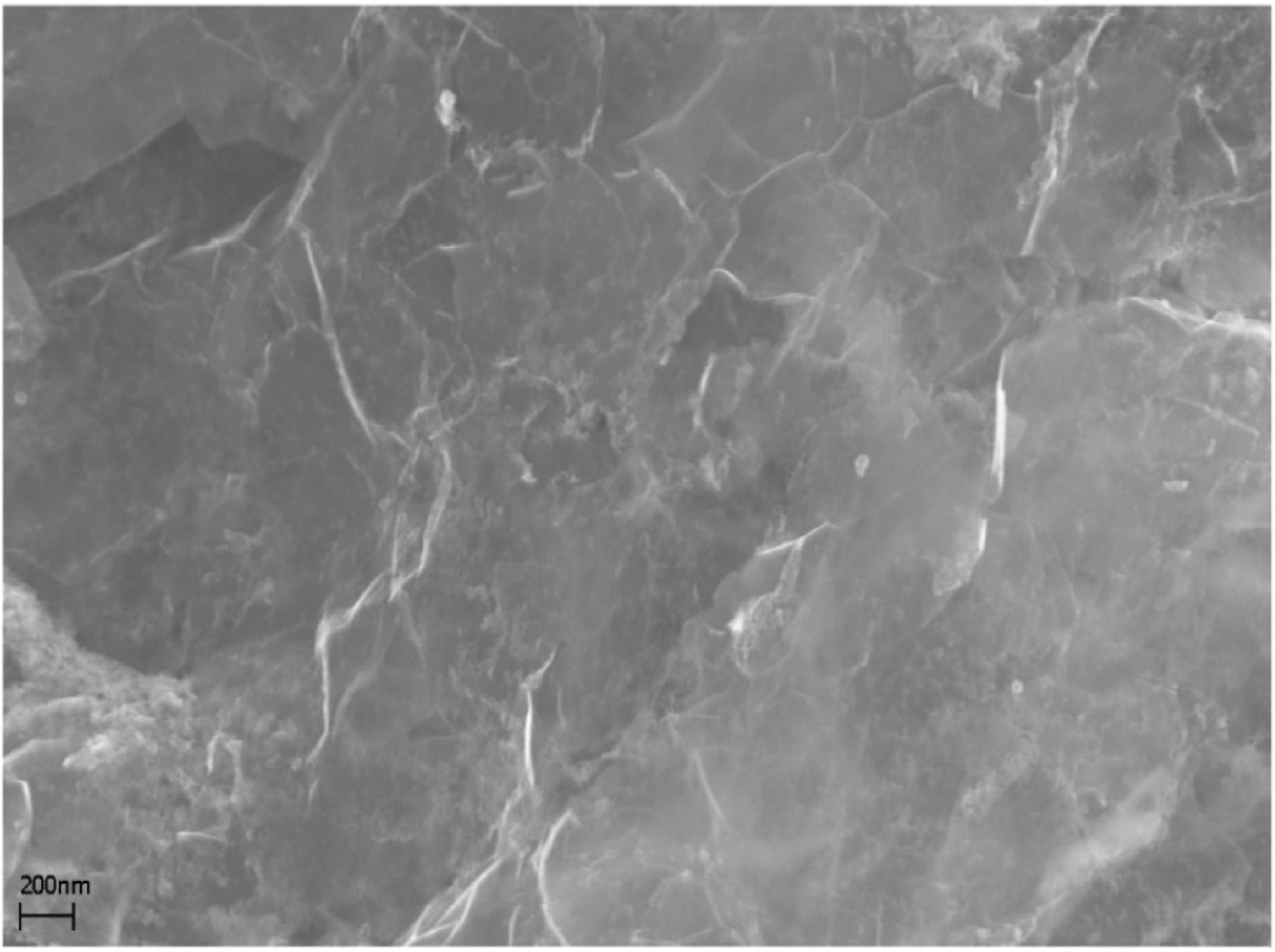

Image 5.2: FE-SEM image of an rGO-PcCo film deposited on an FTO glass substrate.

Image 5.2 is a FE-SEM micrograph of an rGO-PcCo film formed by spin coating on an FTO electrode. It is a characteristic image of a nanostructured film made of assembled rGO multilayers. The brighter areas are wrinkles in the graphene layers as well as edges of overlapping sheets.

Energy-Dispersive X-Ray spectra (EDX), collected by a detector connected to the FE-SEM confirmed the presence of cobalt in the samples. However, we could not deduce quantitative data about the composition of the material, as nitrogen can not usually be detected by EDX and also because signals from the oxygen atoms in the FTO support were picked up by the detector.

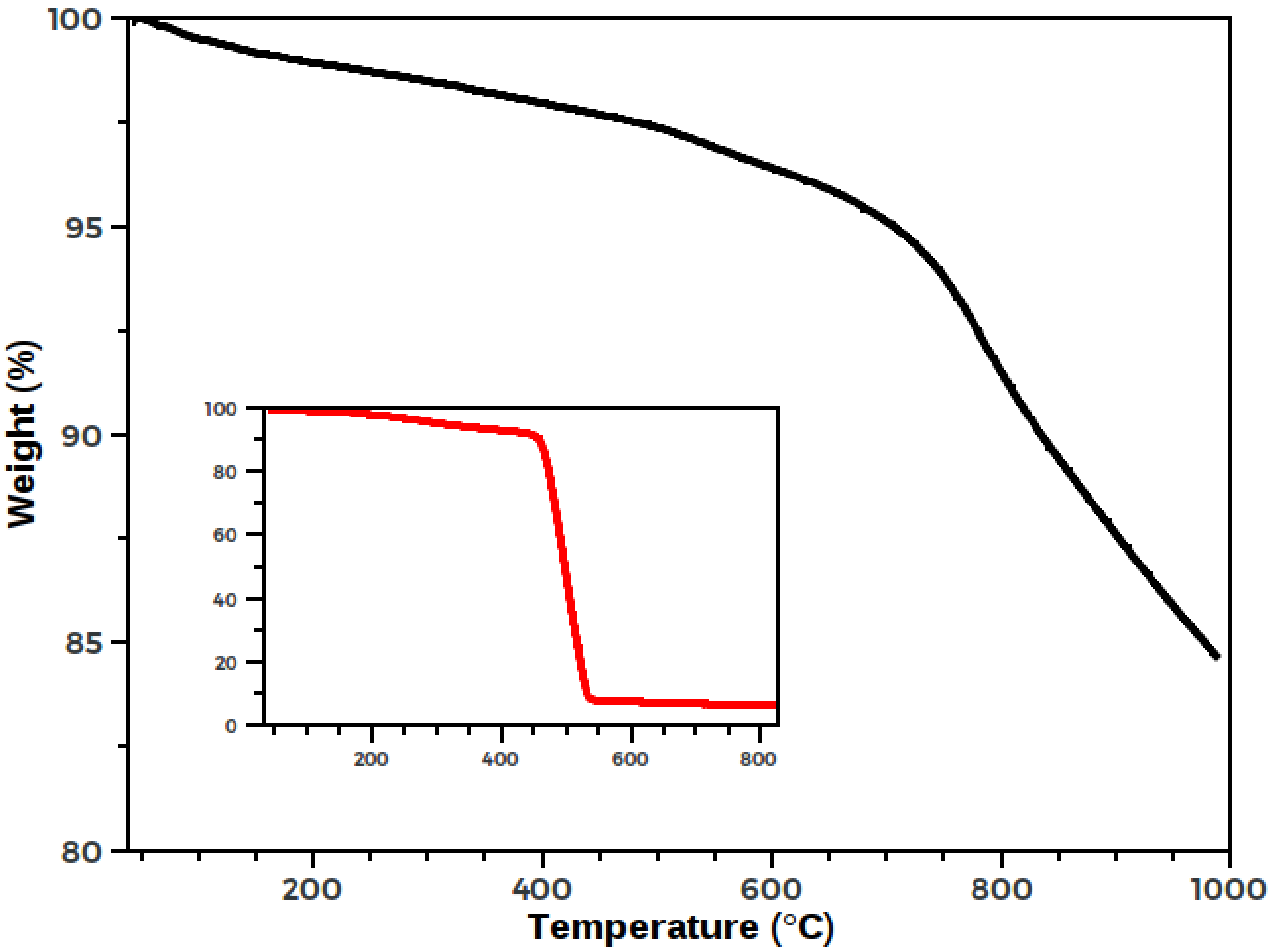

Figure 5.14: Thermogravimetric profile of the rGO-PcCo hybrid material in inert atmosphere. Inset: corresponding data for neat PcCo

TGA of the hybrid material showed a ~5 wt% weight loss up to 700 °C (Figure 5.14), indicating a well graphitized structure with a relatively low content of heteroatoms. The TGA profile of neat rGO material (not shown) did not experience any weight loss at temperatures below 230°C. When compared with the 1.2% weight loss of the doped material in the same temperature range, it is concluded that this loss should be both due to evaporation of trapped volatile species and phthalocyanine-based functionalities.

In this respect, TGA analysis of neat cobalt(II) phthalocyanine (Figure 5.14, inset) showed a 1.7% weight loss at 230°C, whereas a severe degradation took place in the temperature range between 450 and 535 °C. At 700°C, a total weight loss of about 92.7% was observed. Based on later observations, it was not actually “degradation”; most of the phthalocyanine had actually sublimed out of the crucible as vapors.

CoN_3 fragments or crystalline PcCo?

For quite some time, the question lingered. Was the electrocatalytic activity due to cobalt (II) phthalocyanine fragments, incorporated into the lattice, or due to PcCo crystallites, adsorbed on the surface of the graphene sheets? We devised another experiment, to try to settle the matter. We prepared a quantity of thermally reduced graphene oxide, by subjecting graphene oxide to the same treatment – heating it under Ar flow at 10°C/min, until the temperature had reached 700°C, at which it was annealed for 1h. We prepared a mixture consisting of 95% rGO and 5% PcCo (w/w%), dispersed it in isopropanol and deposited it as a thin film on an FTO glass substrate via spin-coating. This was used as a counter-electrode in a DSSC. For reference, we fabricated a second counter-electrode coated just with rGO.

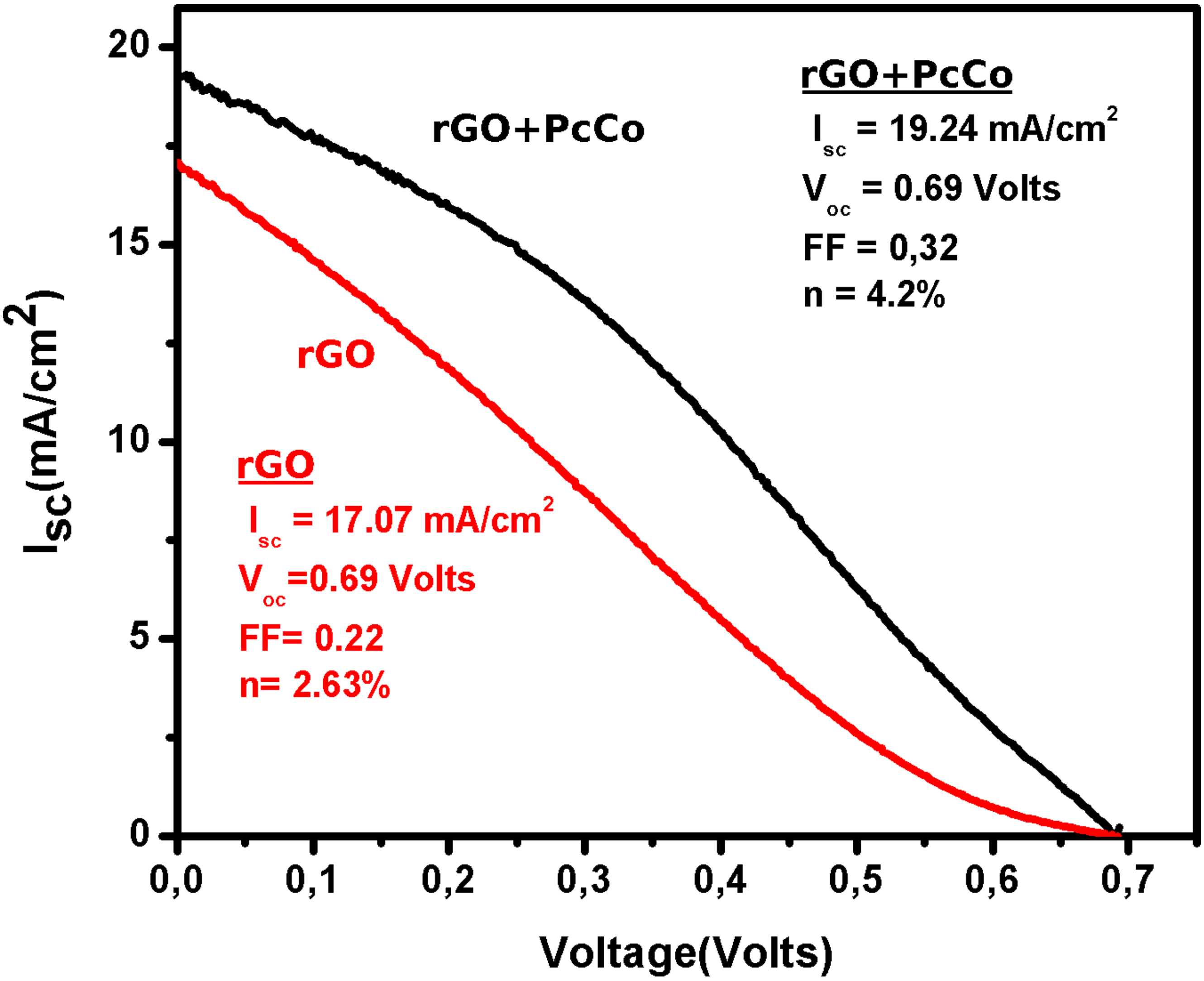

Figure 5.15: I-V curves of the rGO+PcCo mixture (black) and rGO (red).

From the data in Figure 5.15 we can see that the rGO counter-electrode achieves a mere 2.63% conversion efficiency. The rGO/PcCo mixture fares much better at 4.2%, but in turn, it lags behind the co-annealed rGO-PcCo hybrid, which was at 7.82%. By combining these results with those of PXRD, XPS and all the other characterizations, we concluded that the answer to the above question was "both". Crystalline cobalt(II) phthalocyanine adsorbed on the reduced graphene oxide sheets endows them with electrocatalytic function, but that alone is not enough; PcCo fragments in the graphitic lattice are needed to boost performance further.

Attempts at optimization and the effects of the graphene oxidation process

As it happened, we used up the last quantity of GO suspension prepared by the Kovtyukhova method[1] in the fabrication of the rGO-PcCo hybrid discussed above. At that time, we had another batch of GO suspension prepared according to the Zhao protocol[2] and we used that in our next experiments. However, we could not repeat the synthesis of the material at 700°C. As soon as the temperature got close to 300°C, PcCo vapors would start to be deposited on the colder areas of the quartz tube in the furnace (Image 5.3) and the resulting material would be completely devoid of PcCo and any electrocatalytic activity. This had not been observed during the initial synthesis.

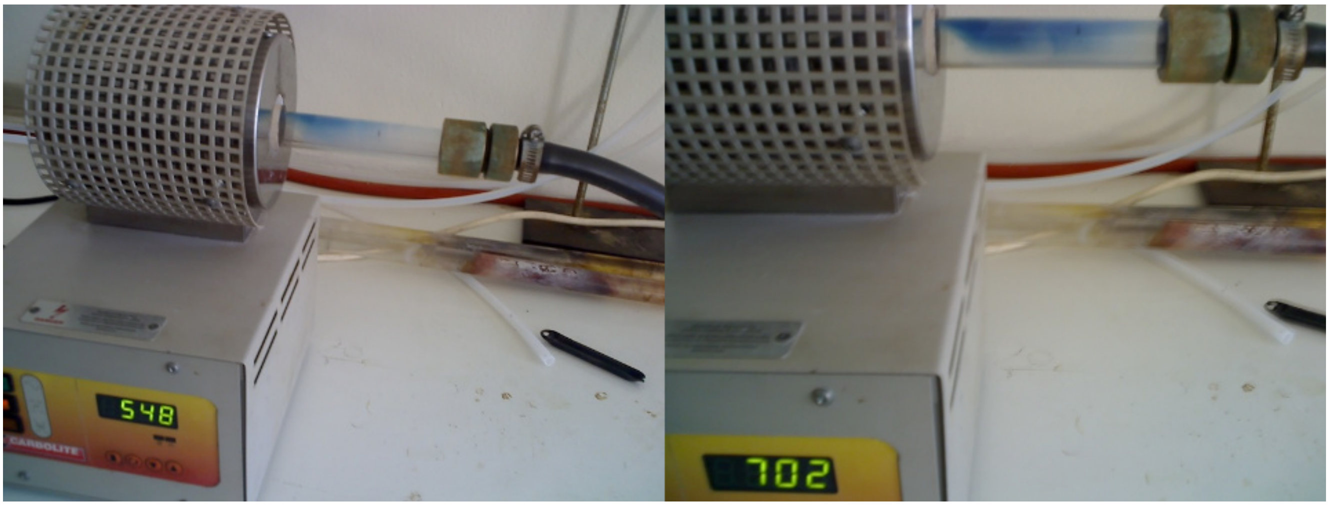

Image 5.3: PcCo deposited from vapors downstream of the combustion boat. As the temperature rose, more PcCo would be deposited on the tube's colder surfaces.

In the photographs above, the blue stain on the quartz tube is PcCo depositions. As the heating continued, the deposits grew. At that particular experiment, we found the needle-like PcCo crystals presented earlier, outside of the combustion boat. After weighing them, we realized that all of the PcCo had sublimed out of the material.

Because we wanted to examine the effects of the annealing temperature on the properties of the electrocatalyst, we had prepared several samples, which were heat-treated at 900°C, 800°C and 500°C. Even at the lowest temperature, almost all of the phthalocyanine would sublime out of the mixture. The annealed materials would exhibit little or no electrocatalytic activity.

At the same time, we had also prepared some samples containing iron(II) and magnesium phthalocyanines, which were annealed at 900°C, 800°C and 700°C. Magnesium phthalocyanine would start to sublime at even lower temperatures, somewhere below 200°C. The graphitic lattice could not be sufficiently restored at these temperatures, so PcMg was abandoned. Sublimation was observed during the annealing of the samples containing PcFe, though a measurable amount would remain in the annealed material. However, that residue consisted mainly of mixtures of Fe(II) and Fe(III) oxides, as evidenced by XRD measurements and the material could not adequately function as an electrocatalyst, so PcFe was eventually abandoned as well.

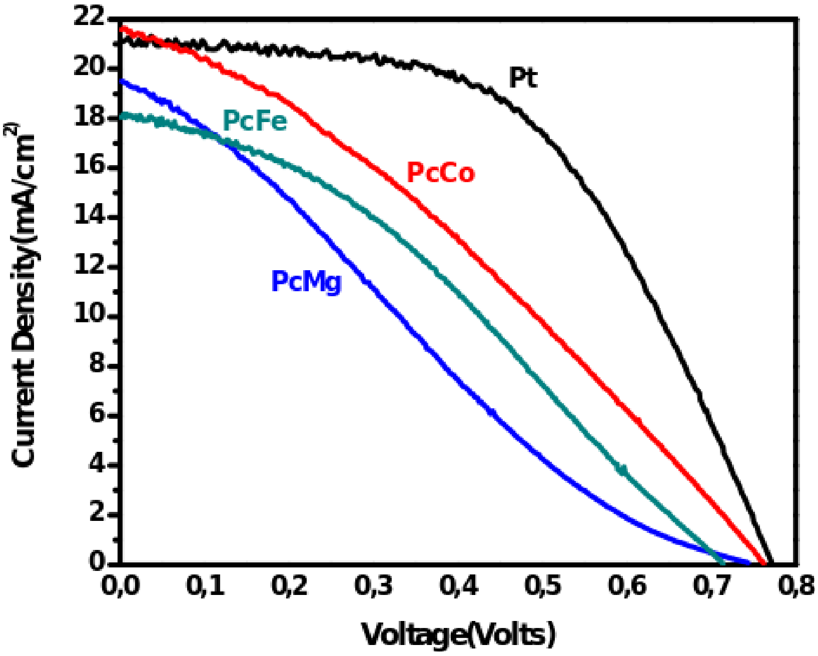

Figure 5.16: I-V curves of DSSCs with counter-electrodes made of GO annealed with PcMg, PcFe and PcCo.

The I-V curves in Figure 5.16 summarize the disappointing electrocatalytic performance of the best samples prepared with each phthalocyanine at the time. We saw no point in pursuing the fabrication of devices based on PcMg or PcFe, so we focused our attention on the PcCo materials.

Having looked at and eliminated every possible variable in the process, from the mixing of the materials to the furnace that was used in annealing, the only possible culprit for the discrepancies was the GO batch that we had used as our starting material. So we set out to produce another batch of GO suspension adhering to the Kovtyukhova protocol and repeat the experiments.

Even though the newer results did not exactly coincide with those of the first experiment, there was a marked difference with all the failed ones. Sublimation was still observed, but to a much lesser extent. By trial and error, we found that the best way to produce a structurally identical material was if during the evaporation of the solvents and drying of the residue, we used slightly elevated temperatures. Heating at 85°C-90°C and subsequent drying at ~120°C produced a material with an identical X-ray diffraction pattern to that of the original.

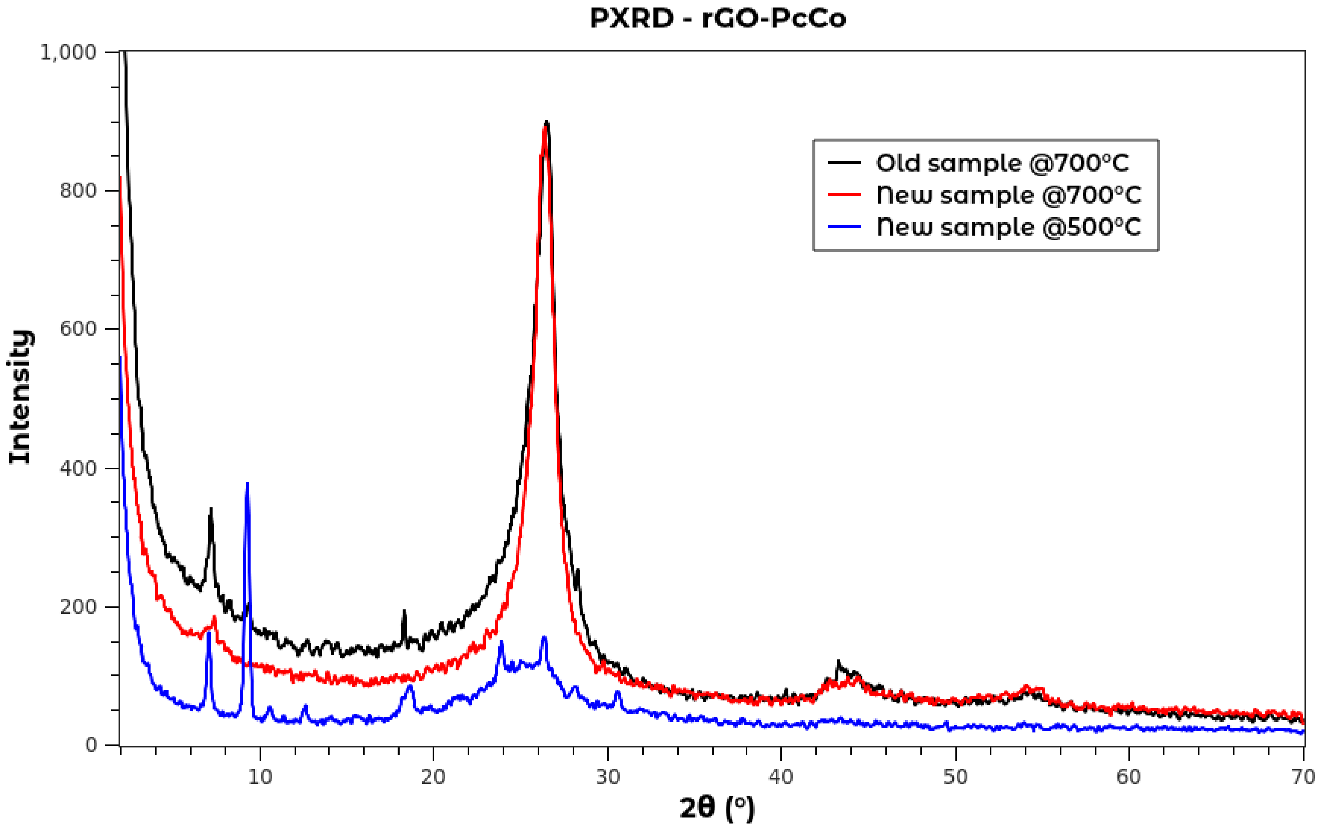

Figure 5.17: Powder X-ray diffraction patterns of the old, successful material (black) and two samples with GO prepared according to the Kovtyukhova protocol, one annealed at 700°C (red) and the other at 500°C (blue).

The diffraction patterns in Figure 5.17 are of a sample prepared with the more intense evaporation and drying regime (red), which exhibits similar characteristics to those of the old material (black). A third sample, annealed at 500°C is shown in blue. The latter displays a lower restoration of the lattice, which was to be expected. The β polymorph of PcCo is evidently present in large quantities, even after meticulous washing with ~1.5L of THF.

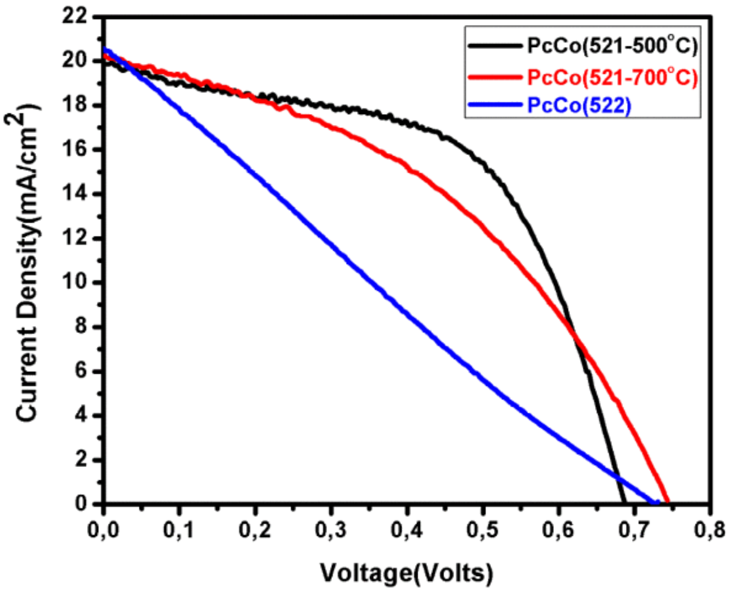

Figure 5.18: I-V curves of rGO-PcCo hybrid counter-electrodes, made from the latest Kovtyukhova GO batch.

The I-V curves of these two materials, labeled 522 and 521-500°C respectively are shown in Figure 5.18. During the preparation of the sample labeled 521-700°C (which was annealed at 700°C) and the 521-500°C, evaporation and drying temperatures were ~55°C and 85°C respectively. Unfortunately, our partners had trouble applying a film of the 522 sample, which was structurally similar to the old one, hence the poor results. The measured conversion efficiencies for the samples 521-500°C, 521-700°C and 522 were 7.73%, 6.31% and 3.57% respectively.

Nitrogen-doped rGO/PEDOT composite

The morphology of graphene derivatives, prepared in a top-down approach, robs them of some of the qualities that make graphene attractive as a material. Forming them into films is a challenge, as they are usually hydrophobic and out of suspensions, the particles tend to aggregate. Films obtained by techniques such as spin coating or drop casting might at times appear macroscopically uniform, but at the nanoscale, misalignment and gaps between graphene sheets result in a very low conductivity. This poses problems in the application of graphene-based materials in electrocatalysis. While there are numerous ways to dope and modify graphene in order to tune its properties, the resulting materials prove inadequate, exactly because of their low conductivity.

In a previous chapter we have seen that an increasingly employed method to circumvent the issues arising from the non-uniformity of graphene-based films is to use a conducting polymer to bridge the gaps between graphene sheets. Enveloping or embedding graphene in conjugated polymers opens up more routes for the electrons to take between catalytically active sites and across the bulk of the material. With that in mind, we attempted to combine N-doped graphene, a material with documented electrocatalytic properties, with PEDOT, a conducting polymer which is transparent and thus suitable for use in photogalvanic components.

To recap, the process consisted of spin coating mixtures of a GO suspension and a urea solution onto FTO glass substrates, which were then annealed, to produce N-doped reduced graphene oxide. The N-doped rGO film was then covered by a layer of PEDOT, formed by electropolymerization. A number of composites were produced, using PEDOT and untreated mixtures of GO and urea, as well as mixtures of GO and urea with varying composition and annealed at different temperatures. We have already reported that we obtained the best results from a mixture of GO:urea with a mass ratio of 55:45, annealed at 350°C for 15min. All the of the following results concern that sample.

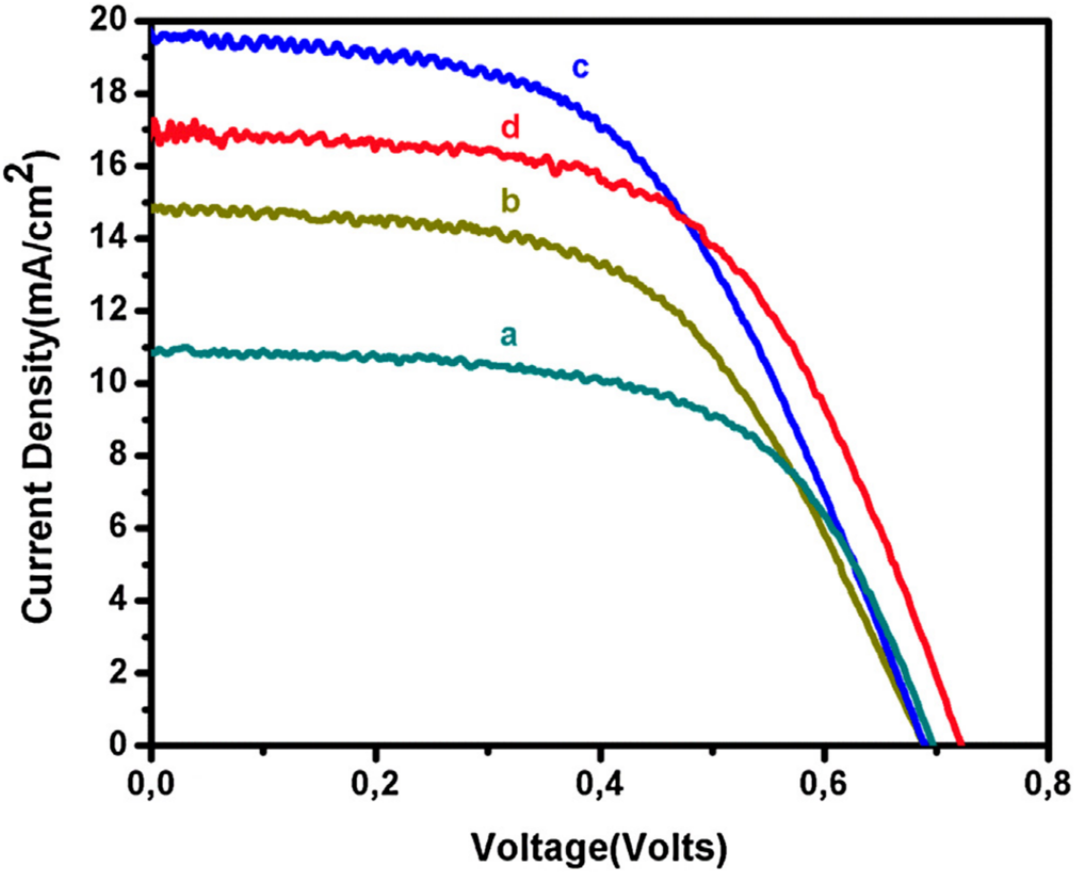

Figure 5.19: Current density-voltage curves obtained with DSSCs bearing various counter-electrodes: (a) PEDOT, (b) PEDOT/GO-urea, (c) PEDOT/rGO-urea and (d) Pt (reference).

The efficiencies of the devices based on PEDOT, PEDOT/GO-urea, PEDOT/rGO-urea, and Pt electrocatalysts were 4.6, 5.6, 7.1, and 7.0%, respectively. The combination of PEDOT with rGO-urea raised the efficiency of the cell to 7.1%, which is comparable within experimental error to that of the Pt reference. N-doping seems to further enhance the electrocatalytic activity of reduced graphene oxide-based electrode materials in DSSC devices, compared to previously reported data where non-doped graphene was used[3].

Table 5.4: Photovoltaic performance data extracted from Figure 5.19.

Counter electrode	I_{SC} (mA/cm^2)	V_{OC} (Volt)	Fill Factor	η%
PEDOT	10.8	0.70	0.61	4.6
PEDOT/GO-urea	14.7	0.68	0.56	5.6
PEDOT/rGO-urea	19.5	0.68	0.53	7.1
Pt	17.3	0.72	0.57	7.0

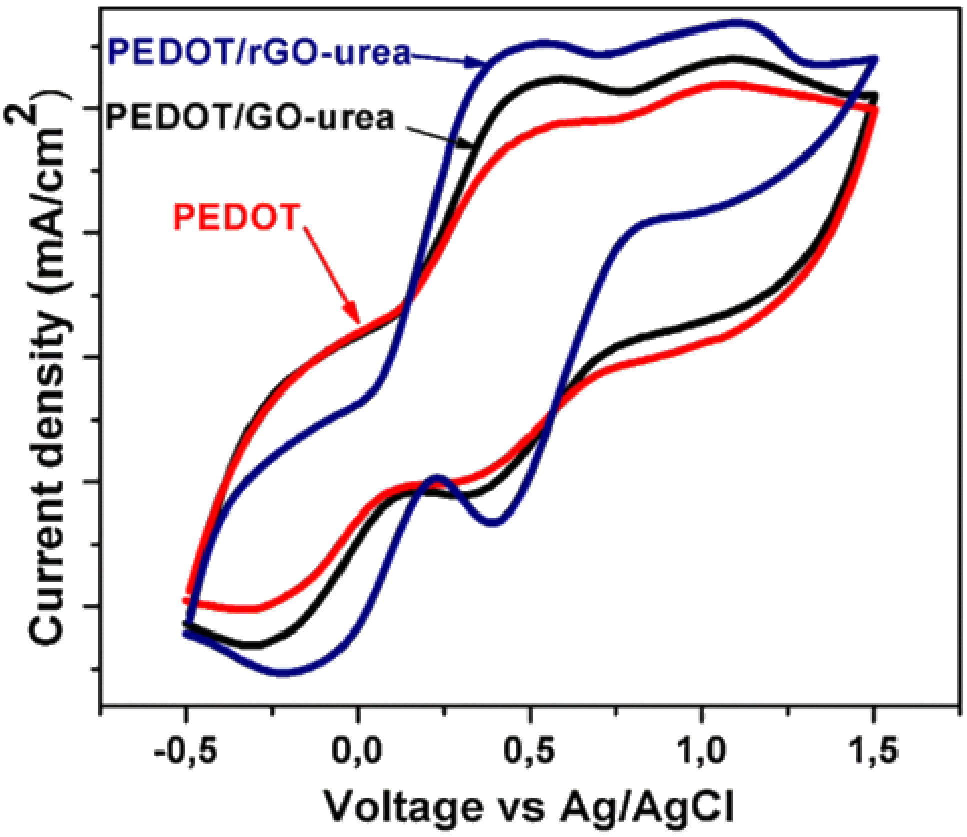

Figure 5.20: Cyclic voltammograms recorded with various PEDOT-containing electrocatalysts supported on FTO electrodes, using Ag/AgCl and a platinum sheet as reference and counter electrodes, respectively.

Again, there are no extraneous peaks in the voltammogram in Figure 5.20, which means that there are no secondary redox reactions taking place in the system. Peak separation does not differ significantly between the three materials, though it is a bit lower than that of the Pt reference (not plotted for clarity). The N-doped/PEDOT composite exhibits both a higher anodic and a higher cathodic current, indicating a faster/increased charge exchange at the electrode-electrolyte interface.

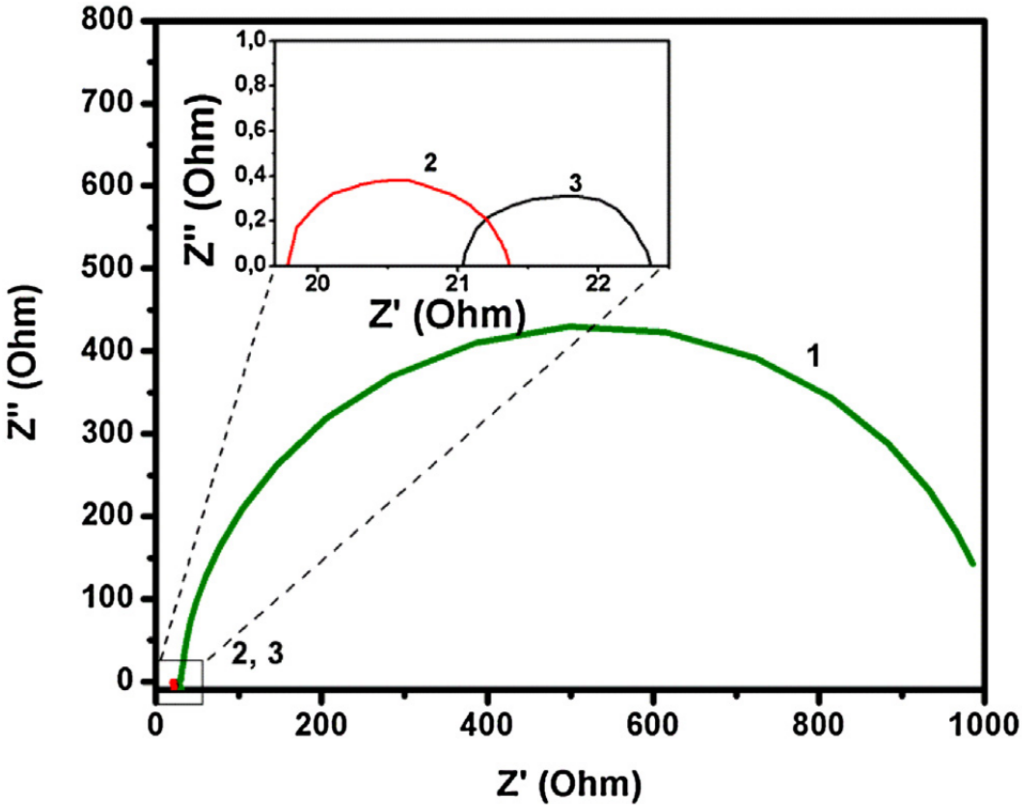

Figure 5.21: Nyquist plots obtained by EIS measurements using symmetric electrodes with various electrocatalysts: (1) rGO-urea; (2) PEDOT/rGO-urea; and (3) Pt reference.

Electrochemical impedance spectroscopy (EIS) was used to characterize the electrocatalysts, by using symmetric cells and the same electrolyte as the one employed in the DSSC devices. The purpose of this procedure was to estimate the charge transfer resistance R_{CT} between the electrode and the electrolyte. The results are presented in Figure 5.21. It is interesting to note that the N-doped graphene by itself demonstrated a huge R_{CT} (>1kΩ) compared to that of Pt (only 1.4Ω). When PEDOT was added to the modified graphene film, R_{CT} dropped dramatically to about 1.5Ω, i.e. it became equivalent to the Pt reference standard. These results are in accordance with the data from cyclic voltammetry, indicating the importance of the presence of PEDOT in boosting the efficiency of the electrocatalyst.

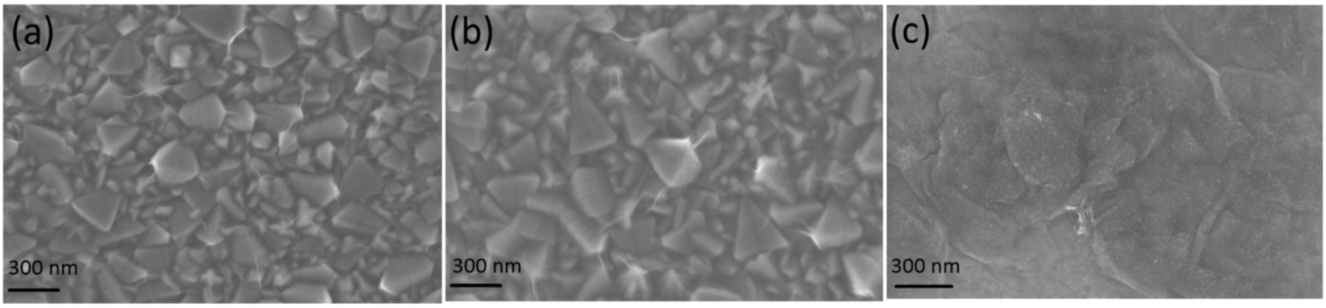

Image 5.4: SEM images of deposited GO flakes (a), thermally annealed GO-urea at 350°C (b) and GO-urea/PEDOT film on FTO glass (c). The flakes are hard to discern, as FTO nanoparticles from the substrate are the dominant aspect in these images.

GO flakes exhibit a wrinkled structure, while the boundaries of the deposited nanostructures are distinguished with difficulty, due to the small thickness of the sheets (Image 5.4a). Indeed, the appearance of the micrographs of Image 5.4a and b is overwhelmed by the underlying FTO nanostructure. Untreated and thermally annealed GO-urea have no noticeable differences in their morphology. In addition to the presence of thin layered nanostructures, a few randomly distributed aggregates with sizes in the range 100–200nm were observed and are attributed to organic residues derived from urea annealing (Image 5.4b).

After the electrodeposition of a PEDOT film on either untreated or annealed GO-urea mixture, a porous morphology was generated, consisting of globular polymeric aggregates (Image 5.4c). The roughness and the coverage homogeneity of the deposited PEDOT film onto either the untreated GO-urea or the annealed mixture (denoted as rGO-urea) was assessed by AFM imaging (Image 5.5a,b).

When PEDOT was electrodeposited onto an untreated GO-urea film, islands of polymeric material were mostly observed, whereas the roughness was in the range between 100 and 150nm. On the contrary, in the case of the annealed sample, the electrodeposited polymer seemed to cover homogeneously the rGO-urea film. The presence of PEDOT-based islands was not so pronounced and the roughness itself was decreased to values below 50nm. This is an indirect indication that the hydrophobic polymer has a noticeably higher chemical affinity for the annealed GO-urea film, than for the thermally untreated mixture. The variation in coverage homogeneity of the PEDOT film was also assessed by SEM imaging (Image 5.5c,d) and optical microscopy (data not shown). It was clearly observed that, under similar conditions, the polymer film on untreated GO-urea is deposited in a non-homogeneous manner.

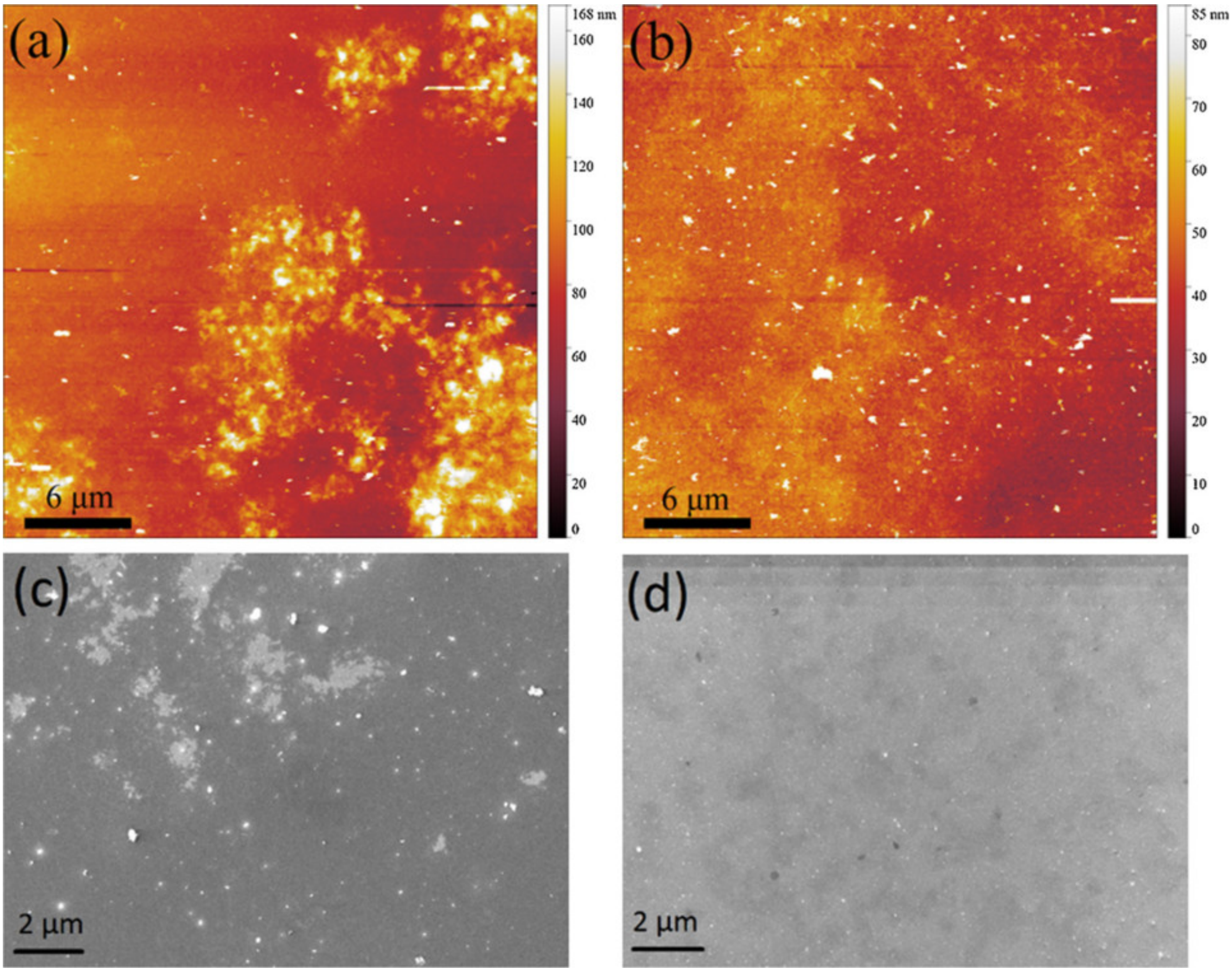

Image 5.5: Representative AFM & SEM images of GO-urea/PEDOT films (a,c) and rGO-urea/PEDOT films (b,d).

Raman

Raman analyses of neat GO, GO-urea and rGO-urea films are shown in Figure 5.22:

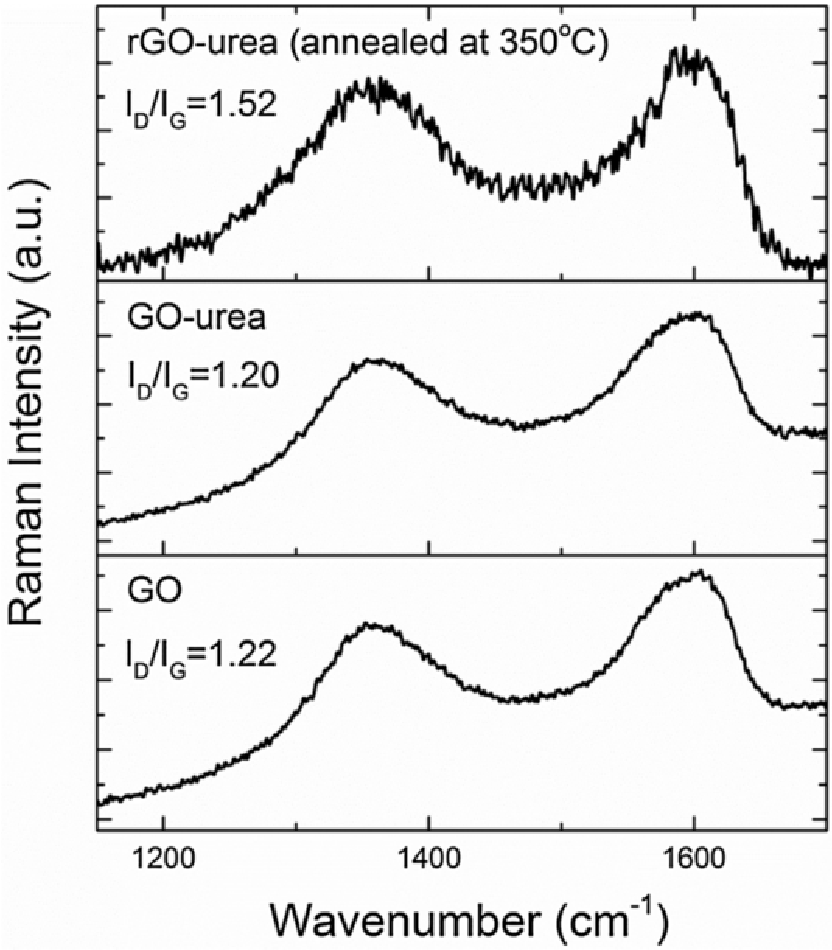

Figure 5.22: Raman spectra (λ_{exc} = 514nm) of GO, untreated GO-urea and thermally annealed at 350°C rGO-urea films.

As expected, all samples show the characteristic D band at about 1350cm^{-1} and the G band at 1580cm^{-1}. The former peak is attributed to the sp^3-hybridized carbon atoms at defect sites of the graphitic lattice, whereas the latter to vibrational modes of sp^2 carbons in the basal plane. The integral intensity ratio between the D and the G band is an indirect measure of the graphitization level of such materials. After the thermal annealing of the GO-urea mixture at 350°C, the D/G ratio increased from 1.2 to 1.5. This could be explained by a slight size decrease of sp^2 domains, caused by the elimination of evolved gases and partial scission of graphitic flakes.

XPS

We used XPS to investigate the physicochemical interactions of N-doped graphene with PEDOT at the interface of the optimized layer-by-layer structure.

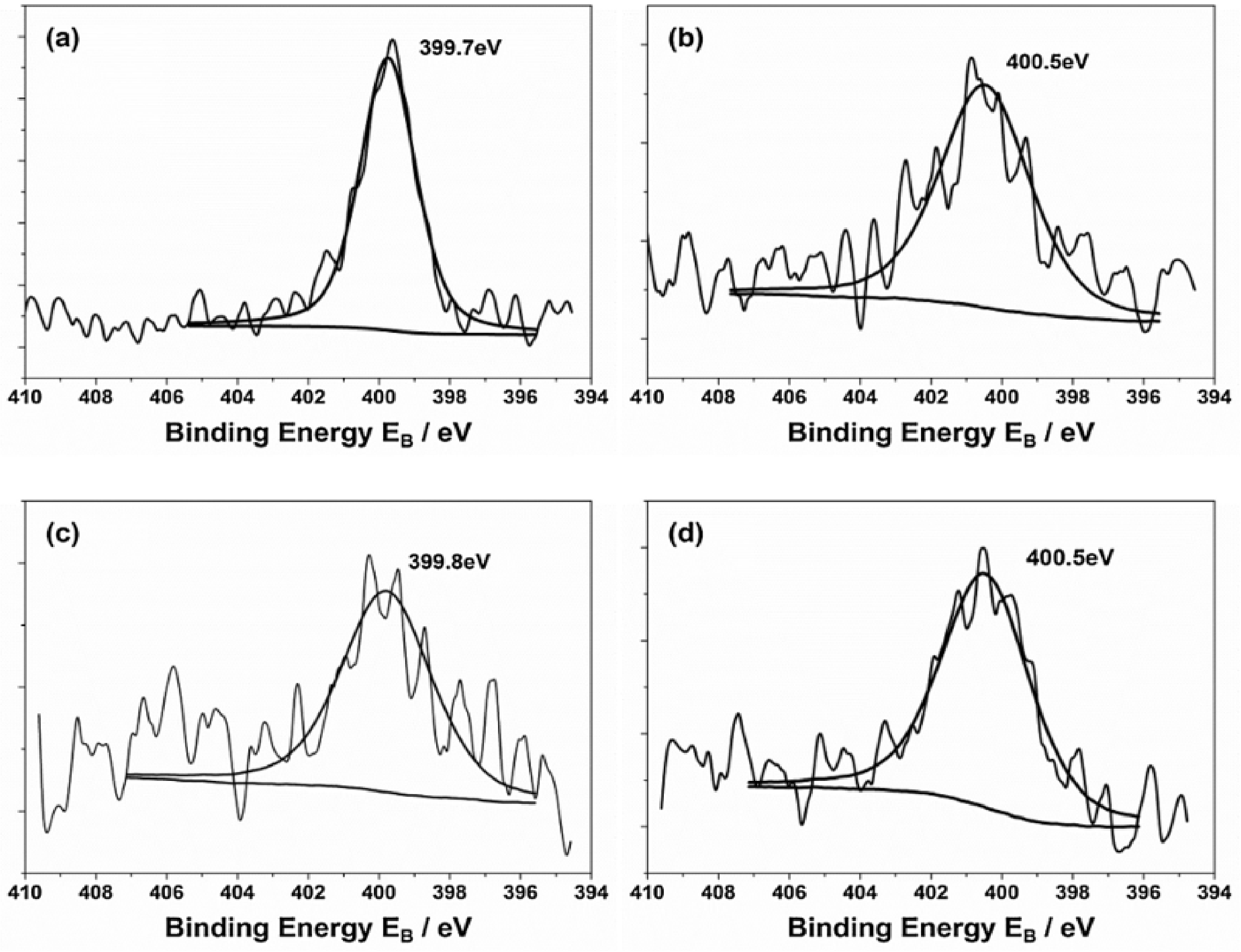

Figure 5.23: N1s peak of (a) GO-urea/ITO, (b) rGO-urea/ITO, (c) PEDOT/GO-urea/ITO and (d) PEDOT/rGO-urea/ITO.

In the wide scan spectra (not shown), elemental photoelectron peaks corresponding to C, N, O, S and In were observed, with the latter species derived from the ITO substrate. Figure 5.23 shows the N1s peak of the GO-urea/ITO, rGO-urea/ITO, PEDOT/GO-urea/ITO and PEDOT/rGO-urea/ITO thin films. For the GO-urea and PEDOT/GO-urea samples, the N1s peak consists of one component centered at 399.8 ± 0.1eV. It is assigned to the N in pure urea ($O=C-NH_2$ bonding). On the contrary, for rGO-urea and PEDOT/rGO-urea thin films, the component centered at 400.5±0.1eV could be indexed to either amide, amine or pyrrolic nitrogen species.

It was calculated that the nitrogen content in the as-deposited GO-urea film is ∼21wt%. After annealing at 350°C, the nitrogen content is estimated to be ∼10wt%. This value was extracted from the data in Table 5.5, since the N1s/C1s intensity ratio decreases by ~50% after the annealing process.

Table 5.5: Ratio of the XPS N1s/C1s peak intensities

Sample	N1s/C1s
GO-urea/ITO	0.072
rGO/urea/ITO	0.036
PEDOT/GO-urea/ITO	0.015
PEDOT/rGO-urea/ITO	0.019

From the N1s spectra, it was observed that no apparent chemical interaction occurs between N-doped graphene and PEDOT, which could be attributed to potential grafting of the nitrogen atoms of doped graphene and the sulfur atoms of the polymer. The S2p spectra of the composite films (not shown) were deconvoluted to two different components. The main one was assigned to sulfur which is bound as heteroatom in aromatic rings, whereas a low intensity component was attributed to the PEDOT sulfur atom in the partially oxidized state. No apparent changes were observed in the spectra of either sample when comparing them with that of a neat PEDOT film. This result is in agreement with the N1s spectra, implying no chemical interaction between heteroatoms at the interfacial region of either GO-urea or N-doped rGO film with a PEDOT layer. Yet, covalent attachment of PEDOT chains onto the graphitic lattice through C-C bonding during the electropolymerization step cannot be ruled out.

The C1s XPS peaks of either GO-urea or thermally treated GO-urea film on ITO are similar as the ones of GO and reduced GO films, respectively. An additional contribution is that of the C-N bond configuration, due to the presence of either parent urea or its thermal decomposition adducts. The binding energies assigned to carbon-nitrogen bonds lie between 285.2 and 286.1eV, depending on the type of bonding. Due to the extended overlap with the corresponding peak of the C-C sp^3 bonds (at 285.6eV), it is not possible to separately analyze the C-N and sp^3 C-C components. Therefore, the C-N component intensity is included in the sp^3 C-C component.

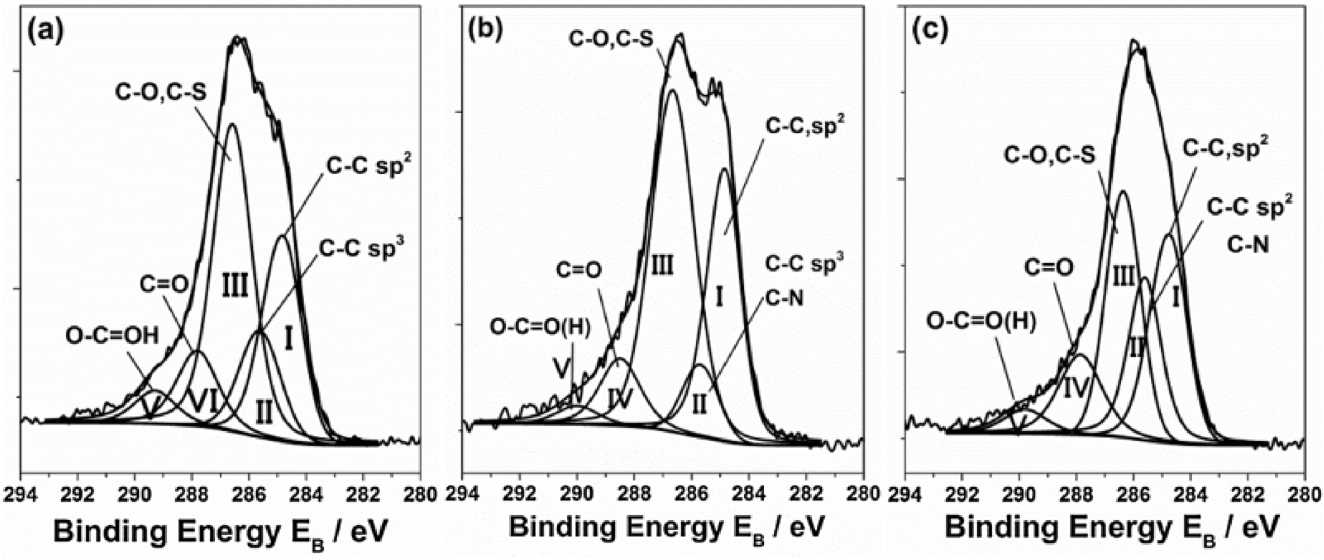

Figure 5.24: Deconvoluted C1s peaks of (a) PEDOT/ITO, (b) PEDOT/GO-urea/ITO and (c) PEDOT/rGO-urea/ITO.

In order to analyze the C1s peak of the samples covered with a thin film of PEDOT (thickness ∼8nm), a reference neat polymer sample was deposited onto ITO and its deconvoluted spectrum is shown in Figure 5.24a. The peak is analyzed into five components: C-C sp^2 (peak I), C-C sp^3 (peak II), C-S/C-O bonds (peak III), carbonyls (peak IV) and carboxyls (peak V). The deconvoluted C1s peaks of the corresponding samples PEDOT/GO-urea and PEDOT/rGO-urea are illustrated in Figure 5.24b and c, respectively.

As observed from the relative intensities of the aforementioned C1s components, the peak II (C-C sp^3 and C-N bonds) in comparison with the corresponding peak of I (C-C sp^2) is more pronounced in the PEDOT/rGO-urea/ITO sample than either PEDOT/ITO or PEDOT/GO-urea/ITO. This could be partly ascribed to potential C-C covalent bonding between N-doped graphene and PEDOT, during the electropolymerization step. Moreover, the N1s/C1s total intensity ratio was reduced more drastically in the GO-urea/ITO than rGO-urea/ITO sample, after the deposition of PEDOT (Table 5.5).

Taking into account the SEM/AFM findings (Image 5.5), where the PEDOT film was uniformly distributed onto rGO-urea without exposing any bare rGO-urea domains, we expected that the N1s of the PEDOT/rGO-urea film would be hardly detectable in the XP spectrum. Yet, as shown in Table 5.5, the corresponding N1s/C1s ratio is slightly larger than the one of PEDOT/GO-urea. This could be explained by a potential diffusion of N-doped graphene platelets within the PEDOT layer during the electrodeposition step.

In order to verify this unexpected result, the PEDOT/rGO-urea sample was also measured at a 45° exit angle, by which the XPS technique is more superficial. The intensity ratios N1s/C1s and N1s/S2p were the same for both exit angles, indicating that nitrogen species are – to some extent – integrated into the PEDOT layer. This could be – partly – the reason for the enhanced intensity of component II in the PEDOT/rGO-urea C1s peak. The above results indicate that nitrogen-containing graphitic fragments are incorporated into the PEDOT film, during the electrodeposition step.

Chapter Bibliography

[1] Kovtyukhova, N. I.; Ollivier, P. J.; Martin, B. R.; Mallouk, T. E.; Chizhik, S. A.; Buzaneva, E. V.; Gorchinskiy, A. D. Layer-by-Layer Assembly of Ultrathin Composite Films from Micron-Sized Graphite Oxide Sheets and Polycations. *Chem. Mater.* **1999**, *11* (3), 771–778 DOI: 10.1021/cm981085u.

[2] Zhao, J.; Pei, S.; Ren, W.; Gao, L.; Cheng, H.-M. Efficient Preparation of Large-Area Graphene Oxide Sheets for Transparent Conductive Films. *ACS Nano* **2010**, *4* (9), 5245–5252 DOI: 10.1021/nn1015506.

[3] Nikolakopoulou, A.; Tasis, D.; Sygellou, L.; Dracopoulos, V.; Galiotis, C.; Lianos, P. Study of the Thermal Reduction of Graphene Oxide and of Its Application as Electrocatalyst in Quasi-Solid State Dye-Sensitized Solar Cells in Combination with PEDOT. *Electrochimica Acta* **2013**, *111*, 698–706 DOI: 10.1016/j.electacta.2013.08.064.

[4] Petraki, F. Study of the Interfaces Formed between Thin Films of Phthalocyanines and Inorganic as Well as Organic Substrates by Photoelectron Spectroscopies, Department of Chemical Engineering, University of Patras: Patras, 2008.

6. Conclusions

Through this work, we have succeeded in producing two cost-effective, electrocatalytic materials, capable of supplanting platinum in DSSC counter-electrodes. Their fabrication process is particularly simple, it does not require highly specialized tooling and it is easy to scale up. We strongly suspect that a more refined, streamlined fabrication method could produce better results with the same materials, than what we have managed. As with most electrochemical components, these materials are not constrained in this specific application and could see use in other areas, e.g. in photocatalytic fuel cells.

In the case of the N-doped graphene/PEDOT composite, we have reaffirmed that conductive polymers can be used to enhance the electronic properties of graphene nanoparticles, much like laying wiring, but at the nanoscale. Since PEDOT is transparent both at rest and when it is conducting, perhaps it could also be used as a protective coat over more sensitive moieties in photochemical applications. The analysis of the interactions between N-doped graphene and PEDOT yielded some unexpected results, which are worthy of further investigation.

The work surrounding the rGO-PcCo hybrid might have felt like starring in a detective novel at times, but it certainly was worthwhile. The resulting material manages to compete with platinum because of its combination of electrocatalytically active sites with a higher surface area, multiplying the interactions with the redox pair. There are a number of avenues left unexplored at the completion of this thesis. Could the loading of the graphene sheets with phthalocyanine be optimized? How does crystalline phthalocyanine enhance the efficiency of the device? Does the counter-electrode in effect function as a photocathode? These are all questions begging to be answered.

Another point made clear at the conclusion of this project, is that graphene oxide is a tricky or treacherous – depending on who you ask – material to work with. All the variables involved in its preparation require very careful monitoring and precise handling. While one might expect from different oxidation methods to yield oxides with different behaviors, slight variations within the same method could have the same result.

A final observation, concerns the complementarity of analytical techniques. One should never rely on the results of any one characterization to draw conclusions. Even closely related techniques can reveal very different phenomena. Outliers and data at the edge of background noise or just outside statistical error should be actively sought out and verified or discarded, by examining them from a different perspective. Over-reliance on a particular instrument or method is certain to lead to misconceptions.